Bielefeld University
Faculty of Physics

Screening Meson Masses towards the Chiral Limit

- PhD Thesis -

Simon Fabian Dentinger

Supervisor and 1st Referee:
Dr. Olaf Kaczmarek

2nd Referee:
Prof. Dr. Frithjof Karsch

Bielefeld, November 5, 2021

Contents

Chapter 1

Motivation

From the beginning of human self-consciousness we have asked ourselves where we come from. It is now accepted that on a large scale the universe was created at the Big Bang. Nowadays mainly the long distance force from gravity dominates the universe, while just a fraction of a second after the Big Bang the strong force dominated. This situation can be simulated in heavy-ion collisions. Through those experiments we hope to achieve a better understanding of the properties of matter.

When one is talking about the properties of matter one also has to talk about phases. Depending on external conditions matter is in a specific phase. By slowly changing these conditions in a way that this matter converts itself to a different phase, one goes either through a so-called phase transition or a crossover. An everyday example is water. Under normal temperature and pressure it is liquid, but if we heat it up enough, water will transition into a gas.

In a similar fashion strong-interaction matter changes its phase. Through calculations with the quantum field theory of the strong interaction, Quantum Chromodynamics (QCD), it is known that the quarks are confined in hadrons in the hadronic phase and are asymptotically free in the so-called Quark-Gluon-Plasma (QGP) phase [1]. Through calculations using the lattice regularization it is known that at zero and small baryon chemical potential for physical quarks this kind of matter is an analytic crossover to the QGP phase [2,3]. The QGP phase was also studied experimentally in heavy-ion collisions. From 2005 researchers at the Relativistic Heavy Ion Collider (RHIC) published growing evidence that the QGP phase exists [4–7]. There is however still a lot to learn about the QCD phase diagram. What we e.g. also know from lattice QCD calculations is the transition temperature. For small values of baryon chemical potential we also know that the transition temperature becomes smaller with increasing baryon density hinting to a transition arc towards zero temperature [8]. Through calculations with

the functional renormalization group we know that the phase transition for small temperatures and high baryon chemical potential is first order [9]. In the current research we expect that the crossover line at low baryon chemical potential transforms to that first order phase transition. The point where crossover and first order transition would meet would be the Critical End Point (CEP). That CEP would be a second order phase transition. A sketch of the QCD phase diagram is shown in Fig. 1.1.

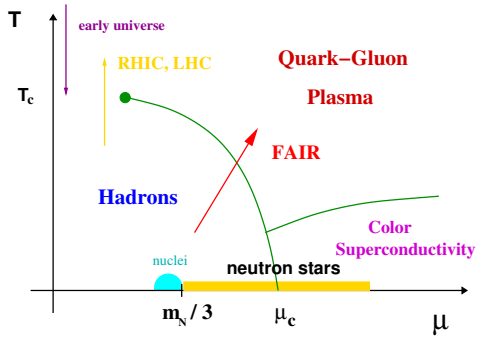

Figure 1.1: Sketch of the QCD phase diagram. The dark green point is the CEP. The dark green lines are first order phase transitions. The crossover region is between the pseudocritical temperature T_c and the CEP. Three different heavy-ion colliders are drawn: RHIC and the Large Hadron Collider (LHC) are operational right now, while the Facility for Antiproton and Ion Research (FAIR) is currently under construction. Sketch taken from Ref. [10].

The strong interaction, which is described by QCD, has some unique characteristics. Quarks are usually confined and therefore need very high baryon chemical potential and/or very high temperatures to become (quasi) free particles inside the QGP phase. Both requirements are not met in our everyday life. High chemical potential can e.g. exist in neutron stars. The temperature needed at low chemical potential to create a QGP, which is in the magnitude of 10^{12} K, is even higher than inside our sun, which is around $1.5 \cdot 10^7$ K, and was there during the first fractions of a second after the Big Bang in the early universe. To investigate the QGP phase experimentally we therefore need very high collision energies to create a QGP through high temperatures and/or baryon chemical potential. Since a QGP only exists for a fraction of a second we can not probe anything directly inside. To overcome this challenge we rely on particles created during chemical freeze-out and we indirectly recreate what happened before in the QGP. This approach therefore needs knowledge about what is happening inside the QGP to interpret the outcome of the experiment correctly.

From the theoretical point of view the strong coupling of QCD needs non-pertubative methods to be investigated outside of some special cases in which

the quarks are asymptotically free particles. The transition region with its CEP is one of those areas where non-pertubative methods are needed.

One of those methods is lattice QCD. It was introduced by Kenneth Geddes Wilson in 1974 [11]. Lattice QCD discretizes space-time by introducing a four dimensional lattice. The inverse distance between neighboring points, the inverse lattice spacing, gives a UV-cutoff, which serves as a regulator. Through the Euclidean space-time formalism we can use Monte-Carlo integration techniques to get meaningful results for systems in equilibrium inside a medium like high temperature QCD. This method unfortunately also has its drawbacks. Because of the so-called sign problem accessing high baryon chemical potential is still an ongoing challenge to overcome. Through the discretization some continuum symmetries get broken to discrete symmetries. Due to the necessary discrete derivatives we also introduce so-called doublers. These are unphysical but identical quarks, which change the results. Removing them is possible but introduces other challenges.

A good way to investigate QCD via lattice QCD is the use of correlation functions. We are especially interested in hadronic correlators. The simplest hadronic correlators are mesonic correlators. With them we want to investigate two things: Our main focus is the anomaly of $U_A(1)$, which will give us the order of the chiral phase transition and therefore information about the potential CEP. Another question we want to address is at which temperature the purely hadronic screening meson states transition into a superposition of free quarks and mesons.

The $U_A(1)$ is an interesting research topic [12–17]. Unlike other symmetries, which are explicitly broken on the level of action or are spontaneously broken, the $U_A(1)$ is an explicitly broken symmetry also by the anomaly. The question whether this explicit breaking vanishes at the transition temperature or not is still ongoing research. The answer to this question has consequences to the CEP and the overall structure of the QCD phase diagram. Former studies [12,16–19] have shown that chiral symmetry and the $U_A(1)$ symmetry get effectively restored at different temperatures for physical quark masses. While the chiral symmetry restoration defines the transition temperature and got restored at that temperature, the $U_A(1)$ symmetry got restored at higher temperature clearly inside the QGP phase. Both symmetries however are also explicitly broken by finite light quark masses. In this work we want to go towards vanishing light quark masses and address if that discrepancy of effective symmetry restoration for $U_A(1)$ to the phase transition temperature is then still valid or if the anomaly of $U_A(1)$ vanishes at the phase transition temperature in the chiral limit.

The CEP is the main focus of many researches. One such research group is the collaboration of the Collaborative Research Center TransRegio 211 (CRC-TR211) of the Deutsche Forschungsgemeinschaft (DFG) in which this research is part of.

The structure of this thesis is as follows: In chapter 2 we give a short introduction to lattice QCD and the theory of this work. In chapter 3 we explain the analysis methods of how we got the results. In chapter 4 we present the results and discuss them. In chapter 5 we present the conclusion of this thesis.

Chapter 2

Introduction to Lattice Quantum Chromodynamics

The interaction of quarks and gluons is described by Quantum Chromodynamics (QCD). The entirety of QCD can mathematically be written through the generating functional. First we need the Lagrangian density of QCD

$$\mathcal{L}[\bar{\psi}(x), \psi(x), A(x)] = \bar{\psi}(x)(i\gamma^\mu D_\mu(x) - m)\psi(x) - \frac{1}{4}F^a_{\mu\nu}(x)F^{a,\mu\nu}(x), \quad (2.1)$$

where $D_\mu = \partial_\mu - igT_aA^a_\mu$ is the covariant derivative, ψ and $\bar{\psi}$ are the quark fields, x is a point in the four dimensional space-time, A are the gluon fields, g is the coupling constant of the strong force, a are color indices, $T_a = \lambda_a/2$ are generators of $SU(3)$, where λ_a are the Gell-Mann matrices and $F_{\mu\nu} = -i[D_\mu, D_\nu]$ is the field strength tensor, where $F_{\mu\nu}(x) = \sum_{a=1}^{8} F^a_{\mu\nu}(x)T_a$. With this Lagrangian density we can get the action of our theory

$$S[A, \psi, \bar{\psi}] = \int dt d^3x \mathcal{L}[\bar{\psi}(x), \psi(x), A(x)]. \quad (2.2)$$

Finally we can write the generating functional of QCD

$$Z[J] = \int \mathcal{D}[\psi, \bar{\psi}]\mathcal{D}[A] \exp(iS[A, \psi, \bar{\psi}] + iS[J]), \quad (2.3)$$

where $S[A, \psi, \bar{\psi}]$ is the QCD action and $S[J]$ is a general source term with current J. If we want to calculate an observable we need to calculate also our generating functional Eq. 2.3. Since a direct analytic solution is not possible, one can use a numerical approach. Due to the high-dimensional integral even for a finite lattice, the configurations necessary for a 4D Ising spin system on a moderate lattice size, which would be a simpler system than QCD, to compute are already around 10^{19728} [20], which is not possible to solve by our current computers. Fortunately, statistical methods can be used to get

reasonable and meaningful results through the use of expectation values of observables on a discrete space-time lattice. This specific method is called lattice QCD and is used in this thesis.

Therefore in the next sections we will explain some important concepts of lattice QCD. For further information see e.g. Ref. [20]. Throughout the whole thesis natural units are used $\hbar = c = 1$.

2.1 Wick rotation

For a straightforward description analogous to statistical physics a so-called Wick rotation needs to be performed. The Wick rotation changes the integration in our action in Eq. 2.2 from real to imaginary time. These actions are also called Minkowski and Euclidean, respectively. This rotation can be done through the identification of two Cauchy integrals: One for the positive and one for the negative values of the temporal extent. Both use a quarter-circle anticlockwise rotation towards the imaginary time axis (first and third quadrant). For a sketch see Fig. 2.1.

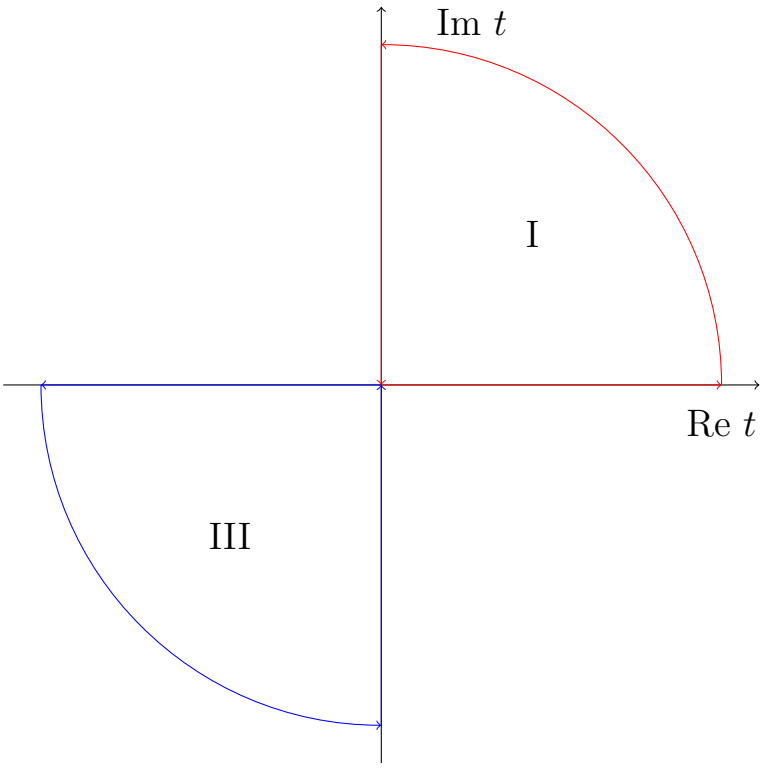

Figure 2.1: Sketch of the two Cauchy integrals for the Wick rotation.

Since these planes should not have any singularities and the fields at any infinite complex time should vanish, it follows for the first quadrant (positive time slice)

$$\int_0^\infty dt \int d^3x \mathcal{L} + \int_{i\infty}^0 dt \int d^3x \mathcal{L} = 0. \tag{2.4}$$

This works analogously for the third quadrant (negative time slice). Using the substitution $t = i\tau$, it directly follows

$$S = \int_{-\infty}^\infty dt \int d^3x \mathcal{L} = i \int_{-\infty}^\infty d\tau \int d^3x \mathcal{L}_\mathrm{E} = iS_\mathrm{E}. \tag{2.5}$$

To distinguish between the two actions S_E will be used for the Euclidian action, i.e. the imaginary time τ is a variable here, not the real time t. Through the substitution $t = i\tau$ we also have to change time-related operators and matrices in the Lagrangian:

$$\begin{aligned} i\partial_t &= -\partial_\tau \\ \gamma_0^E &= \gamma_0^M \equiv \gamma_4 \\ \gamma_i^E &= -\gamma_i^M, \end{aligned} \tag{2.6}$$

where M stands for Minkowski and E for Euclidean.

The relative i from Eq. 2.5 has direct consequences for the partition function

$$Z = \int \mathcal{D}[\psi, \bar{\psi}]\mathcal{D}[A] \exp(iS[A, \psi, \bar{\psi}]) = \int \mathcal{D}[\psi, \bar{\psi}]\mathcal{D}[A] \exp(-S_\mathrm{E}[A, \psi, \bar{\psi}]), \tag{2.7}$$

where $\mathcal{D}[\psi, \bar{\psi}]$ and $\mathcal{D}[A]$ are the measures of all involved fields. For more information on partition functions, see e.g. Ref. [20]. Since the action is by definition a real number, that makes it possible to interpret the term $\exp(-S_\mathrm{E}[A, \psi, \bar{\psi}])$ as a probability if it gets normalized (more on that in section 2.3). A feature of any theory with finite imaginary temporal direction, e.g. lattice QCD, is the introduction of temperature T. It automatically arises in lattice QCD because we have to restrict the space-time integrals of our Euclidean action to finite imaginary times (and space). It follows

$$\int_{-\infty}^\infty d\tau \to \int_0^\beta d\tau, \tag{2.8}$$

where $\beta = \frac{1}{T}$ is the inverse temperature. The symbol β is also used for the inverse gauge coupling; thus, to avoid confusion, this use of β will only be used in this section and in section 2.3 where the connection to temperature will be shown in more detail. In a similar manner baryon chemical potential μ_B can also be introduced in a statistical mechanical way. More on that in section 2.3. In the next section 2.2 a closer look into the discretization of QCD will be given, which leads to lattice QCD.

2.2 Discretization of QCD

To calculate observables directly from a quantum field theory in a well-defined way we need an ultraviolet regulator. A regulator makes expressions finite. There are different ways to regulate a quantum field theory. In this thesis we want to regulate QCD via lattice. To do so we replace the original continuous space by a finite lattice

$$x \Rightarrow a_x n_x, \tag{2.9}$$

where $n_x = 0, 1, ..., N_x - 1$ and a_x is the lattice spacing in x-direction. Usually it is $N_x = N_y = N_z \equiv N_s$ and $a_x = a_y = a_z \equiv a_s (\equiv a)$, which makes this 3D lattice a box. We want to use that kind of lattice here as well. For a finite box boundary conditions have to be set. We chose periodic boundary conditions, i.e. we identify $n_i = N_s$ with $n_i = 0$ for $i = x, y, z$ or for simplicity $i = 1, 2, 3$.

The Euclidean action for the continuum reads

$$\begin{aligned} S_{\mathrm{E}} =& S_G[A] + S_F[A, \psi, \bar{\psi}] \\ =& \frac{1}{4g^2} \sum_{j=1}^{8} \int d^4x F_{\mu\nu}^{(j)}(x) F_{\mu\nu}^{(j)}(x) \\ &+ \int d^4x \bar{\psi}(x)(\gamma_\mu(\partial_\mu + iA_\mu(x)) + m)\psi(x), \end{aligned} \tag{2.10}$$

where S_G is the gluonic part and S_F is the fermionic part of the action, g is the bare gauge coupling and $F_{\mu\nu}^{(j)}(x) = \partial_\mu A_\nu^{(j)}(x) - \partial_\nu A_\mu^{(j)}(x) - f_{jik} A_\mu^{(i)}(x) A_\nu^{(k)}(x)$ is the field strength tensor with color index j. First let us take care of the spatial derivatives of Eq. 2.10. Using the Taylor series expansion of the fields these derivatives can be written as

$$\partial_i \psi(\vec{x}, \tau) \to \frac{\psi(\vec{n} + \hat{i}, n_\tau) - \psi(\vec{n} - \hat{i}, n_\tau)}{2a} + \mathcal{O}(a^2), \tag{2.11}$$

where $\vec{x}$ is a 3D vector of continuum space, $\vec{n}$ is the same 3D vector of lattice space (cf. Eq. 2.9) and $\hat{i}$ is the unit vector in the i-direction. To complete the discretization we have to take care of the time direction as well. To simplify the theory we use an analogous derivative and the same lattice spacing in Euclidean time direction

$$\partial_\tau \psi(x) \to \frac{\psi(\vec{n}, n_\tau + \hat{\tau}) - \psi(\vec{n}, n_\tau - \hat{\tau})}{2a} + \mathcal{O}(a^2), \tag{2.12}$$

where x is a 4D vector of continuum space-time, n_τ is a point of lattice time and $\hat{\tau}$ is the unit vector in the imaginary time direction. We will combine $\vec{n}$ and n_τ to n as a 4D vector of lattice space-time. The maximum number

of lattice points in the temporal direction is denoted as N_τ. The integral in space-time will accordingly be replaced by

$$\int d^4x \to a^4 \sum_{n\in\Lambda_4}, \tag{2.13}$$

where Λ_4 denotes the 4D finite lattice with its $N_s^3 \times N_\tau$ lattice points. The states related to the fields stay orthogonal and complete:

$$\begin{aligned} \langle\psi'|\psi\rangle =& \delta(\psi'-\psi) = \prod_{n\in\Lambda_4} \delta(\psi'(n)-\psi(n)), \\ \mathbb{1} =& \int_{-\infty}^{\infty} \mathcal{D}\psi \, |\psi\rangle \langle\psi| \text{ with } \mathcal{D}\psi = \prod_{n\in\Lambda_4} d\psi(n). \end{aligned} \tag{2.14}$$

For temperatures $T > 0$ it is common to have $N_s > N_\tau$. This reduces finite volume effects. It is not necessary to have the same lattice spacing in spatial and temporal direction, but we use it in this thesis. For the temporal direction we chose anti-periodic boundary conditions for fermions and periodic boundary conditions for gauge fields, because the fermionic fields follow the anticommutation relation, while the bosonic gauge fields follow the commutation relation. For our lattice QCD calculations at high temperatures, where the lowest Matsubara frequencies dominant, these boundary conditions are especially important since their Matsubara frequencies differ depending on their fermionic or bosonic nature. The gauge fields are described in the next paragraph. For further reading on the discretization via lattice, see e.g. Ref. [20].

An important change to the action happens if we switch from continuum to discrete action. The gluon fields become elements of the gauge group U and are not elements of the algebra A anymore. That is due to gauge invariance of the derivative term in the fermionic part [20]. Since in the discrete description not all fields are evaluated on same space-time points anymore, the gauge fields U have to be introduced to conserve gauge invariance. Since U connects fields with different space-time points they are also called link variables. For the gauge and fermionic part of the action S_G and S_F different discretizations are possible. For the gauge part of the action the starting point is the Wilson gauge action, which reads

$$S_G[U] = \frac{2}{g^2} \sum_{n\in\Lambda} \sum_{\mu<\nu} \Re(\mathrm{tr}[1 - U_{\mu\nu}(n)]), \tag{2.15}$$

where

$$U_{\mu\nu}(n) = U_\mu(n) U_\nu(n+\hat{\mu}) U_{-\mu}(n+\hat{\mu}+\hat{\nu}) U_{-\nu}(n+\hat{\nu}) \tag{2.16}$$

is the shortest, non-trivial closed loop on a lattice, the so-called plaquette. For our calculations we use the Symanzik improved gluon action as e.g. in [8].

The starting point for all fermionic actions is the so-called naive fermion discretization for a single flavor

$$S_F[U,\psi,\bar{\psi}] = a^4 \sum_{n\in\Lambda} \bar{\psi}(n) \left(\sum_{\mu=1}^{4} \gamma_\mu \frac{U_\mu(n)\psi(n+\hat{\mu}) - U_{-\mu}(n)\psi(n-\hat{\mu})}{2a} + m_0\psi(n) \right), \tag{2.17}$$

where $U_\mu(n)$ are link variables connecting the starting space-time point n with its neighbor in positive μ-direction. For the fermionic part more details will be given in section 2.5.

By discretizing and limiting the space-time integrals to finite integrals for calculations we introduce finite volume effects and a cut-off through the lattice spacing a. These corrections however should become small to draw conclusions for real-life physics. To do that the lattice spacing a should be as small as possible in the beginning to neglect higher order corrections so that only lowest order corrections have to be dealt with. To quantify and reduce those corrections an analysis has to be done where different limits have to be taken. This includes the infinite volume limit, also known as thermodynamic limit, where $N_s \to \infty$ is taken by suitable ansätze. Next, one takes the continuum limit where $a \to 0$ by suitable ansätze to transition from the lattice back to the continuum again while keeping some physics constant. Since we remove the regulator in this step we need renormalizable observables for the continuum limit extrapolation. For our analysis the thermodynamic and continuum limit however have to be taken at fixed temperature T of the system, which makes the continuum limit $a \to 0$ equal to $N_\tau \to \infty$.

In the next section 2.3 a closer look into the connection of the Euclidean formulation to statistical mechanics will be given. Moreover the introduction of temperature as well as the starting point of lattice calculations will be presented.

2.3 Statistical mechanics

In this section we will make the connection of our lattice QCD description and statistical mechanics. The Euclidean correlator is defined as [20]

$$\langle O_2(t)O_1(0)\rangle_\beta = \frac{1}{Z_\beta}\mathrm{tr}\left[\exp(-(\beta-t)\hat{H})\hat{O}_2 \exp(-t\hat{H})\hat{O}_1 \right], \tag{2.18}$$

where the normalization factor Z_β is the partition function given by

$$Z_\beta = \mathrm{tr}\left[\exp(-\beta\hat{H}) \right], \tag{2.19}$$

where t is the Euclidean time distance, β is defined as the maximum distance in time direction (same β as in section 2.1), $\hat{O}$ are operators for observables and $\hat{H}$ is the Hamiltonian of the system. Inserting completeness relations with energy eigenstates, pulling out the largest factor $\exp(-TE_0)$, setting the vacuum energy $E_0 = 0$ and the maximum time distance $\beta = \infty$, leads to

$$\lim_{\beta\to\infty} \langle O_2(t)O_1(0)\rangle_\beta = \sum_n \langle 0|\hat{O}_2|n\rangle\langle n|\hat{O}_1|0\rangle \exp(-tE_n), \tag{2.20}$$

where E_n are the different energy eigenvalues of the Hamiltonian $\hat{H}$ and $|n\rangle$ are the corresponding eigenstates, see e.g. Ref. [20] for the individual steps.

We can write the Euclidean correlator of Eq. 2.18 also in another representation via path integrals. Beginning from the right-hand side of Eq. 2.18 the Hamiltonian will be written in terms of field operators, then the completeness relations of these field operators together with the Trotter formula result in

$$\begin{aligned}\langle O_2(t_1 = t)O_1(t_0 = 0)\rangle_\beta =& \frac{1}{Z_\beta}\int \mathcal{D}[\psi,\bar{\psi}]\mathcal{D}[U]\exp(-S_\mathrm{E}[U,\psi,\bar{\psi}]) \\ & \times O_2[U,\psi,\bar{\psi}](t_1 = t)O_1[U,\psi,\bar{\psi}](t_0 = 0),\end{aligned} \tag{2.21}$$

where U denotes that this is already in lattice discretization. A comparison of Eq. 2.21 with the expectation value from statistical mechanics, e.g. a spin system with

$$\langle O\rangle = \frac{1}{Z}\sum_s \exp(-\beta H[s])O[s], \tag{2.22}$$

where s represents a spin configuration, leads to the replacement of the Boltzmann factor $\exp(-\beta H[s])$ with the weight factor $\exp(-S_\mathrm{E}[U,\psi,\bar{\psi}])$. Because of this close connection Z_β, which is the generating functional of our field theory, is therefore also called the partition function. If you compare Eq. 2.19 with the interpretation of the same equation as in statistical mechanics, it follows that $\beta = 1/(k_B T)$, where k_B is the Boltzmann constant and T the temperature of the system. Thus the right hand side of Eq. 2.20 is in the zero temperature vacuum. Since we use natural units ($k_B = 1$) the maximum distance in time direction β is just the inverse of temperature T.

Through our lattice discretization we limit our integration in the Euclidean time direction to the maximum distance $\beta = aN_\tau$ and therefore the temperature T results from limiting the Euclidean time integral to some finite extent

$$\beta = aN_\tau = \frac{1}{T}. \tag{2.23}$$

By knowing the lattice spacing a of our system we can therefore directly set the temperature T. Because a and N_τ do not change for one lattice setup the temperature T is fixed for that system. Flipping that argument around

we see how the continuum limit works. Having a fixed temperature T and increasing N_τ towards infinity by having different lattice setups leads to a vanishing lattice spacing a. Note that for finite extent β the Fourier transformation leads to discrete energy values since energy is the Fourier transform of time. These values are called Matsubara frequencies.

Another connection to statistical mechanics can be found if we look at chemical potential μ_B. The introduction of chemical potential for the lattice is however not straightforward and will break γ_5-hermiticity of the Dirac operator for finite μ_B and therefore our Boltzmann weight becomes complex. That is the so-called sign problem. In this thesis however we do not use any chemical potential and therefore it is only noted here that these challenges exist and are still part of ongoing research. For more details see e.g. Ref. [20]. In the next section we will have a closer look into ways to calculate the partition function and we also want to build the basis to calculate the correlators later.

2.4 Calculating the Euclidean correlator

To calculate Euclidean correlators we have to perform the high-dimensional integration of Eq. 2.21. Since the Euclidean action of the partition function is real and therefore the Boltzmann weight $\exp(-S_\mathrm{E}) \geq 0$, an interpretation of that weight as a probability can be made. That can be used to integrate our Euclidean correlator via Monte Carlo integration with samples derived from Markov chains. Next we give a short overview of how that method can be used here.

Monte Carlo integration is a very powerful tool for integrating high-dimensional integrals. The simplified idea is to take random numbers or vectors x_n inside the integration interval, calculate the observable at these points and average over all that

$$\underbrace{\langle f \rangle}_{\substack{\text{expectation}\\ \text{value}}} = \underbrace{\frac{1}{b-a}}_{\text{normalization}} \int_a^b \underbrace{\mathrm{d}x}_{\text{differential}} \underbrace{1}_{\text{weight}} f(x) = \lim_{N\to\infty} \frac{1}{N} \sum_{n=1}^{N} f(x_n), \quad (2.24)$$

where f is the observable. By limiting the number N of those random numbers or vectors x_n we achieve an approximation of the correct integral. That is called Monte Carlo Sampling. If we have a weight ρ like the Boltzmann weight $\exp(-S_\mathrm{E})$ in Eq. 2.21 we can sample random numbers or vectors ac-

cording to that weight

$$\underbrace{\langle f \rangle_\rho}_{\substack{\text{expectation}\\ \text{value}}} = \underbrace{\frac{1}{\int \mathrm{d}x \rho(x)}}_{\text{normalization}} \int \underbrace{\mathrm{d}x}_{\text{differential}} \underbrace{\rho(x)}_{\text{weight}} f(x) = \lim_{N\to\infty} \frac{1}{N} \sum_{n=1}^{N} f(x_n), \quad (2.25)$$

which is called Monte Carlo Importance Sampling if we again limit the number N of the random numbers or vectors x_n.

The tricky part is to get these sets of random numbers or vectors x_n for our high-dimensional integral. In lattice QCD we integrate over complete sets of gauge fields. We call a complete set of gauge fields a configuration; those individual gauge fields would be equivalent to individual entries of a high-dimensional vector, which we integrate over in the Monte Carlo importance sampling. To find these configurations U_n (not to be confused with the indiviual gauge fields U_μ), which follow a probability distribution, we start from an arbitrary configuration U_0 and then construct a stochastic sequence of configurations, which follows eventually the equilibrium distribution $P(U)$. That sequence is called a Markov chain. There are specific conditions for Markov chains, which are related to the transition probability $T(U'|U) = P(U'|U)$, which describes the probability of transition to U' in the chain starting from U. First it has to be a probability, which means

$$0 \leq T(U'|U) \leq 1. \quad (2.26)$$

That is the reason why our weight $\exp(-S_\mathrm{E})$ should be real and positive, which is the main obstacle for exploring finite baryon chemical potential lattice QCD calculations where that is in general not the case. Normalization and the Boltzmann weight together result here in a probability. The second condition is that all configurations should be reachable from every other configuration

$$0 < T(U'|U). \quad (2.27)$$

That is called ergodicity and it is also directly fulfilled by our weight $\exp(-S_\mathrm{E})$. The third condition is completeness, which is

$$\sum_{U'} T(U'|U) = 1. \quad (2.28)$$

The fourth and last condition is that each step of the Markov chain obeys the balance equation

$$\sum_{U} T(U'|U) P(U) \stackrel{!}{=} \sum_{U} T(U|U') P(U'), \quad (2.29)$$

with

$$P(U') = \sum_{U} T(U'|U). \quad (2.30)$$

One specific and mostly used solution to the balance equation is

$$T(U'|U)P(U) = T(U|U')P(U'), \tag{2.31}$$

which is the so-called detailed balance condition. With that, one major technical issue remains: To advance the Markov chain from one configuration to another we need an algorithm, which fulfills the balance equation. Here we have many possibilities. Some algorithms are e.g. the heat bath and hybrid Monte Carlo algorithm.

Let us shortly look into Eq. 2.21 in a bit more detail. Comparing it with the generating functional Eq. 2.3 after the Wick rotation using Grassmann-valued fields we can create so-called n-point functions in lattice QCD. This process leads to Wick's theorem [20]

$$\langle \eta_{i_1}\bar{\eta}_{j_1}...\eta_{i_n}\bar{\eta}_{j_n}\rangle_F = (-1)^n \sum_{P(1,2,...,n)} \mathrm{sign}(P)(M^{-1})_{i_1 j_{P_1}}(M^{-1})_{i_2 j_{P_2}}...(M^{-1})_{i_n j_{P_n}}, \tag{2.32}$$

where F refers to the integration over the Grassmann-valued fields (in that case the fermion fields), η are Grassmann-valued fields, P refers to the permutation, where sign is the 'sign' of that permutation, and $M = -a^4(\gamma_\mu D^\mu + m_0)$, where M is the Dirac operator and a is the lattice spacing. We summarize $-a^4\gamma_\mu D^\mu = D$ and redefine $m \equiv -a^4 m_0$. From that side we therefore only need to create suitable gauge configurations according to the weight $\exp(-S_\mathrm{E})$ since after the integration over the Grassmann-valued fields only the integration over gauge fields will survive. It can be shown that [20]

$$\langle\langle O\rangle_F\rangle_G = \frac{1}{Z}\int \mathcal{D}[U]\exp(-S_G[U])\det[M[U]]O[U], \tag{2.33}$$

where O is an observable, S_G is the gauge action and $\det[M] = Z_F[U] = \int \mathcal{D}[\psi,\bar{\psi}]\exp(-S_F[\psi,\bar{\psi},U])$ is the fermion determinant, where M is again the Dirac operator. A configuration distribution according to the weight

$$w[U] = \frac{1}{Z}\exp(-S_G[U])\det[M[U]] \tag{2.34}$$

will create a gluonic and fermionic background on sea level while the observable $O[U]$ acts on valence level. We usually want the generating action to be the same on sea and valence level. For our action, the fermion determinants are positive for non-zero quark masses and it therefore can be used as probability weight. Setting all fermion determinants to unity by hand here is called the quenched approximation of QCD while taking them correctly into account is called dynamical QCD. Since the fermion determinants are part of the weight they have to be calculated in every step in the Markov chain.

Since we exclusively use dynamical QCD for our calculations in this thesis let us have a closer look into how the fermion determinants come into play.

The central idea is to abuse a close analogy between bosonic and fermionic Gaussian integrals. The close relation gives us the possibility to use pseudofermions instead of normal Grassmann-valued fermion fields. Those Gaussian integrals over pseudofermion fields can then be solved more easily. A way to include the fermion determinant(s) for the weight is by introducing them as an effective fermion action [20]

$$\det[M[U]] = \exp(\mathrm{tr}[\ln(M[U])]) \equiv \exp(-S_F^{\mathrm{eff}}[U]), \tag{2.35}$$

where S_F^{eff} is the effective fermion action, which is independent of the quark fields ψ and $\bar{\psi}$. This leads to a total Boltzmann weight of

$$\exp(-S_G[U] - S_F^{\mathrm{eff}}[U]), \tag{2.36}$$

where $S_G[U]$ is the gauge action. Because an update of gauge fields only effects their nearest neighbors this part of the action is called local. The effective fermion action on the other hand connects with all gauge variables of the system and thus locality is unfortunately not fulfilled for the effective fermion action. That means that the Metropolis algorithm with single link variable is not optimal regarding computing time for dynamical QCD. That is why we use the Rational Hybrid Monte Carlo (RHMC) algorithm instead.

The Dirac operator highly depends on the fermion type used. We will have a closer look into different fermion types in section 2.5. Since a lot of the computional effort for dynamical QCD is spent solving sparse linear systems, we first want to cover the methods to solve them more efficiently. Depending on the observable that we want to calculate with our correlator we might have to calculate (inverse) Dirac operators there as well. We will have a look into our special case of mesonic correlators in section 2.7.

To evaluate expectation values of hadronic correlators usually requires constructing quark propagators, which means the inverse of M, obeying the equation [21]

$$M^{-1}M = MM^{-1} = \mathbf{1}. \tag{2.37}$$

Because M is a square matrix of dimension a few times the lattice volume, but only has non-zero entries of the order volume, that is a problem of sparse matrix inversion. Therefore we construct $g = M^{-1}h$ for a selected source vector h by solving

$$Mg = h. \tag{2.38}$$

In subsection 2.4.2 we give a short introduction to the Conjugate Gradient (CG) method, which we use to solve the sparse linear system of Eq. 2.38 to solve for the quark propagators. For our RHMC algorithm we need the more efficient multi-shift CG solver. For the details on that we refer to Ref. [21]. Before we jump into the CG method, let us first take advantage of the special structure of our Dirac matrix.

2.4.1 Even-odd preconditioning

Before we solve our sparse linear system, we want to reduce the size of the sparse linear system. The LU preconditioning takes advantage of the special structure of the staggered Dirac matrix (which we will use in this thesis), which cuts the problem size roughly in half. Decomposing into even and odd lattice sites, the Dirac matrix has the block structure

$$M = \begin{pmatrix} R_e & D_{eo} \\ D_{oe} & R_o \end{pmatrix}, \tag{2.39}$$

where the upper row and left column refer to even sites and the lower row and right column to odd. For staggered fermions we have $R_e = R_o = m$ and $D_{eo} = D = -D_{oe}^\dagger$ [21]. We will enter these variables now. For the general calculation, see Ref. [21]. We can now write the decomposition of M as

$$M = \underbrace{\begin{pmatrix} 1 & D/m \\ 0 & 1 \end{pmatrix}}_{U} \underbrace{\begin{pmatrix} m + DD^\dagger/m & 0 \\ 0 & m \end{pmatrix}}_{A} \underbrace{\begin{pmatrix} 1 & 0 \\ -D^\dagger/m & 1 \end{pmatrix}}_{L}. \tag{2.40}$$

Then we get $L^{-1} = \begin{pmatrix} 1 & 0 \\ D^\dagger/m & 1 \end{pmatrix}$ and $U^{-1} = \begin{pmatrix} 1 & -D/m \\ 0 & 1 \end{pmatrix}$ trivially. Therefore we continue with

$$Mg = UALg = h \tag{2.41}$$

and define $Lg = x$ and $U^{-1}h = b$. That brings us to

$$\underbrace{\begin{pmatrix} A_{ee} & 0 \\ 0 & m \end{pmatrix}}_{A} \underbrace{\begin{pmatrix} x_e \\ x_o \end{pmatrix}}_{Lg} = \underbrace{\begin{pmatrix} b_e \\ b_o \end{pmatrix}}_{U^{-1}h}, \tag{2.42}$$

where the matrix $A_{ee} = (m^2 + DD^\dagger)/m$ is hermitian positive definite and we have split the vector in even-site and odd-site components. Since the solution on the odd sites is trivial, we only have to solve a sparse system on the even sites. When we solved for x, we get our desired solution $g = L^{-1}x$ trivially. Thus we have reduced the problem size roughly in half.

In the next subsection we will go over the conjugate gradient method to solve a sparse linear system; in the case of Eq. 2.42 for x.

2.4.2 Conjugate gradient

Now let us have a short look into a Conjugate Gradient (CG) method [20], which we could use to solve for the determinant over the Dirac operator in

the RHMC algorithm but we can also use it to solve quark propagators in mesonic correlators. Because $M^\dagger M$ is hermitian positive definite, we can invert the Dirac matrix M by inverting $M^\dagger M$ and multiply it with $M^\dagger$ [21]. This inversion is needed in both cases and the CG method is one of, if not, the fastest method to do so for staggered fermions.

For a real, symmetric, positive definite $N \times N$ matrix A

$$Q(x) = \frac{1}{2} x^T A x - x^T b \tag{2.43}$$

is a positive definite quadratic form with its minimum at x^*, so that the gradient vanishes,

$$\partial Q(x)|_{x^*} = Ax^* - b = 0. \tag{2.44}$$

Thus x^* is the solution for the system $Ax = b$. The CG method now iterates $x^{(i)}$ in a way so that in each step $Q(x^{(i)} + \alpha_i p^{(i)})$ is minimized as a function with $p^{(i)}$ being a search vector and α_i being a real parameter. The search vector is made orthogonal to $Ap^{(i-1)}$ and all previous $Ap^{(j)}$. All those search vectors then span a Krylov subspace. Starting from a random vector $x^{(0)}$ it will take N iterations to reach the minimum x^*, where N is the dimension of the matrix A. By calculating the norm $||Ax^{(i)} - b||$ and comparing that to an accuracy ϵ the algorithm can be sped up if the norm falls below ϵ.

In the next section 2.5 we present some types of fermions. We discuss their advantages and disadvantages and explain why we chose staggered fermions.

2.5 Different fermion types

While the gluonic part of the action is usually the same (except for improvements regarding cut-off effects), the fermionic part may differ depending on the problem at hand. The problem of the naive fermion discretization is that it introduces 15 so-called doublers. Doublers are unphysical particles with the exact same mass as the physical particle. These doublers can appear in discrete fermion actions like the naive action and will in the case of the naive action not even disappear after the continuum limit has been taken, but for other fermion actions they might disappear in the continuum limit. Nonetheless transferring from discrete to continuum physics is no easy task, especially if the probed part of physics is only correct in the latter. For this reason and because of large cut-off effects the naive discretization is not used. On the other hand different fermion types might get rid of the doubler problem but will introduce another problem because of a no-go theorem [22].

For instance the Wilson fermions will get rid of doublers by introducing an extra term to increase the mass of doublers. This extra term also vanishes in the continuum limit and while doing so also increases the doubler masses to infinity. A downside of Wilson fermions is that this extra term explicitly breaks chiral symmetry.

Another fermion type is overlap fermions. They also get rid of doublers but keep chiral symmetry intact by solving the Ginsparg-Wilson equation, while losing ultralocality, which gets restored again in the continuum limit. Another downside is the high numerical cost compared to other fermion types.

Domain-wall fermions are also numerically demanding but less so than overlap fermions. Here a 5^{th} dimension and a modified Dirac operator is introduced. They as well solve the Ginsparg-Wilson equation and therefore have chiral symmetry already at finite lattice spacing in the limit of infinite lattice points in the 5^{th} dimension. They are also free of doublers. Since the no-go theorem [22] assumed even-numbered dimensions, the introduction of a 5^{th} dimension might circumvent the restrictions of this theorem. Nonetheless a downside is that domain-wall fermions only recover full chiral symmetry in the limit of infinite length in the 5^{th} dimension.

Lastly we want to mention staggered fermions. They are an interesting fermion type since they are numerically easy to compute and restore partly chiral symmetry while reducing the doublers from 15 to 3. Through rooting the doublers can then be completely eliminated [23]. As we will use staggered fermions for these reasons in this thesis we will have a closer look into that fermion type in the next section 2.6.

2.6 Staggered fermions

In this thesis staggered fermions have been exclusively used. For further reading see e.g. Ref. [20, 21]. As mentioned in section 2.5 staggered fermions preserve a remnant chiral symmetry and reduce the 16-fold degeneracy of the naive fermion action to a four quark theory while reducing computational cost. This four quark theory in turn will be reduced to a one quark theory by taking the fourth root of the staggered fermion determinant [23]. This process is called rooting. During the derivation of staggered fermions we need to project four identical copies to a single-component field. This projection onto a single-component field in Dirac space unfortunately breaks some symmetries and reduces the doubler symmetry to the new taste symmetry [24–26]. We will come back to that when it is necessary.

The main idea of staggered fermions is to transform the quark fields in a way that their original Dirac space becomes diagonal, which in turn speeds up the computation. The staggered transformation is defined as

$$\psi(n) = \gamma_1^{n_1}\gamma_2^{n_2}\gamma_3^{n_3}\gamma_4^{n_4}X(n) \qquad \bar{\psi}(n) = \bar{X}(n)\gamma_4^{n_4}\gamma_3^{n_3}\gamma_2^{n_2}\gamma_1^{n_1}, \tag{2.45}$$

where γ are the Dirac matrices, n_i are the coordinates of the lattice sites, ψ and $\bar{\psi}$ are the quark fields. If these transformed fields are put into the naive

discretized fermion action (Eq. 2.17) all γ_μ cancel, e.g.

$$\begin{aligned}\bar{\psi}(n)\gamma_3\psi(n\pm\hat{3}) =&\bar{X}(n)\gamma_4^{n_4}\gamma_3^{n_3}\gamma_2^{n_2}\gamma_1^{n_1}\gamma_3\gamma_1^{n_1}\gamma_2^{n_2}\gamma_3^{n_3\pm1}\gamma_4^{n_4}X(n)\\ =&(-1)^{n_1+n_2}\bar{X}(n)\gamma_4^{n_4}\gamma_3^{n_3}\gamma_2^{n_2}\gamma_1^{n_1}\gamma_1^{n_1}\gamma_2^{n_2}\gamma_3\gamma_3^{n_3\pm1}\gamma_4^{n_4}X(n)\\ =&(-1)^{n_1+n_2}\bar{X}(n)\gamma_4^{n_4}\gamma_3^{n_3}\gamma_3\gamma_3^{n_3\pm1}\gamma_4^{n_4}X(n)\\ =&(-1)^{n_1+n_2}\bar{X}(n)\mathbb{1}X(n)\end{aligned} \tag{2.46}$$

for the 3-direction by using the anticommutation relation of Dirac matrices $\{\gamma_\mu,\gamma_\nu\}=2\delta_{\mu\nu}I_4$. Therefore we get

$$S_F[\chi,\bar{\chi}]=a^4\sum_{n\in\Lambda}\bar{\chi}(n)\left(\sum_{\mu=1}^{4}\eta_\mu(n)\frac{U_\mu(n)\chi(n+\hat{\mu})-U_\mu^\dagger(n-\hat{\mu})\chi(n-\hat{\mu})}{2a}+m_0\chi(n)\right), \tag{2.47}$$

where η_μ is the so-called staggered phase factor defined as

$$\eta_\mu(n)=(-1)^{\sum_{\nu<\mu}n_\nu}, \tag{2.48}$$

with $\eta_1(n)=1$, χ and $\bar{\chi}$ are Grassmann-valued fields that are, except for the Dirac structure which is already omitted, identical to X and $\bar{X}$. That projection was done here since it only consists of a diagonal with ones in Dirac space. Because the fields in the staggered action (Eq. 2.47) omit three of the four identical fields in Dirac space we expect therefore to have only a quarter of quark flavors, i.e. 4 instead of 16. We will have a closer look into the number of quark flavors later in this section. The projection onto a scalar Dirac space has some hidden side-effects on the overall structure of this theory. One hidden side-effect is in the usual lattice translation symmetry [23]

$$t_\mu:\begin{cases}\psi(n)\mapsto\psi(n+\mu)\Rightarrow X(n)\mapsto\zeta_\mu(n)\gamma_\mu X(n+\mu)\\ \bar{\psi}(n)\mapsto\bar{\psi}(n+\mu)\Rightarrow\bar{X}(n)\mapsto\zeta_\mu(n)\bar{X}(n+\mu)\gamma_\mu\end{cases}, \tag{2.49}$$

where

$$\zeta_\mu(n)=(-1)^{\sum_{\nu>\mu}n_\nu}, \tag{2.50}$$

$\bar{X}$ and X are the original fields with diagonal Dirac structure after the staggered transformation. Translations would need to also handle a change in Dirac structure for staggered fermions. Due to the gamma matrix in Eq. 2.49, the projection from X to χ therefore does not commute with lattice translation symmetry. By using the doubling symmetry created by

$$B_\mu(n)=\gamma_\mu\gamma_5(-1)^{n_\mu}, \tag{2.51}$$

with $\gamma_5=\gamma_1\gamma_2\gamma_3\gamma_4$, and all its combinations we can form a combination of translation and doubling called shift, which commutes with our projection

from X to χ

$$S_\mu : \begin{cases} \psi(n) \mapsto -iB_\mu B_5 \psi(n+\mu) \Rightarrow \chi(n) \mapsto \zeta_\mu(n)\chi(n+\mu) \\ \bar{\psi}(n) \mapsto -i\bar{\psi}(n+\mu) B_\mu B_5 \Rightarrow \bar{\chi}(n) \mapsto \zeta_\mu(n)\bar{\chi}(n+\mu) \\ U_\nu(n) \mapsto U_\nu(n+\mu), \qquad \forall\nu \end{cases}, \tag{2.52}$$

where $B_5(n) = i\gamma_5\eta_5(n)$.

What happened so far? The original Dirac structure is distributed over the hypercube instead of being written explicitly in the action. A simple phase factor $\eta_\mu(n)$ replaced γ_μ in the action. Computing staggered fermions is therefore numerically inexpensive because of this simple Dirac structure but requires some effort in understanding the non-trivial consequences. We need e.g. the shift symmetry in order to project X and $\bar{X}$ to χ and $\bar{\chi}$. The shift symmetry replaces and merges the doubling symmetry and the translation symmetry from the original theory. Shift transformations anti-commute with shift transformations in different directions, i.e. $S_\mu S_\nu = -S_\nu S_\mu$ for $\nu \neq \mu$. Of 16 identical quarks from the naive action, i.e. the one physical quark and his 15 doublers connected by the doubling symmetry, we expect that only 4 will survive after discarding the identical copies by projecting X and $\bar{X}$ to χ and $\bar{\chi}$. Since the original doubling symmetry is gone due to merging with the translation symmetry, the amount of doublers in this theory is not clear at this point. After the next paragraph we will look into that and we will see that a new quantum number named taste takes over this role and has 4 possible values. Therefore we will have 4 quark tastes in this theory.

Besides the inexpensive numerical computation, another advantage of staggered fermions is the remnant of chiral symmetry. The $U_A(1)$ rotation before the projection is

$$\psi' = \exp(i\alpha\gamma_5 \mathbb{1})\psi \qquad\qquad \bar{\psi}' = \bar{\psi}\exp(i\alpha\gamma_5\mathbb{1}), \tag{2.53}$$

where $\alpha \in \mathbb{R}$ is the rotation angle and γ_5 is the fifth gamma matrix. If we combine this transformation together with the staggered transformation (Eq. 2.45) we get for a bilinear

$$\begin{aligned} \bar{\psi}'(n)\gamma_5\psi'(n) =& \bar{X}(n)\gamma_4^{n_4}\gamma_3^{n_3}\gamma_2^{n_2}\gamma_1^{n_1}(\cos(\alpha) + i\gamma_5\sin(\alpha)) \\ & \times \gamma_5(\cos(\alpha) + i\gamma_5\sin(\alpha))\gamma_1^{n_1}\gamma_2^{n_2}\gamma_3^{n_3}\gamma_4^{n_4}X(n) \\ =& \bar{X}(n)\gamma_4^{n_4}\gamma_3^{n_3}\gamma_2^{n_2}\gamma_1^{n_1}(2i\sin(\alpha)\cos(\alpha) \\ & + \gamma_5(\cos^2(\alpha) - \sin^2(\alpha)))\gamma_1^{n_1}\gamma_2^{n_2}\gamma_3^{n_3}\gamma_4^{n_4}X(n) \\ =& 2i\sin(\alpha)\cos(\alpha)\bar{X}(n)X(n) \\ & + (\cos^2(\alpha) - \sin^2(\alpha))\eta_5(n)\bar{X}(n)\gamma_5 X(n). \end{aligned} \tag{2.54}$$

For $\alpha = 0$ we get the original pseudoscalar bilinear $\eta_5(n)\bar{X}(n)\gamma_5 X(n)$, for an angle $\alpha = \frac{\pi}{4}$ we rotate to a scalar bilinear $i\bar{X}(n)X(n)$. If we would project now X and $\bar{X}$ to χ and $\bar{\chi}$ also in the bilinear by omitting the gamma matrix, we expect that the staggered phase factor $\eta_5(n)$ takes over the role of γ_5 and therefore a remnant chiral symmetry remains in the action. We will go into more details on that in section 2.8.

After distributing the Dirac structure over the hypercube we have to address the question of how to construct hadron interpolators and their corresponding correlators with definite spin and parity. Before we can address that we first need to understand how many and what kind of quarks the staggered action from Eq. 2.47 describes and which symmetries relate to them.

To make the study more transparent we look at the free case $U_\mu(n) = 1$. Next our 4D hypercube will be split into 16 4D sub-hypercubes. For that let us assume that the number of lattice points in every direction N_μ is even and labeled as $n_\mu = 0, 1, ..., N_\mu - 1$. Then h_μ labels points in every sub-hypercube and s_μ labels different sub-hypercubes, i.e. if $s_\mu \neq 0$ for any μ it is a point of a neighboring sub-hypercube of $s_\mu = 0$. It is

$$n_\mu = 2h_\mu + s_\mu, \tag{2.55}$$

with $h_\mu = \{0, 1, ..., \frac{N_\mu}{2} - 1\}$ and $s_\mu = \{0, 1\}$. The staggered phase factor then only depends on the vector s since

$$\eta_\mu(n) = \eta_\mu(2h + s) = \eta_\mu(s). \tag{2.56}$$

We define 4×4 matrices

$$\Gamma^{(s)} = \gamma_1^{s_1}\gamma_2^{s_2}\gamma_3^{s_3}\gamma_4^{s_4}. \tag{2.57}$$

Two important relations for these Γ matrices are

$$\frac{1}{4}\mathrm{tr}[\Gamma^{(s)\dagger}\Gamma^{(s')}] = \delta_{ss'}, \quad \frac{1}{4}\sum_s \Gamma^{(s)*}_{ba}\Gamma^{(s)}_{b'a'} = \delta_{aa'}\delta_{bb'}. \tag{2.58}$$

With all this we can now define new hypercubic quark fields $q(h)$ and $\bar{q}(h)$ as

$$q(h)_{ab} \equiv \frac{1}{8}\sum_s \Gamma^{(s)}_{ab}\chi(2h + s), \quad \bar{q}(h)_{ab} \equiv \frac{1}{8}\sum_s \bar{\chi}(2h + s)\Gamma^{(s)*}_{ba}, \tag{2.59}$$

where a and b are indices for new spaces, which we later identify as the new Dirac and taste space. The inverse relation reads

$$\chi(2h + s) = 2\mathrm{tr}\left[\Gamma^{(s)\dagger}q(h)\right], \quad \bar{\chi}(2h + s) = 2\mathrm{tr}\left[\bar{q}(h)\Gamma^{(s)}\right]. \tag{2.60}$$

The mass term of the staggered action Eq. 2.47 is straight forward

$$\begin{aligned} a^4 \sum_n \bar{\chi}(n)\chi(n) =& a^4 \sum_h \sum_s \bar{\chi}(2h+s)\chi(2h+s) \\ =& 4a^4 \sum_h \sum_s \bar{q}(h)_{ba} \Gamma^{(s)}_{ab} \Gamma^{(s)\dagger}_{b'a'} q(h)_{a'b'} \\ =& (2a)^4 \sum_h \mathrm{tr}[\bar{q}(h)q(h)]. \end{aligned} \tag{2.61}$$

The kinetic term is a bit more involved. The result is

$$S_{stagg,kin} = (2a)^4 \sum_h \sum_\mu \mathrm{tr}[\bar{q}(h)\gamma_\mu \nabla_\mu q(h)] - a\ \mathrm{tr}[\bar{q}(h)\gamma_5 \Delta_\mu q(h)\gamma_\mu\gamma_5], \tag{2.62}$$

with $\nabla_\mu f(h) = \frac{f(h+\hat{\mu})-f(h-\hat{\mu})}{4a}$ and $\Delta_\mu f(h) = \frac{f(h+\hat{\mu})-2f(h)+f(h-\hat{\mu})}{(2a)^2}$. This result will now be verified by inserting everything back in. It follows

$$\begin{aligned} S_{stagg,kin} =& (2a)^4 \sum_h \sum_\mu \mathrm{tr}\left[\bar{q}(h)\gamma_\mu \frac{q(h+\hat{\mu}) - q(h-\hat{\mu})}{4a}\right] \\ & - \mathrm{tr}\left[\bar{q}(h)\gamma_5 \frac{q(h+\hat{\mu}) - 2q(h) + q(h-\hat{\mu})}{4a}\gamma_\mu\gamma_5\right] \\ =& 4a^3 \sum_h \sum_\mu \mathrm{tr}[\bar{q}(h)\gamma_\mu (q(h+\hat{\mu}) - q(h-\hat{\mu}))] \\ & - \mathrm{tr}[\bar{q}(h)\gamma_5 (q(h+\hat{\mu}) - 2q(h) + q(h-\hat{\mu}))\gamma_\mu\gamma_5] \\ =& 4a^3 \sum_h \sum_\mu \sum_{ss'} \mathrm{tr}\left[\frac{1}{8}\bar{\chi}(2h+s)\Gamma^{(s)\dagger}\gamma_\mu \left(\frac{1}{8}\Gamma^{(s')}\chi(2(h+\hat{\mu})+s')\right.\right. \\ & \left.\left. - \frac{1}{8}\Gamma^{(s')}\chi(2(h-\hat{\mu})+s')\right)\right] \\ & - \mathrm{tr}\left[\frac{1}{8}\bar{\chi}(2h+s)\Gamma^{(s)\dagger}\gamma_5 \left(\frac{1}{8}\Gamma^{(s')}\chi(2(h+\hat{\mu})+s') - \frac{2}{8}\Gamma^{(s')}\chi(2h+s')\right.\right. \\ & \left.\left. + \frac{1}{8}\Gamma^{(s')}\chi(2(h-\hat{\mu})+s')\right)\gamma_\mu\gamma_5\right]. \end{aligned} \tag{2.63}$$

Note that χ and $\bar{\chi}$ are only numbers in the trace. By using the relations

$$\mathrm{tr}\left[\Gamma^{(s)\dagger}\gamma_5\Gamma^{(s')}\gamma_\mu\gamma_5\right] = (-1)^{s_\mu}\mathrm{tr}[\Gamma^{(s)\dagger}\gamma_\mu\Gamma^{(s')}] \tag{2.64}$$

and

$$\mathrm{tr}[\Gamma^{(s)\dagger}\gamma_\mu\Gamma^{(s')}] = 4\eta_\mu(s)\delta_{s,s'\pm\mu} \tag{2.65}$$

one gets

$$\begin{aligned}S_{stagg,kin} =&4a^3\sum_h\sum_s\sum_\mu\frac{1}{16}\bar{\chi}(2h+s)[\eta_\mu(s)(\delta_{s_\mu 1}(\chi(2(h+\hat{\mu})+s-\hat{\mu})\\&-\chi(2(h-\hat{\mu})+s-\hat{\mu}))+\delta_{s_\mu 0}(\chi(2(h+\hat{\mu})+s+\hat{\mu})\\&-\chi(2(h-\hat{\mu})+s+\hat{\mu})))-\eta_{\mu+1}(s)(\delta_{s_\mu 1}(\chi(2(h+\hat{\mu})+s-\hat{\mu})\\&-2\chi(2h+s-\hat{\mu})+\chi(2(h-\hat{\mu})+s-\hat{\mu}))+\delta_{s_\mu 0}(\chi(2(h+\hat{\mu})+s+\hat{\mu})\\&-2\chi(2h+s+\hat{\mu})+\chi(2(h-\hat{\mu})+s+\hat{\mu})))].\end{aligned} \tag{2.66}$$

Let us see what happens to the staggered phase factor for different values of s_μ: For $s_\mu = 0$ it follows $\eta_{\mu+1}(s) = \eta_\mu(s)$, while for $s_\mu = 1$ it follows $\eta_{\mu+1}(s) = -\eta_\mu(s)$. With that in mind it follows

$$\begin{aligned}S_{stagg,kin} =&4a^3\sum_h\sum_s\sum_\mu\frac{1}{16}\bar{\chi}(2h+s)[\eta_\mu(s)(\delta_{s_\mu 1}(\chi(2(h+\hat{\mu})+s-\hat{\mu})\\&-\chi(2(h-\hat{\mu})+s-\hat{\mu}))+\delta_{s_\mu 0}(\chi(2(h+\hat{\mu})+s+\hat{\mu})\\&-\chi(2(h-\hat{\mu})+s+\hat{\mu})))-\eta_\mu(s)(\delta_{s_\mu 1}(-\chi(2(h+\hat{\mu})+s-\hat{\mu})\\&+2\chi(2h+s-\hat{\mu})-\chi(2(h-\hat{\mu})+s-\hat{\mu}))+\delta_{s_\mu 0}(\chi(2(h+\hat{\mu})+s+\hat{\mu})\\&-2\chi(2h+s+\hat{\mu})+\chi(2(h-\hat{\mu})+s+\hat{\mu})))]\\=&4a^3\sum_h\sum_s\sum_\mu\frac{1}{16}\bar{\chi}(2h+s)\eta_\mu(s)[\delta_{s_\mu 1}(2\chi(2(h+\hat{\mu})+s-\hat{\mu})\\&-2\chi(2h+s-\hat{\mu}))+\delta_{s_\mu 0}(2\chi(2h+s+\hat{\mu})-2\chi(2(h-\hat{\mu})+s+\hat{\mu}))]\\=&8a^3\sum_h\sum_s\sum_\mu\frac{1}{16}\bar{\chi}(2h+s)\eta_\mu(s)[\chi(2h+s+\mu)-\chi(2h+s-\mu)].\end{aligned} \tag{2.67}$$

Therefore the kinetic part of the staggered action reads

$$\begin{aligned}S_{stagg,kin} =&a^4\sum_h\sum_s\sum_\mu\bar{\chi}(2h+s)\eta_\mu(s)\frac{\chi(2h+s+\hat{\mu})-\chi(2h+s-\hat{\mu})}{2a}\\=&(2a)^4\sum_h\sum_\mu\mathrm{tr}[\bar{q}(h)\gamma_\mu\nabla_\mu q(h)]-a\ \mathrm{tr}[\bar{q}(h)\gamma_5\Delta_\mu q(h)\gamma_\mu\gamma_5].\end{aligned} \tag{2.68}$$

We now want to identify the quark fields $q(h)_{ab}$ with new fields ψ

$$\psi^{(t)}(h)_\beta \equiv q(h)_{\beta t}, \qquad \bar{\psi}^{(t)}(h)_\beta \equiv \bar{q}(h)_{t\beta}, \tag{2.69}$$

where β is an index of the new Dirac space and t is an index of the taste

space. In total the free staggered action for these new fields is

$$S_F[\psi,\bar{\psi}] =(2a)^4 \sum_h \Bigg(\sum_{t=1}^{4} \Bigg(m\bar{\psi}^{(t)}(h)\psi^{(t)}(h) + \sum_{\mu=1}^{4} \bar{\psi}^{(t)}(h)\gamma_\mu \nabla_\mu \psi^{(t)}(h) \Bigg) - a \sum_{t,t'=1}^{4} \sum_{\mu=1}^{4} \bar{\psi}^{(t)}(h)\gamma_5(\tau_5\tau_\mu)_{tt'}\Delta_\mu \psi^{(t')}(h) \Bigg), \tag{2.70}$$

where $\tau_\nu = \gamma_\nu^T$. In Eq. 2.70 three terms can be identified. First the usual mass term, second the usual kinetic term and a third term with $(\tau_5\tau_\mu)_{tt'}$, which mixes different tastes and therefore breaks taste-symmetry. But this third term vanishes in the continuum limit $a \to 0$ and therefore taste-symmetry gets restored. Because nothing was omitted or added regarding the staggered action, it is the same action and therefore the same general quark fields. It is now visible that by creating these hypercubic quark fields $\bar{q}$ and q the new Dirac and taste space are distributed over the lattice. This action however has large cut-off effects. To reduce the cut-off effects we use an improved version of the staggered action of Eq. 2.70. This action reduces the cut-off effects of the taste-breaking term by smearing of the gauge links to remove tree-level taste-changing and reduction of one-loop taste-changing. Therefore the overall cut-off effects are reduced to $\mathcal{O}(a^2)$. This action is called the Highly-Improved Staggered Quarks (HISQ) action [27]. Details on the HISQ action and the smearing process are nicely explained in Ref. [28].

In the next section 2.7 we will explain the construction of hadronic correlators for staggered fermions.

2.7 Hadronic correlators for staggered fermions

With the knowledge from section 2.6 we can create hadronic interpolators and then hadronic correlators. As quark fields we use the hypercubic quark fields. As defining symmetries for the hadronic interpolators a Dirac and a taste matrix is necessary [29]. In this thesis mesonic correlators are investigated, therefore a detailed look into these kinds of interpolators and the construction of their correlators is now given.

As a reminder, a local continuum meson interpolator is given by

$$O_M(x) = \bar{\psi}_\alpha^{(f)}(x)\Gamma_{\alpha\alpha'}\psi_{\alpha'}^{(f')}(x), \tag{2.71}$$

where Γ is the generating operator for the quantum numbers of the meson state and α is the Dirac index. Now let us look at the changes for the bilinear

in the staggered case [29]. For our interpolator with hypercubic fields $q(h)_{\beta t}$ in the free case

$$\begin{aligned} O_M(h) =& \bar{q}^{(f)}(h)(\Gamma^D \otimes \Gamma^t) q^{(f')}(h) \\ =& \frac{1}{64} \sum_{ss'} \bar{\chi}^{(f)}(2h+s) \Gamma^{(s)\dagger}_{t\beta} \Gamma^D_{\beta\beta'} \Gamma^{(s')}_{\beta' t'} \chi^{(f')}(2h+s') \Gamma^t_{tt'} \\ =& \frac{1}{64} \sum_{ss'} \bar{\chi}^{(f)}(2h+s) \Gamma^{(s)\dagger}_{t\beta} \Gamma^D_{\beta\beta'} \Gamma^{(s')}_{\beta' t'} \chi^{(f')}(2h+s') \Gamma^{tT}_{t't} \\ =& \frac{1}{64} \sum_{ss'} \bar{\chi}^{(f)}(2h+s) \chi^{(f')}(2h+s') \mathrm{tr}\Big[\Gamma^{(s)\dagger} \Gamma^D \Gamma^{(s')} \Gamma^{tT}\Big], \end{aligned} \tag{2.72}$$

where Γ^D and Γ^t are gamma matrices acting only on the new Dirac space or on the taste space respectively and T refers to the transpose. For local meson interpolators one has $\Gamma \equiv \Gamma^D \equiv \Gamma^{t*}$. Note that the two Dirac spaces indexed by α in Eq. 2.71 and β in Eq. 2.72 are not the same. For local meson interpolators in the staggered case one gets $s = s'$ and a phase factor to take care of. Since for local meson interpolators only $\bar{\chi}$ and χ fields on the same lattice sites are connected, this definition is also true for the interacting case. Let us take for example $\Gamma = \gamma_5$

$$\begin{aligned} \mathrm{tr}\Big[\Gamma^{(s)\dagger} \gamma_5 \Gamma^{(s')} \gamma_5^\dagger\Big] =& \mathrm{tr}\Big[\gamma_4^{\dagger(s_4)} \gamma_3^{\dagger(s_3)} \gamma_2^{\dagger(s_2)} \gamma_1^{\dagger(s_1)} \gamma_5 \gamma_1^{(s'_1)} \gamma_2^{(s'_2)} \gamma_3^{(s'_3)} \gamma_4^{(s'_4)} \gamma_5^\dagger\Big] \\ =& \mathrm{tr}\Big[\gamma_4^{\dagger(s_4)} \gamma_3^{\dagger(s_3)} \gamma_2^{\dagger(s_2)} \gamma_1^{\dagger(s_1)} \underbrace{\gamma_5 \gamma_5^\dagger}_{I_4} (-1)^{s'_1+s'_2+s'_3+s'_4} \gamma_1^{(s'_1)} \gamma_2^{(s'_2)} \gamma_3^{(s'_3)} \gamma_4^{(s'_4)}\Big] \\ =& (-1)^{s'_1+s'_2+s'_3+s'_4} \mathrm{tr}\Big[\gamma_4^{\dagger(s_4)} \gamma_3^{\dagger(s_3)} \gamma_2^{\dagger(s_2)} \gamma_1^{\dagger(s_1)} \gamma_1^{(s'_1)} \gamma_2^{(s'_2)} \gamma_3^{(s'_3)} \gamma_4^{(s'_4)}\Big] \\ =& (-1)^{s'_1+s'_2+s'_3+s'_4} \mathrm{tr}\Big[\Gamma^{(s)\dagger} \Gamma^{(s')}\Big] = 4\delta_{ss'} (-1)^{s'_1+s'_2+s'_3+s'_4}. \end{aligned} \tag{2.73}$$

Therefore the local meson γ_5 interpolator reads

$$\begin{aligned} O_{M,\gamma_5}(h) =& \frac{1}{64} \sum_{ss'} \bar{\chi}^{(f)}(2h+s) \chi^{(f')}(2h+s') 4\delta_{ss'} (-1)^{s'_1+s'_2+s'_3+s'_4} \\ =& \frac{1}{16} \sum_{s} (-1)^{s_1+s_2+s_3+s_4} \bar{\chi}^{(f)}(2h+s) \chi^{(f')}(2h+s). \end{aligned} \tag{2.74}$$

Since the main structure in the staggered action from Eq. 2.70 is the same as for e.g. the naive action, the same choice for Γ_D in staggered and Γ in Eq. 2.71 creates meson states with the same quantum numbers. In this thesis we only use local meson interpolators and we will focus on these now by setting $\Gamma \equiv \Gamma^D \equiv \Gamma^{t*}$. For the interpolator in Eq. 2.74 all momenta are still present. To get just the masses a momentum projection to momentum zero has to be done. This can be done by a partial discrete Fourier transformation to

momentum space and setting the momentum directly, in this case to zero. It follows

$$\tilde{O}_M(0,h_4) = C_0 \sum_{\vec{h}} O_M(\vec{h},h_4), \tag{2.75}$$

where C_0 is a normalization constant. We will come back to this later.

There is another issue in Eq. 2.74. Our meson interpolator has hypercubic coordinate h, i.e. not a specific lattice site n like in the continuum case. Because our χ fields sit on lattice sites n and contribute differently this would lead to an indefinite distance between source and sink. A solution is to add or subtract another term to cancel contributions of specific χ and $\bar{\chi}$ fields

$$O_M(h) = \bar{q}^{(f)}(h)(\Gamma\otimes\Gamma^*)q^{(f')}(h) \pm \bar{q}^{(f)}(h)((\gamma_4\gamma_5\Gamma)\otimes(\gamma_4^*\gamma_5^*\Gamma^*))q^{(f')}(h), \tag{2.76}$$

while the phase between the first and second term will be $\phi(s) = (-1)^{s_4}$. What does that do? If there is a plus between these two meson states then the contributions with $s_4 = 1$ cancel, if there is a minus the contributions with $s_4 = 0$ cancel. Therefore only contributions of one time slice in these hypercubic fields survive. For our $\Gamma = \gamma_5$ example using the plus-term of Eq. 2.76 we get

$$\begin{aligned}
O_{M2,+}(h) =& \frac{1}{16}\sum_s \bar{\chi}^{(f)}(2h+s)(-1)^{s_1+s_2+s_3+s_4}\chi^{(f')}(2h+s) \\
&+ \frac{1}{16}\sum_{s'} \bar{\chi}^{(f)}(2h+s')(-1)^{s_1'+s_2'+s_3'}\chi^{(f')}(2h+s') \\
=& \frac{1}{16}\sum_s (-1)^{s_1+s_2+s_3}\Big((-1)^{s_4}\bar{\chi}^{(f)}(2h+s)\chi^{(f')}(2h+s) \\
&+ \bar{\chi}^{(f)}(2h+s)\chi^{(f')}(2h+s)\Big) \\
=& \frac{1}{8}\sum_{\substack{s \\ s_4=0}} (-1)^{s_1+s_2+s_3}\bar{\chi}^{(f)}(2h+s)\chi^{(f')}(2h+s).
\end{aligned} \tag{2.77}$$

Similarly for $\Gamma = \gamma_5$ with the minus-term leads to

$$\begin{aligned} O_{M2,-}(h) =& \frac{1}{16}\sum_{s} \bar{\chi}^{(f)}(2h+s)(-1)^{s_1+s_2+s_3+s_4}\chi^{(f')}(2h+s) \\ & - \frac{1}{16}\sum_{s'} \bar{\chi}^{(f)}(2h+s')(-1)^{s'_1+s'_2+s'_3}\chi^{(f')}(2h+s') \\ =& \frac{1}{16}\sum_{s}(-1)^{s_1+s_2+s_3}\Big((-1)^{s_4}\bar{\chi}^{(f)}(2h+s)\chi^{(f')}(2h+s) \\ & - \bar{\chi}^{(f)}(2h+s)\chi^{(f')}(2h+s)\Big) \\ =& -\frac{1}{8}\sum_{\substack{s \\ s_4=1}}(-1)^{s_1+s_2+s_3}\bar{\chi}^{(f)}(2h+s)\chi^{(f')}(2h+s). \end{aligned} \tag{2.78}$$

Combining both Eq. 2.77 and Eq. 2.78 we get

$$O_{M2}(h,s_4) = \frac{1}{8}\sum_{s_1,s_2,s_3}(-1)^{s_1+s_2+s_3+s_4}\bar{\chi}^{(f)}(2h+s)\chi^{(f')}(2h+s), \tag{2.79}$$

where s_4 is an explicit variable of the interpolator. Therefore the interpolator of Eq. 2.79 has a specific distance in the 4-direction, which is the separation direction. After understanding and constructing the interpolators, next the hadronic correlators have to be constructed. Again at this point only mesonic staggered correlators will be discussed.

So far we constructed only the annihilation interpolator O_M, i.e. a sink. For a correlator we also need a corresponding creation interpolator $\bar{O}_M$, i.e. a source. Since all Dirac structure comes from terms like Eq. 2.57 the staggered fields χ and $\bar{\chi}$ are conjugate transpose to each other, i.e. $\bar{\chi} = \chi^\dagger$. Note that the staggered fields are still Grassmann-valued fields. Therefore a creation interpolator reads for the aforementioned example of a local meson interpolator for the $\Gamma = \gamma_5$

$$\begin{aligned} \bar{O}_{M2}(h,s_4) =& \left(\frac{1}{8}\sum_{s_1,s_2,s_3}(-1)^{s_1+s_2+s_3+s_4}\bar{\chi}^{(f)}(2h+s)\chi^{(f')}(2h+s)\right)^\dagger \\ =& -\frac{1}{8}\sum_{s_1,s_2,s_3}(-1)^{s_1+s_2+s_3+s_4}\bar{\chi}^{(f')}(2h+s)\chi^{(f)}(2h+s). \end{aligned} \tag{2.80}$$

The minus sign results from the exchange of Grassmann-valued fields. With that the fermionic part of the correlator can be constructed. The next step

is the contraction of the fields. It follows for our example with $f \neq f'$

$$\begin{aligned} C_{M2}(h,s_4)_F =& \langle O_{M,\gamma_5}(h,s_4)\bar{O}_{M,\gamma_5}(0,0)\rangle_F \\ =& -\frac{1}{64}\frac{1}{Z_F}\int \mathcal{D}[\chi,\bar{\chi}] \sum_{\substack{s'',s' \\ s''_4=s_4,s'_4=0}} (-1)^{s''_1+s''_2+s''_3+s''_4+s'_1+s'_2+s'_3+s'_4} \\ & \times \bar{\chi}^{(f)}(2h+s'')\chi^{(f')}(2h+s'')\bar{\chi}^{(f')}(s')\chi^{(f)}(s')\exp(-S_F[U,\chi,\bar{\chi}]) \\ =& \frac{1}{64} \sum_{\substack{s'',s' \\ s''_4=s_4,s'_4=0}} (-1)^{s''_1+s''_2+s''_3+s''_4+s'_1+s'_2+s'_3+s'_4} \\ & \times \mathrm{tr}[M^{-1}_{f'}(2h+s''|s')M^{-1}_{f}(s'|2h+s'')], \end{aligned} \tag{2.81}$$

where $M_f(n|m)$ refers to Dirac operators with flavor f connecting space-time point n to m and $Z_F = \det(M_f)\det(M_{f'})$. Again a minus sign was introduced via exchange of Grassmann-valued fields. The contractions of $\bar{\chi}$ and χ are so-called quark propagators leading to traces over inverse Dirac operators. Those could be solved with the conjugate gradient method mentioned in subsection 2.4.2. The double summation over all corners of the hypercube in Eq. 2.81 gives rise to multiple calculations of inverse Dirac operators. This would have high computational cost. It can be reduced by a similar strategy as in Eq. 2.76. Here we add all the remaining 14 states only to the source operator $\bar{O}_{M,\gamma_5}(0,0)$ to set $s'_1 = s'_2 = s'_3 = 0$. The sink then automatically selects the correct states due to quantum number conservation. Still using the sink from Eq. 2.79 we get

$$C_{M2}(h,s_4)_F = C_1 \sum_{\substack{s'' \\ s''_4=s_4}} (-1)^{s''_1+s''_2+s''_3+s''_4} \mathrm{tr}[M^{-1}_{f'}(2h+s''|0)M^{-1}_{f}(0|2h+s'')], \tag{2.82}$$

where a projection to momentum zero by a modification according to Eq. 2.75 in only one of the interpolators leads to

$$\begin{aligned} \tilde{C}_{M2}(h_4,s_4)_F =& C_2 \sum_{\vec{n}} (-1)^{n_1+n_2+n_3+n_4} \mathrm{tr}[M^{-1}_{f'}(n|0)M^{-1}_{f}(0|n)] \\ =& C_2 \sum_{\vec{n}} \mathrm{tr}[M^{-1}_{f'}(n|0)M^{-1\dagger}_{f}(n|0)] \equiv \tilde{C}_{M2}(n_4)_F, \end{aligned} \tag{2.83}$$

where $n = 2h + s$ for all four dimensions and $\vec{n}$ is only for the three spatial dimensions. Only one interpolator has to be modified since states with different momenta are othogonal to each other. In the second step of Eq. 2.83 $M^{-1\dagger}_f(n|0) = (-1)^{n_1+n_2+n_3+n_4}M^{-1}_f(0|n)$ was used to simplify it even more.

In our example the phase factor is $\phi(\mathbf{x}) = 1$. In general the final correlators are

$$\begin{aligned}\tilde{C}_M(h_4, s_4) =& \langle O_M(h, s_4)\bar{O}_M(0,0)\rangle \\ =& \frac{1}{Z}\int \mathcal{D}[U]\det(M_f)\det(M_{f'})\exp(-S_G[U])\tilde{C}_M(h_4, s_4)_F,\end{aligned} \tag{2.84}$$

with

$$Z = \int \mathcal{D}[U]\det(M_f)\det(M_{f'}), \tag{2.85}$$

where U are gauge field configurations and S_G is the gluonic action. To calculate the observable itself we need to invert the Dirac matrix M. To calculate the complete correlator we use the methods, which we presented in section 2.4.

Starting from the other end we know from Eq. 2.20 that a correlator built from interpolators in the form of Eq. 2.72 will have an exponential decay according to their energy levels. Since on a lattice we have boundary conditions we also experience an exponential rise mirroring this decay. That leads to a sum of an exponential decay and rise, which can be brought together to

$$\begin{aligned}\langle O_2(\tau)O_1(0)\rangle =& \sum_n \langle\tilde{0}|\,\hat{O}_2\,|n\rangle\,\langle n|\,\hat{O}_1\,|\tilde{0}\rangle\,(\exp(-\tau E_n) + \exp((\tau - aN_\tau)E_n)) \\ =& \sum_n \langle\tilde{0}|\,\hat{O}_2\,|n\rangle\,\langle n|\,\hat{O}_1\,|\tilde{0}\rangle \exp\left(-a\frac{N_\tau}{2}E_n\right) 2\cosh\left(\left(\tau - a\frac{N_\tau}{2}\right)E_n\right) \\ =& \sum_n A_n \cosh\left(\left(\tau - a\frac{N_\tau}{2}\right)E_n\right),\end{aligned} \tag{2.86}$$

where $|\tilde{0}\rangle$ is the vacuum state of the fixed temperature system, i.e. an in-medium state. Since an interpolator of the form of Eq. 2.76 adds or subtracts a second state depending on the separation distance n_τ, in our case the selecting sink, the correlator becomes

$$\begin{aligned}\langle O_2(n_\tau)O_1(0)\rangle =& \sum_i A_i \cosh\left(\left(n_\tau - \frac{N_\tau}{2}\right)aE_{i,1}\right) \\ & - (-1)^{n_\tau}\sum_j B_j \cosh\left(\left(n_\tau - \frac{N_\tau}{2}\right)aE_{j,2}\right),\end{aligned} \tag{2.87}$$

where we now switched to pure lattice notation. After projection to momentum zero the energies E_i in Eq. 2.87 will only contain masses. For an explanation of the relative minus sign between the two states see section 2.8.

The usual procedure now is to fit the function from Eq. 2.87 with parameters A_i, B_j, $E_{i,1}$ and $E_{j,2}$ onto the calculated correlator at different separation distances n_τ. For our calculation however the maximum distance in time direction N_τ is rather short due to the link to the inverse temperature $1/T$. That leads to obvious technical problems in the analysis of high temperatures. To circumvent that we use spatial instead of temporal correlators. These spatial correlators are also called screening correlators. From a technical standpoint getting screening correlators from temporal correlators is very simple. We just have to interchange all variables related to the temporal direction with the variables related to the spatial direction. In our case we interchange $\gamma_4 \leftrightarrow \gamma_3$, $n_\tau \leftrightarrow n_z$ and $N_\tau \leftrightarrow N_z$. For simplicity we are using n or n_σ for n_z and N_s or N_σ for N_z to indicate that they are spatial correlators. The limits, which have to be taken to reduce the cut-off effects, however stay the same, i.e. $N_s \to \infty$ for thermodynamic limit and $N_\tau \to \infty$ for continuum limit.

From a physical standpoint however we change the content of our created states. Instead of pole masses we get screening masses, hence the name for the correlators. For zero temperature these two masses are identical because of Lorentz invariance. For non-zero temperature small modifications happen, which are temperature dependent resulting from the breaking of the Lorentz invariance at finite temperature [30]. More on that in subsection 2.7.1. However these modifications are the same factors for degenerate correlators like the correlators of scalar and pseudoscalar particles if the $U_A(1)$ symmetry is restored, and the correlators of vector and axialvector particles if $SU_A(2)$ symmetry is restored. In this work we extract the ground state masses of those particles and we are only interested in the difference between particle masses, which are connected via their respective symmetry, which makes this temperature dependent modification irrelevant. The main focus is the anomaly of $U_A(1)$, which can be investigated by the degeneracy of scalar and pseudoscalar particle. More on that in section 2.10. The screening mass extraction process will be explained in more detail in section 3.1.

Through the addition or subtraction of another term, see Eq. 2.76, a second particle with different quantum numbers was introduced to the staggered correlator. Note that depending on the mesons in each of these correlators, also known as channels, only the phase factor changes. For all our calculations we used local screening meson staggered correlators. In Tab. 2.1 the phase factors $\phi(\mathbf{x})$ for all these correlators are listed.

In section 2.8 we will show the connection between different particles of our screening mass correlators, i.e. chiral symmetries, and why their susceptibilities describe only one state instead of two. Since we are using screening masses we give a short explanation of the more subtle differences to pole

masses and why they are sufficient for our study in the next subsection 2.7.1.

	$\phi(\mathbf{x})$	Γ_D		J^{PC}		states	
		NO	O	NO	O	NO	O
$M1$	$(-1)^{x+y+\tau}$	$\gamma_3\gamma_5$	$\mathbb{1}$	0^{-+}	0^{++}	π_2	a_0
$M2$	1	γ_5	γ_3	0^{-+}	0^{+-}	π	–
$M3$	$(-1)^{y+\tau}$	$\gamma_1\gamma_3$	$\gamma_1\gamma_5$	1^{--}	1^{++}	$\rho_2^{\mathcal{T}}$	$a_1^{\mathcal{T}}$
$M4$	$(-1)^{x+\tau}$	$\gamma_2\gamma_3$	$\gamma_2\gamma_5$	1^{--}	1^{++}	$\rho_2^{\mathcal{T}}$	$a_1^{\mathcal{T}}$
$M5$	$(-1)^{x+y}$	$\gamma_4\gamma_3$	$\gamma_4\gamma_5$	1^{--}	1^{++}	$\rho_2^{\mathcal{L}}$	$a_1^{\mathcal{L}}$
$M6$	$(-1)^{x}$	γ_1	$\gamma_2\gamma_4$	1^{--}	1^{+-}	$\rho_1^{\mathcal{T}}$	$b_1^{\mathcal{T}}$
$M7$	$(-1)^{y}$	γ_2	$\gamma_1\gamma_4$	1^{--}	1^{+-}	$\rho_1^{\mathcal{T}}$	$b_1^{\mathcal{T}}$
$M8$	$(-1)^{\tau}$	γ_4	$\gamma_1\gamma_2$	1^{--}	1^{+-}	$\rho_1^{\mathcal{L}}$	$b_1^{\mathcal{L}}$

Table 2.1: The list of all local screening meson staggered operators. States associated with the non-oscillating and oscillating part of the screening correlators are designated by the identifiers NO and O, respectively. Particle assignments of the corresponding states are given only for the $\bar{u}d$ flavor combination. The superscripts $\mathcal{T}$ and $\mathcal{L}$ stand for transverse and longitudinal, respectively. The operators listed here are taken from Ref. [12] and are identical to Ref. [31].

2.7.1 What are screening masses?

There is a significant difference between pole masses and screening masses. Pole masses are the true masses of a particle in the usual sense of an exponential decay of a correlator along Euclidean time. Screening masses on the other hand are measured along the spatial direction. The temporal and the spatial directions are equal at $T = 0$. However at finite T the Lorentz invariance gets broken and therefore both masses describe different things. While the pole masses still describe the mass of a particle in the usual sense, screening masses describe something a bit more subtle. The interactions in a thermal medium most likely alter the dispersion relation to [32]

$$\omega^2(\vec{p}, T) = M_H^2 + \vec{p}^2 + \Pi(\vec{p}, T), \tag{2.88}$$

where $\Pi(\vec{p}, T)$ is the temperature dependent vacuum polarization. In the simplest case [30] we can absorb this vacuum polarization into a temperature dependent mass and a coefficient $A(T)$, which might also be temperature dependent

$$\omega^2(\vec{p}, T) \simeq M_H^2(T) + A^2(T)\vec{p}^2. \tag{2.89}$$

In this case, at zero momentum the decay of the spatial correlator is determined by the screening mass $M_H^{sc}(T) = \frac{M_H(T)}{A(T)}$ while the decay of the

temporal correlator is determined by the pole mass $M_H(T)$. Therefore the pole and screening mass differ if $A(T) \neq 1$.

Because at some non-zero temperature it is $A(T) \neq 1$ we can not necessarily identify the screening and the pole masses at any temperature, e.g. T_c. The difference of the pole masses of π and a_0 however is a measure of $U_A(1)$ symmetry breaking, since $U_A(1)$ symmetry should be effectively restored if both masses become degenerate. We can use the difference of screening masses of π and a_0 to the same extent, because the mass difference should only be divided by $A(T)$, which comes from the vacuum polarization $\Pi(\vec{p}, T)$ in the case of zero momentum. That means that if $U_A(1)$ symmetry gets effectively restored, the screening masses of π and a_0 should be degenerate as well.

Another way to look at the spatial correlation functions at finite temperature [30] is that the finite temporal extents of the Euclidean lattice act on spatial quark and anti-quark propagators like a finite volume effect, which influences the long-distance behavior of the spatial correlation functions [12]. Screening masses in QCD thus act similar to the Debye screening in Quantum Electrodynamics (QED) created by the plasmon in an electrodynamic plasma [33]. This screening therefore changes the interaction between particles to a shorter ranged effective interaction.

In the next section 2.8 we go into more details about the chiral symmetries and the susceptibilities for staggered fermions.

2.8 Chiral symmetries and susceptibilities for staggered fermions

In this section we explain the chiral symmetries for staggered fermions and then address the relative minus sign between the two states of Eq. 2.87 with the help of this deeper understanding. Next we want to show that even though the correlator has two states instead of only one, we can get susceptibilities for only one state by summing over these correlators.

As already mentioned in section 2.6 the projection from fields $\bar{X}$ and X to $\bar{\chi}$ and χ removes the original Dirac structure and changes some non-trivial aspects like chiral rotations. After this projection the chiral rotations form a smaller group. As shown in section 2.7 the quark fields, which describe the theory with staggered fermions, are the hypercubic quark fields $\bar{q}$ and q. As also seen in section 2.7 particle states are described by a tensor product of the new Dirac and taste space. Therefore the chiral rotations also consist of these tensor products. The staggered action from Eq. 2.70 with hypercubic fields is invariant under $U_\epsilon(1)$ rotations [34, 35]

$$q' = \exp(i\alpha(\gamma_5 \otimes \gamma_5^*))q, \qquad \bar{q}' = \bar{q}\exp(i\alpha(\gamma_5 \otimes \gamma_5^*)), \tag{2.90}$$

where the first part of the tensor product is the Dirac and the second part is the taste space. Eq. 2.90 describes the remnant chiral symmetry. Let us apply that to the pseudoscalar bilinear to see what happens:

$$\begin{aligned} O_M(h) =& \bar{q}(h)_{t\beta}(\gamma_{5,\beta\beta'}\gamma^*_{5,tt'})q(h)_{\beta' t'} \\ =& \bar{q}(h)_{t''\beta''}\exp(i\alpha\gamma_{5,\beta''\beta}\gamma^*_{5,t''t})\gamma_{5,\beta\beta'}\gamma^*_{5,tt'} \\ & \times \exp(i\alpha\gamma_{5,\beta'\beta^{(3)}}\gamma^*_{5,t't^{(3)}})q(h)_{\beta^{(3)}t^{(3)}} \\ =& \frac{1}{64}\sum_{s,s'}\bar{\chi}(2h+s)\chi(2h+s')(\gamma_4^{s_4}\gamma_3^{s_3}\gamma_2^{s_2}\gamma_1^{s_1})_{t''\beta''} \\ & \times \exp(i\alpha\gamma_{5,\beta''\beta}\gamma^*_{5,t''t})\gamma_{5,\beta\beta'}\gamma^*_{5,tt'}\exp(i\alpha\gamma_{5,\beta'\beta^{(3)}}\gamma^*_{5,t't^{(3)}}) \\ & \times (\gamma_1^{s_1'}\gamma_2^{s_2'}\gamma_3^{s_3'}\gamma_4^{s_4'})_{\beta^{(3)}t^{(3)}}. \end{aligned} \tag{2.91}$$

Next we use a similar strategy as in Eq. 2.54 and sort everything for traces again. It follows

$$\begin{aligned} O_M(h) =& \frac{1}{64}\sum_{s,s'}\bar{\chi}(2h+s)\chi(2h+s') \\ & \times \left(4\eta_5(s)\delta_{ss'}(\cos^2(\alpha)-\sin^2(\alpha)) + 2i\eta_5^2(s)\sin(\alpha)\cos(\alpha)\mathrm{tr}[\gamma_5\Gamma^{(s)\dagger}\gamma_5\gamma_5\Gamma^{(s')}\gamma_5]\right) \\ =& \frac{1}{64}\sum_{s,s'}\bar{\chi}(2h+s)\chi(2h+s')\left(4\eta_5(s)\delta_{ss'}(\cos^2(\alpha)-\sin^2(\alpha)) + 2i\sin(\alpha)\cos(\alpha)4\delta_{ss'}\right) \\ =& \frac{1}{16}\sum_{s}\bar{\chi}(2h+s)\chi(2h+s)\left(\eta_5(s)(\cos^2(\alpha)-\sin^2(\alpha)) + 2i\sin(\alpha)\cos(\alpha)\right) \\ =& \frac{1}{16}\sum_{s}\bar{\chi}(2h+s)\chi(2h+s)\left(\eta_5(s)\cos(2\alpha) + i\sin(2\alpha)\right). \end{aligned} \tag{2.92}$$

If we rotate with an angle $\alpha = \frac{\pi}{4}$ we get

$$O_M(h) = \frac{1}{16}\sum_{s}\bar{\chi}(2h+s)\chi(2h+s)i. \tag{2.93}$$

By rotating from the pseudoscalar to this state we therefore get a factor of $i\eta_5(n)$ from the sink and $i\eta_5(0) = i$ from the source. A relative η_5 between the unrotated and rotated interpolator means that they are connected like the continuum $U_A(1)$ rotation where a relative γ_5 is between the two interpolators, which means that this other interpolator consists therefore of a scalar state. From source and sink we get a factor of $-\eta_5(n)$ for the correlator. The total relative minus sign between these correlators leads to the relative minus sign if we look at the physical content of the correlator. That explains the relative minus sign in 2.87 for our staggered correlators. The calculation for vector and axialvector is analogous. Note that the rotation of Eq. 2.90 is not

the anomalous $U_A(1)$ rotation from continuum physics. The $U(1)$ rotation, which has the anomaly, is

$$q' = \exp(i\alpha(\gamma_5 \otimes \mathbb{1}))q, \qquad \bar{q}' = \bar{q}\exp(i\alpha(\gamma_5 \otimes \mathbb{1})), \tag{2.94}$$

but this is not a symmetry of the staggered action because of the taste-breaking term. The local scalar meson from Eq. 2.93 becomes degenerate in the continuum limit to its taste partners, including the non-local scalar meson with the anomaly, due to the restoration of taste symmetry [36]. Note that both axial chiral rotations Eq. 2.90 and Eq. 2.94 could however only be symmetries of the staggered action in the massless limit (chiral limit). Since for our calculations the continuum limit has to be done before the chiral limit, we can calculate any of those scalar mesons. We chose the local scalar meson because it is easier to analyze.

After understanding why there is a relative minus sign between the two states inside a staggered meson correlator, we want to look at the content of a simple summation over a correlator, i.e. our susceptibilities. To understand the content we look at the summation of the correlator and the same procedure for a single state correlator, which would not have a definitive separation distance of $n_\tau a$ as we made our correlator by construction; see section 2.7.

We start with the temporal mesonic staggered correlator. In this case we have to sum over all lattice distances n_τ

$$\chi_M = \sum_{n_\tau=0}^{N_\tau-1} \phi(n_\tau)\tilde{C}_M, \tag{2.95}$$

where $\tilde{C}_M$ describes one meson staggered correlator with projection to momentum zero and a function $\phi(n_\tau)$, which is specific to the channel and will be defined in just a bit.

Let us begin with the $M2$ channel. The interesting particle in this channel is obviously the pion since it is the only particle available. The susceptibility is then

$$\begin{aligned}\chi_\pi = &\sum_{n_\tau=0}^{N_\tau-1} \phi(n_\tau)\tilde{C}_{M2}(n_\tau) = \sum_{n_\tau=0}^{N_\tau-1} \phi(n_\tau) C_2 \sum_{\vec{n}} \mathrm{tr}[M_{f'}^{-1}(n|0) M_f^{-1\dagger}(n|0)] \\ =&C_2 \sum_n \phi_(n_\tau)\mathrm{tr}[M_{f'}^{-1}(n|0) M_f^{-1\dagger}(n|0)],\end{aligned} \tag{2.96}$$

where the initial phase factor of the channel is $\phi(\mathbf{x}) = 1$. We want to compare that to a summed over correlator with only the pion state in the sink. Such a correlator reads

$$\tilde{C}_{\gamma_5}(h_4) = \frac{C_2}{2} \sum_{\vec{n}} \sum_{s_4} \mathrm{tr}[M_{f'}^{-1}(n|0) M_f^{-1\dagger}(n|0)]. \tag{2.97}$$

Note that due to neglecting of the second state, a factor of $\frac{1}{2}$ enters as well as a summation over s_4. Combining that kind of correlator with an additional summation over the separation distance n_τ leads to a double summation over s_4, which introduces a factor of 2. It follows

$$\chi_\pi = \sum_{n_\tau=0}^{N_\tau-1} \tilde{C}_{\gamma_5}(h_4) = C_2 \sum_n \mathrm{tr}[M_{f'}^{-1}(n|0) M_f^{-1\dagger}(n|0)]. \tag{2.98}$$

If we compare Eq. 2.96 to Eq. 2.98, it follows that the specific function in this case is $\phi(n_\tau) = 1$. Therefore a simple summation over $\tilde{C}_{M2}(n_4)$ leads to a susceptibility of only one state, here the pion. For spatial correlators we have to again interchange $n_\tau \leftrightarrow n$ as well as $N_\tau \leftrightarrow N_s$.

How are the factors for the other channels? Since the interesting state is either in the non-oscillating or in the oscillating part, the factor $\phi(n_\tau)$ for other non-oscillating parts is also $\phi(n_\tau) = 1$. In this case the interesting channels are $M6$, $M7$ and for temporal correlators also $M8$. It follows for the spatial correlators for the vector susceptibility

$$\chi_\rho = \sum_{n=0}^{N_s-1} \tilde{C}_{M67}(n), \tag{2.99}$$

where $\tilde{C}_{M67}(n) = \frac{\tilde{C}_{M6}(n)+\tilde{C}_{M7}(n)}{2}$. This combined correlator helps to increase the statistics.

Now we will check the susceptibilities for the oscillating part. The temporal correlator for the $M1$ channel reads

$$\tilde{C}_{M1}(n_4) = C_2 \sum_{\vec{n}} (-1)^{n_1+n_2+n_3} \mathrm{tr}[M_{f'}^{-1}(n|0) M_f^{-1\dagger}(n|0)], \tag{2.100}$$

while the temporal correlator with only the scalar state reads

$$\tilde{C}_{\mathbb{1}}(h_4) = \frac{C_2}{2} \sum_{\vec{n}} \sum_{s_4} (-1)^{n_1+n_2+n_3+n_4} \mathrm{tr}[M_{f'}^{-1}(n|0) M_f^{-1\dagger}(n|0)]. \tag{2.101}$$

The scalar susceptibility is

$$\chi_{a_0} = -\sum_{n_\tau=0}^{N_\tau-1} \tilde{C}_{\mathbb{1}}(h_4) = -C_2 \sum_n (-1)^{n_1+n_2+n_3+n_4} \mathrm{tr}[M_{f'}^{-1}(n|0) M_f^{-1\dagger}(n|0)], \tag{2.102}$$

where again a factor of 2 arises due to the double summation over n_τ and the minus accounts for getting the true scalar state due to the rise of i^2 from $U_\epsilon(1)$ rotations inside the interpolators; see Eq. 2.90. For the $M1$ channel

the susceptibility reads

$$\chi_{a_0} = \sum_{n_\tau=0}^{N_\tau-1} \phi(n_\tau)\tilde{C}_{M1}(n_\tau) = C_2 \sum_n \phi(n_\tau)(-1)^{n_1+n_2+n_3}\mathrm{tr}[M_{f'}^{-1}(n|0)M_f^{-1\dagger}(n|0)]$$
$$\stackrel{!}{=} -C_2 \sum_n (-1)^{n_1+n_2+n_3+n_4}\mathrm{tr}[M_{f'}^{-1}(n|0)M_f^{-1\dagger}(n|0)]. \tag{2.103}$$

To fulfill Eq. 2.103 the phase factor needs to be $\phi(n_\tau) = -(-1)^{n_\tau}$. The formula for the a_0 susceptibility is therefore

$$\chi_{a_0} = -\sum_{n_\tau=0}^{N_\tau-1} (-1)^{n_\tau}\tilde{C}_{M1}(n_\tau). \tag{2.104}$$

Again, similarly the one for the axialvector susceptibility with spatial correlators reads

$$\chi_{a_1} = -\sum_{n=0}^{N_s-1} (-1)^{n}\tilde{C}_{M34}(n), \tag{2.105}$$

where $\tilde{C}_{M34}(n) = \frac{\tilde{C}_{M3}(n)+\tilde{C}_{M4}(n)}{2}$ is again a combined correlator to increase the statistics.

In the next section 2.9 the connection between pure lattice numbers and physical units will be discussed.

2.9 Connection between lattice and physical units

To get any meaningful results from lattice calculations it is necessary to connect them to physical units. This is done by so-called scale setting. Since in this thesis natural units $\hbar = c = 1$ are used, everything can be related to the lattice spacing a. The lattice spacing describes the distance between nearest neighbor lattice points and is not directly known by the setup or during calculation. Only through scale setting the lattice gets a physical meaning in sense of distance in meters or, usually used in our case, femtometers fm. Therefore every quantity is calculated first in lattice units, which are dimensionless. That means that the physical quantity depends on factors of a, e.g. the calculated mass on the lattice is am, where m is the physical mass with its physical unit MeV.

For setting the scale it is in general preferred to have an experimentally well known quantity, which is cheap and easy to compute on the lattice with small statistical and systematic uncertainties (which includes cut-off effects) and quark mass dependence. Different scale setting schemes usually result in different lattice spacings for same lattice setups. That is due to the non-uniqueness of scales at finite lattice spacing a. Nonetheless they should all

agree in the continuum limit.

The general scale setting procedure amounts to establish a relation between the bare coupling g_0, which is related to the inverse coupling β, and the lattice spacing a. E.g. if a dimensionless mass M is calculated on the lattice and is related in physical units as $M = am$ the scale would be

$$a_{m-\text{scale}}(g_0) = \frac{M(g_0)}{m}, \tag{2.106}$$

where m is the same mass as M but already known by experiment in physical units and $a_{m-\text{scale}}(g_0)$ is the lattice spacing at bare coupling g_0 in the example $m-$scale. From Eq. 2.106 it is clear that good scale setting is important since (when quark masses are neglected) any uncertainty propagates linearly into a hadron mass. To fix quark masses the scale already enters decisively into fixing the bare quark masses of the Lagrangian and therefore into planning of the simulation. Thus good scale setting requires little to no quark mass dependence. On the one hand setting the scale by using e.g. the proton mass would be a bad idea since it has strong quark mass dependence, thus it makes tuning of quark masses rather difficult. On the other hand weak quark mass dependence also helps extrapolating the scale for non-physical quark masses more easily because experimental input is needed to set the scale initially, which in experiment is at physical quark masses. Keep in mind that trajectories for reaching the physical point can lead to different sensitivity to quark masses.

In this work mass-degenerate u and d quarks are used while the s quark mass stays fixed at its physical value. Throughout this thesis the Kaon decay constant f_K has been used to set the scale. It is used to perform the primary scale setting and to determine values of the theory scales like r_0 and r_1. The largest drawback of decay constants is that they are related to weak processes. Therefore the precision of them depends on our knowledge of the CKM matrix elements. The big advantage on the other side is that they have long plateaus for scale setting [37].

In the final section of this chapter 2.10 we go into the details of why the $U_A(1)$ symmetry is so important and how that is related to the QCD phase diagram.

2.10 $U_A(1)$ symmetry and universality class

One aspect for understanding the QCD phase diagram and especially the critical point is the fate of $U_A(1)$ at the phase transition for vanishing chemical potential $\mu_B = 0$ in the chiral limit $m_l \to 0$ [16–18].

The naive fermion action

$$S_F[\psi,\bar{\psi},U] = a^4 \sum_{n\in\Lambda} \bar{\psi}(n) \left(\sum_{\mu=1}^{4} \gamma_\mu \frac{U_\mu(n)\psi(n+\hat{\mu}) - U_{-\mu}(n)\psi(n-\hat{\mu})}{2a} + m_0\psi(n) \right) \tag{2.107}$$

is for vanishing light quark masses $m_u = m_d = m_l$ in the mass matrix m_0 invariant under $U_A(1)$ rotations (Eq. 2.53). However observables X, calculated e.g. with a correlator

$$C = \langle X \rangle = \frac{1}{Z} \int \mathcal{D}[\psi,\bar{\psi}]\mathcal{D}[U] \exp(-S_{\mathrm{QCD}}[U,\psi,\bar{\psi}]) X[U,\psi,\bar{\psi}], \tag{2.108}$$

where $\mathcal{D}[\psi,\bar{\psi}]$ is the measure, are not necessarily invariant under $U_A(1)$ rotations. In fact, after calculating the necessary Jacobian determinant $\mathcal{J}$ of that transformation, we get

$$\begin{aligned} \mathcal{D}[\psi,\bar{\psi}] &= \mathcal{D}[\psi',\bar{\psi}']\mathcal{J}^{-2} \\ &= \mathcal{D}[\psi',\bar{\psi}'] \exp\left(i \int \mathrm{d}^4x \; \alpha(x) \left(\frac{g^2}{16\pi^2} \epsilon_{\mu\nu\lambda\sigma} F^c_{\mu\nu} F^c_{\lambda\sigma} \right) \right), \end{aligned} \tag{2.109}$$

where α is the rotation angle, F is the gluon field strength tensor and ϵ is the four dimensional Levi-Civita symbol [38]. This invariance, which only exists if the measure is separately invariant under the rotation, is called the anomaly of $U_A(1)$. That is in contrast to the $SU_A(2)$ symmetry, which does not have an anomaly, but is broken spontaneously in the chiral limit $m_l \to 0$ at lower temperature T, which leads due to Goldstone's theorem to massless Goldstone bosons. In the case of $SU_A(2)$ there would be a triplet of massless bosons because three symmetries would be broken. Since $SU_A(2)$ is a weakly explicitly broken symmetry, i.e. still a good approximate symmetry, this triplet of bosons is expected to have low masses. Indeed we can identify this triplet as the pion triplet of $\pi^\pm$ and π^0, which is expected to have zero mass in the chiral limit $m_l \to 0$ for low temperature T, where the symmetry is spontaneously broken. The $U_A(1)$ however is explicitly broken by the anomaly while the spontaneous symmetry breaking is restored at lower or at the same T as the anomalous symmetry breaking, and therefore no Goldstone boson is associated in this case. It is also the reason for the large mass gap between the pseudoscalar η and η' [17].

The anomaly of $U_A(1)$ has been the focus of many studies [13–15]. Why is the anomaly of $U_A(1)$ so important? Near a critical point scaling of observables depends on the universality class of that critical point [8, 19]. The universality class depends on the breaking (or restoration) pattern of the symmetry group. For dynamical QCD with (2+1)-flavors at vanishing μ_B

and physical quark masses the transition is a crossover. Towards vanishing light quark masses m_l a second order phase transition arises there. In Fig. 2.2 an illustration of the phase transition as a function of m_l and m_s for $\mu_B = 0$ is shown. The dark green lines are second order phase transitions, which are critical points. Since the anomaly of $U_A(1)$ is an anomaly we do not initially know if $U_A(1)$ is in the larger symmetry group or not. The QGP phase, which is above the phase transition temperature, can be described by the larger symmetry group. The hadronic phase, which is below the phase transition temperature, can be therefore described by the smaller symmetry group. We know that in the hadronic phase $U_A(1)$ as well as $SU_A(2)$ are broken. We also know that in the QGP phase the spontaneous breaking of $SU_A(2)$ disappears and the symmetry gets effectively restored shortly after the phase transition. But we do not know if the anomalous $U_A(1)$ also gets effectively restored at T_c in the chiral limit.

Fig. 2.2 are the so-called Columbia plots. In these plots the dotted lines from the physical point to $m_l = 0$ is the so-called chiral limit for (2+1)-flavor QCD, which we are interested in. The left plot of Fig. 2.2 is the scenario that current research leans toward [39, 40]. In this scenario the phase transition is second order at $m_l = 0$ for physical strange quark mass m_s. Two different universality classes are possible depending on if $U_A(1)$ is broken or has very small breaking, i.e. an effective symmetry restoration, at the phase transition temperature. In case of a broken $U_A(1)$ the universality class of this critical point is $O(4) \to O(3)$ and in the case of an effectively restored $U_A(1)$ the universality class of this critical point is $U(2) \times U(2) \to U(2)$ [16]. Which one of those will be realized depends then on the strength of the anomalous breaking of $U_A(1)$ [15].

In the right plot of Fig. 2.2 the second scenario is plotted. In that case the transition region from the lower left corner extends to the physical value of m_s. The phase transition is then first order in the chiral limit and the universality class of the corresponding critical point at a specific $m_l < m_{l,\text{phys.}}$ and $\mu = 0$ is $Z(2)$.

Knowing the universality class of this critical point helps us to understand the QCD phase diagram. If the scenario in the left plot of Fig. 2.2 is realized we expect a tricritical point at some non-vanishing μ_B at $m_l = 0$. This is illustrated in Fig. 2.3. We therefore get a connection between the critical point in our calculation and the Critical End Point (CEP) of the physical QCD. In Fig. 2.3 the CEP is the light blue point, the tricritical point is the violet point connecting the black, blue and red solid lines. Through our calculations we are tiptoeing towards the red point in that scenario. The CEP of QCD is of special interest theoretically as well as experimentally and was the main interest of the first funding period of the CRC-TR211 collaboration in which the research of this thesis was done.

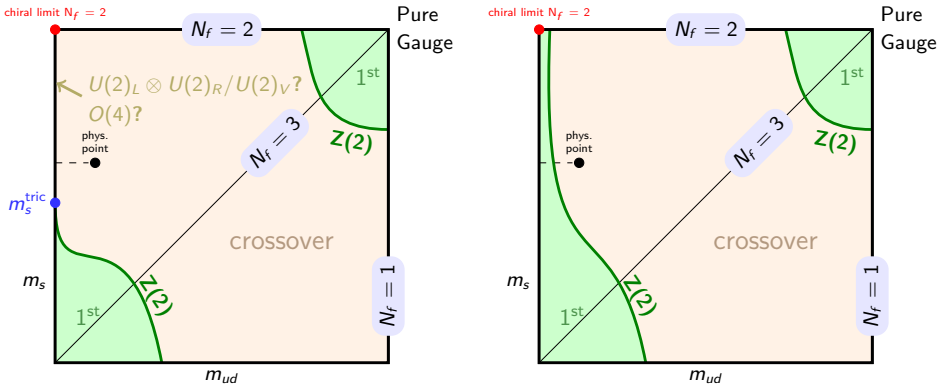

Figure 2.2: The Columbia plots show the order of the phase transition for $\mu_B = 0$ for different values of m_{ud} and m_s in the case of $N_f = 1$, $N_f = 2$, $N_f = 2 + 1$ and $N_f = 3$ QCD. Dotted lines indicate the chiral limit extrapolation in $N_f = 2+1$ QCD. The left plot is one possible scenario. The right plot is the other possible scenario. For details see text. Plots taken from Ref. [41].

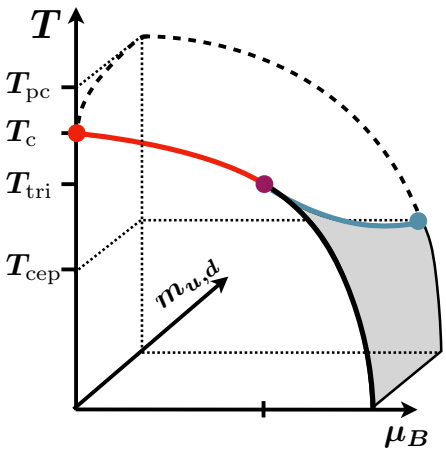

Figure 2.3: Possible QCD phase diagram with temperature T, baryon chemical potential μ_B and light quark mass $m_{u,d}$. Dashed lines are crossover transitions while the solid red and blue lines are second order phase transitions. The grey area are first order phase transitions. Plot taken from Ref. [42].

A possible effectively restored $U_A(1)$ symmetry should be observable by calculating meson correlators, which can transform into each other via $U_A(1)$ rotations [43]. Two of these correlators consist of the ground state isovector pseudoscalar and scalar mesons with a light-light quark flavor combination;

see section 2.8. In fact all masses in those correlators have to be identical on each level if $U_A(1)$ is effectively restored. Since we are dealing with staggered fermions, this degeneration of correlators is hard to see if at all since a continuum limit extrapolation has to be done beforehand to restore taste symmetry and thus to receive correct correlators. Therefore one focus is on the ground state masses of these particle spectra. For a better mass extraction screening meson correlators will be used here instead of temporal ones. That changes the interpretation of the observables but does not change the fact that both correlators are connected via $U_A(1)$ rotations if the symmetry is restored. Screening masses can be interpreted as the inverse length scale over which a perturbation is screened by the plasma [15]; more information on that in subsection 2.7.1. Besides screening masses the corresponding susceptibilities should also become degenerate and therefore the second focus is on these observables. See section 2.8 for details on chiral symmetries and these susceptibilities.

Since the $U_A(1)$ symmetry is an interesting topic, a lot of research has already been done. We now want to briefly give an overview here to put the final results of this thesis later into context of the current research.

On one side we have studies, which support a broken $U_A(1)$ symmetry in the chiral limit after the phase transition temperature: In the study [44] domain wall fermions were used. This study also analyzed screening correlators of π and a_0 (named δ in this study). For the $U_A(1)$ symmetry they were looking at the susceptibility difference of those two correlators like in our study and concluded that the $U_A(1)$ symmetry remained broken. However this study did only use a small lattice size with a pion mass of 200 MeV and did not perform any thermodynamic, continuum or chiral limit extrapolation. A similar result was brought by another study [45]. This study also used domain wall fermions and also came to the conclusion that the $U_A(1)$ symmetry remains broken at the phase transition temperature in the chiral limit. This was basically a follow-up study with larger lattice sizes, which tried to investigate the finite volume effects, done by a different group. Another study [46] looked at the eigenvalues of the overlap operator using HISQ configurations to calculate the susceptibility difference. Even though volume effects were taken into account, the continuum and chiral limit extrapolations were still missing. The study [47] also found similar to Ref. [46] that the $U_A(1)$ symmetry is broken. The study used similar to Ref. [46] eigenvalues of the overlap operator using HISQ configurations to calculate the susceptibility difference. Volume effects and the chiral limit were taken into account, but not the continuum limit. Finally the study [48] looked at Dirac eigenvalues using HISQ configurations calculating the susceptibility difference. It was found that the $U_A(1)$ symmetry remains broken even at higher temperatures ($T \approx 1.6T_c$). This study performed all three extrapolations.

On the other side are studies, which support an effectively restored $U_A(1)$ symmetry in the chiral limit at the phase transition temperature: The study [49] used overlap fermions and calculated meson correlators and Dirac operator spectral density. This study took finite volume effects into account, but not the continuum limit. Another study [15] used $\mathcal{O}(a)$-improved Wilson fermions and calculated screening correlators of mesons similar to our study. Finite size effects were taken into account, but again not the continuum limit. Both studies concluded that the $U_A(1)$ symmetry gets effectively restored at the transition temperature in the chiral limit. The study [50] used domain wall fermion configurations and calculated eigenmodes of the domain wall as well as the overlap Dirac operator. This study has taken finite size and cut-off effects into account and did a chiral limit extrapolation, but not by thermodynamic or contiuum limit extrapolations. It concluded that an $U_A(1)$ symmetry gets effectively restored in the chiral limit by using a reweighting technique. The investigated temperature range was 190-220 MeV, which is a range of around 1.11-1.3 T_c ($T_c \approx 170$ MeV for two-flavor QCD [51]), where T_c is the chiral phase transition temperature of the $N_f = 2$ QCD, which this paper studied. Finally the study [52] is a follow-up study of Ref. [50] with a similar set-up increasing the upper bound of their temperature range to 330 MeV and the same conclusion.

In the next chapter 3 we explain the technical details from the lattice calculation to the extrapolated values and in chapter 4 we show the corresponding results of this thesis.

Chapter 3

Methodology

In this chapter the technical methods for getting the final results from the calculated numbers from lattice QCD are explained in details. For now we calculated spatial meson mass correlators in dynamical QCD using the Highly Improved Staggered Quark (HISQ) action with (2+1)-flavors, fixing the strange quark mass m_s at its physical value and varying the two degenerate light quark masses m_l towards the chiral limit around their transition temperature T_{pc}.

3.1 Extracting masses from correlators

Unlike the susceptibilities for e.g. pseudoscalar and scalar channels, which can be calculated by

$$\chi_\pi = \sum_{n=0}^{N_s-1} \tilde{C}_{M2}(n), \qquad \chi_{a_0} = -\sum_{n=0}^{N_s-1} (-1)^n \tilde{C}_{M1}(n), \tag{3.1}$$

where $\tilde{C}_M$ are the meson correlators with a projection to zero momentum (for details see section 2.8), the masses for these channels have to be extracted through fitting the correlator with

$$\tilde{C}_M(n) = \sum_{i=0}^{N_{no}} A_i \cosh(m_{i,no}(n - N_s/2)) - (-1)^n \sum_{i=0}^{N_{osc}} B_i \cosh(m_{i,osc}(n - N_s/2)) \tag{3.2}$$

and getting the mass through a fitting parameter. An exception to that fitting function is the $M2$ channel, which does not have an oscillating part *osc*; see Tab. 2.1.

However, there are a few challenges that have to be overcome here [12, 53]:

1. The ground state mass dominates in the middle of our correlator, but the middle of our correlator is also noisier. We therefore want to use

multi-state fits and extract the ground state mass from them. Since in a multi-state fit there are many parameters to be fitted, the fit may become unstable without a good initial guess. The way we overcome this is to construct higher state fits by first estimating initial guesses for lower state fits and then fit on the difference between the correlator and this lower state fit. With this procedure one gets an initial guess for a fit with one more state than the starting fit. In a second step we can fit this higher state fit using the initial guess and then we repeat the procedure.

2. Higher state fits will always be more accurate than lower state fits due to possible overfitting. Overfitting means that the fit is too closely to the data points and will fail to predict future data points. We overcome this challenge by using a selection criterion that also considers the number of parameters to counter overfitting. In our case we use the corrected Akaike Information Criterion (AICc) [54]. For every parameter in our fit the value gets increased linearly and for larger values of the likelyhood function it decreases logarithmically. The corrected version deals with the fact that we have a small sample size, where the normal AIC would overfit naturally, by adding an additional term, which also considers the sample size relative to the parameters.

3. Getting a reliable mass plateau. At this point there is only a fit chosen for the whole range. This fit has only one value for the ground state mass and might not be accurate. To overcome this, we use different ranges for the fits to get different ground state masses and construct a mass plateau.

In Fig. 3.1 we show an example of the fitting where a typical $M2$ channel meson correlator with two light quark masses is plotted. This example is for a lattice size of $56^3 \times 8$ at mass ratio $m_s/m_l = 80$ and coupling $\beta = 6.390$ with two non-oscillating states using the usual (2+1)-flavor HISQ action with physical strange quark mass. The colors indicate from red to blue different fitting ranges which increase from the middle of the lattice, i.e. the end of the plotted correlator, to the beginning of the lattice $n_\sigma = 1$. Note that due to periodicity of the lattice only one half of the correlator should be unique. For this reason the second half of the correlator is folded on top of the first half to increase the statistics. For all used fitting ranges the parameters and their respective AICc are saved. Note also that only in this channel the fits lie under their data points. That is because the weighted least squares shifts the fits away from the data points due to the off-diagonal matrix elements in their covariance matrix. In this channel the distribution of data points is not normal but log-normal as we will see in section 4.2. This results in negative off-diagonal elements in the covariance matrix, which shifts the fits

always below the data points. This is special to the $M2$ channel and does not happen in the other channels as they are normal distributed as we will see in section 4.2. As one counter measure we use the AICc, which considers the likelihood function. Another counter measure is to have a large amount of configurations in relation to the lattice size, such that the shift is still within the error bars of the data points as in the $M2$ channel example in section 4.2. One way to solve this "problem" in the $M2$ channel completely is to have a vast amount of configurations, such that the distribution is (almost) normal instead of log-normal.

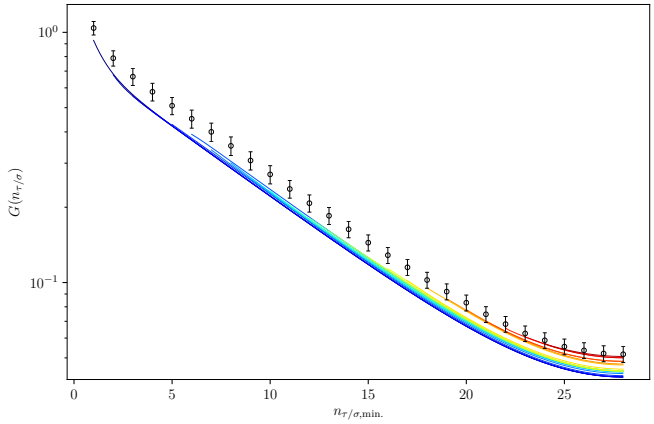

Figure 3.1: Example for a two-state fit along a spatial direction. This example is for a $56^3 \times 8$ lattice in the $M2$ channel at coupling $\beta = 6.390$ with mass ratio $m_s/m_l = 80$. On the x-axis is the separation distance and on the y-axis is the correlator value in lattice units. The correlator has been symmetrized by folding the second half onto the first half, which is shown here. Starting from the center of the lattice ($n_{\sigma,\text{max}} = 28$) we used various ranges from $n_{\sigma,\text{min}} = n_\sigma = 24$ to 1 as left bound for the two-state fit indicated by the different colors ranging from red to blue as the range increases.

In the second step the AICc values of all different fits are compared to each other at all fitting ranges. Only the mass corresponding to the lowest AICc value for each fitting range is used in the following analysis. E.g. if at a fitting range starting from $n_\sigma = 10$ the fit with one non-oscillating state has the lowest AICc compared to the fit with two non-oscillating states and the fit with three non-oscillating states, the ground state mass parameter of the fit with one non-oscillating state is used in the following analysis as the ground state mass for starting distance $n_\sigma = 10$. See Fig. 3.2 for the AICc values for this example.

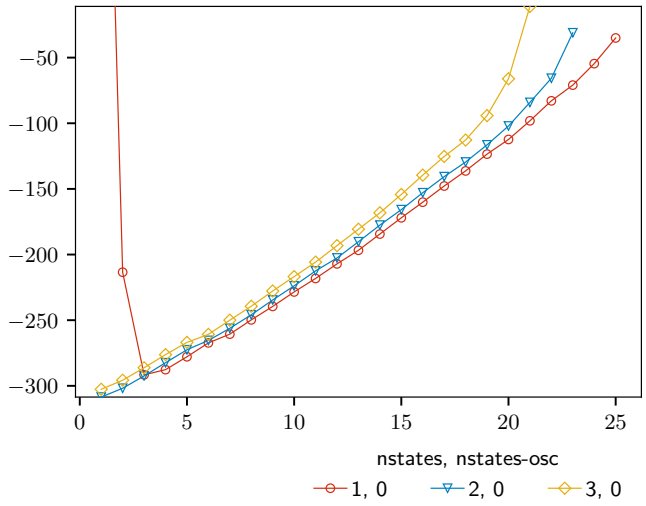

Figure 3.2: Example for an AICc selection. This example is for a $56^3 \times 8$ lattice in the $M2$ channel at coupling $\beta = 6.390$ with mass ratio $m_s/m_l = 80$ as shown in Fig. 3.1. On the x-axis is n_σ and on the y-axis is the AICc value. Only the lowest AICc values will be selected for the mass plateaus. In this example at small n_σ the two-state fit will be selected but for the rest of the correlator the one-state fit will be selected. The shown three-state fit however will not be chosen and hence is irrelevant for further analysis.

In Fig. 3.3 the corresponding ground state masses are plotted. Note that only for the AICc selection relevant states are plotted; in that case the fit with three non-oscillating states were never selected and therefore is not shown.

In Fig. 3.4 the resulting mass plateau is plotted. Note that lower $n_\sigma = n_{min}$ means that more of the correlator is fitted. Flat mass plateaus in this area are therefore preferred because they have less statistical uncertainty due to more included lattice points. In this example the mass plateau is very stable and long. Usually the length of mass plateaus in the $M2$ channel is longer than the mass plateaus of the other channels due to the additional oscillating part in the other channels and therefore possibly more selected fit combinations. Unlike the effective mass, which usually plateaus around the center of the correlator and has similar noise for all data points, our method produces a larger plateau and can work better around noisy data points, as we have in correlators with an oscillating part. We will show our mass results in section 4.3.

In the next section 3.2 we look into the first extrapolation, which we need to perform to answer the main question of this thesis: Is the $U_A(1)$ symmetry effectively restored at the chiral phase transition?

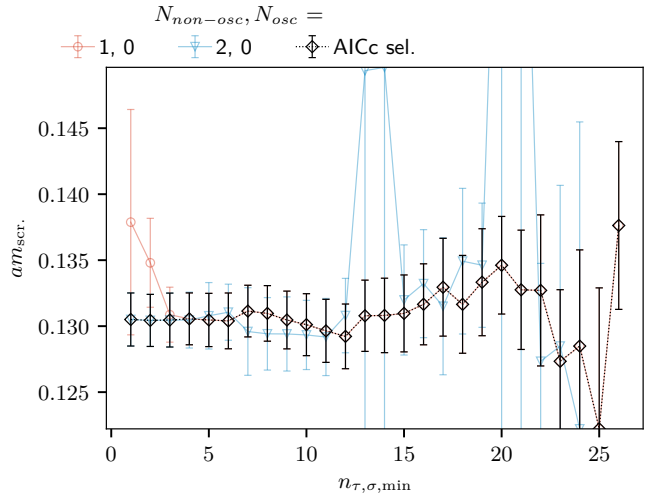

Figure 3.3: Example for AICc selected ground state screening masses. This example is for a $56^3 \times 8$ lattice in the $M2$ channel at coupling $\beta = 6.390$ with mass ratio $m_s/m_l = 80$ as shown in Fig. 3.1. Shown are the fit parameter values for the ground state mass of the selected fits from Fig. 3.2. In black are the selected values by the AICc criterion.

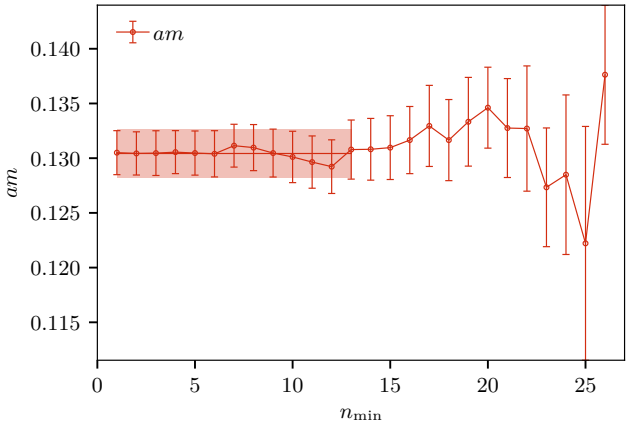

Figure 3.4: Example for the mass plateau selection. This example is for a $56^3 \times 8$ lattice in the $M2$ channel at coupling $\beta = 6.390$ with mass ratio $m_s/m_l = 80$ as shown in Fig. 3.1. From the AICc selected masses an adequate range for the final mass value is selected where the mass plateau is created as shown in Fig. 3.3. The values here seem to be stable enough in a sense of a real plateau.

3.2 Thermodynamic limit extrapolation

The first limit we need to take is the infinite volume limit, also known as the thermodynamic limit. The goal is to remove finite volume effects, which arise naturally on the lattice because of the finite extent that all lattices have.

First we need to consider the form of the fitting function. The finite volume dependence of the screening mass is expected to follow a power law rather than an exponential form at zero temperature [55] and a different power law for the free case. For screening masses we expect therefore

$$m_{N_s/N_\tau} = m_{N_s\to\infty/N_\tau}\left(1 + b_{N_\tau}\left(\frac{N_\tau}{N_s}\right)^c\right), \tag{3.3}$$

where m_{N_s/N_τ} is the screening mass calculated on a $N_s^3 \times N_\tau$ lattice, $m_{N_s\to\infty/N_\tau}$ is the screening mass in the thermodynamic limit at a specific N_τ, which is along with b_{N_τ} and c also a fitting parameter. It is $c = 3$ for $T = 0$ and $c = 1$ for the free case at $T \to \infty$ [55]. We therefore assume that for finite temperature it should be $c \in [1, 3]$. Thus we restrict c to be inside this interval. We futhermore assume that c only depends on temperature T and the number of temporal lattice points N_τ. For $m_{N_s\to\infty/N_\tau}$ and b_{N_τ} we assume that they depend on N_τ, particle type (e.g. pseudoscalar, scalar) and temperature T. Therefore a combined fit with a shared parameter c between pseudoscalar and scalar particles at fixed N_τ and T is possible. With these assumptions we have five parameters to set with two sets of data points, i.e. pseudoscalar and scalar masses. Therefore we need at least three different volumes at fixed N_τ and T to perform a fit with six data points.

For the thermodynamic limit of the susceptibilities we use a simpler ansatz. In contrast to screening masses we need to build manually an observable out of susceptibilities, which is multiplicatively and additively renormalized [8]. We therefore take the thermodynamic limit with

$$\left(m_s^2\frac{\chi_{\pi/\rho} - \chi_{a_0/a_1}}{f_K^4}\right)_{N_s} = \left(m_s^2\frac{\chi_{\pi/\rho} - \chi_{a_0/a_1}}{f_K^4}\right)_{N_s\to\infty}\left(1 + \frac{d_{N_\tau}}{N_s^3}\right), \tag{3.4}$$

where the difference between these two susceptibilities makes this observable additively renormalized, the mass multiplication of m_s^2 multiplicatively renormalized and the Kaon decay constant f_K^4 makes it dimensionless. For the susceptibilities we have two parameters and only one set of data points. Therefore we need at least three different volumes to still have an underconstrained system to fit like for the screening masses. Note that χ_π is related to $\langle\bar{\psi}\psi\rangle_l$ by

$$\chi_\pi = \frac{\langle\bar{\psi}\psi\rangle_l}{m_l}. \tag{3.5}$$

The behaviour in the thermodynamic limit for $\langle\bar{\psi}\psi\rangle_l$ has been studied in [8].

In former studies [53, 56] the effects of thermodynamic limit extrapolation for screening masses seemed negligible to the statistical uncertainty for lattices at large enough volumes. Our volumes fulfill the requirement of $N_s/N_\tau \geq 4$, therefore we expect that this correction is also small in our case. Because we have smaller light quark masses than in those studies, we want to verify that expectation here as well. Results on thermodynamic limit extrapolations will be shown in section 4.4 where we will also discuss it in more detail.

In the next section 3.3 we will look into the second extrapolation needed to answer the main question of this thesis. In this step we transition from the lattice back into continuum physics.

3.3 Continuum limit extrapolation

The second limit we have to take is the continuum limit. The goal is to extrapolate to vanishing lattice spacing $a \to 0$. The cut-off effects result from the action S. In all lattice QCD calculations the action is

$$S_{\text{latt}} = S_{\text{cont}} + \mathcal{O}(a^n) \tag{3.6}$$

by construction. For the HISQ action it is expected that the cut-off effects are of $\mathcal{O}(a^2)$. To check for significant higher orders of cut-off effects in a a first estimate with just a^2 cut-off effects are assumed and verified if it seems linear. Therefore for screening masses we fit

$$m_{N_\tau} = m_{N_\tau\to\infty}\left(1 + b_{\text{mass}}\frac{1}{N_\tau^2}\right) \tag{3.7}$$

using the infinite volume extrapolated masses. Similarly for our combined susceptibilty observable we first assume

$$\left(m_s^2\frac{\chi_\pi - \chi_{a_0}}{f_K^4}\right)_{N_\tau} = \left(m_s^2\frac{\chi_\pi - \chi_{a_0}}{f_K^4}\right)_{N_\tau\to\infty}\left(1 + b_{\text{susc}}\frac{1}{N_\tau^2}\right), \tag{3.8}$$

where the infinite volume extrapolated susceptibilties are used. In both cases the infinite volume extrapolated values are inserted on the left-hand side of this equation.

In Eq. 3.7 and Eq. 3.8 the fitting parameters are $m_{N_\tau\to\infty}$ or $\left(m_s^2\frac{\chi_\pi-\chi_{a_0}}{f_K^4}\right)_{N_\tau\to\infty}$, which are the continuum limit values of the respective observable, and b_{mass} or b_{susc}, respectively. Assuming that scalar and pseudoscalar meson masses experience different cut-off effects we have therefore two parameters to set by our fits for every observable. Thus we need values from three different

lattice spacings a, i.e. values from three different N_τ, at fixed temperature T to have an underconstrained system to fit them.

To check if the effect of thermodynamic limit extrapolations is also small on this stage of the extrapolation we also used just largest volume values as input parameters for the continuum limit and compared them to the proper extrapolations. Results on those continuum limit extrapolations will be shown and discussed in section 4.5.

In the last section of this chapter 3.4 we cover the last necessary extrapolation. In this step we remove the explicit breaking of the chiral symmetries through the light quark mass m_l.

3.4 Chiral limit extrapolation

At this point all values should be continuum extrapolated. For this work the values at $m_l = 0$ are of special interest. Unfortunately these values can not be directly computed at $m_l = 0$ since the Dirac operator at these values can not be accessed numerically. To overcome this problem an extrapolation for different light quark masses m_l to $m_l = 0$ can be taken. Therefore the third and last limit we want to take is the chiral limit $m_l \to 0$. In the chiral symmetry broken region at low temperature and also in the region close to but below the transition temperature we know that it is

$$m_\pi(m_l) = m_\pi(m_l = 0) + b\sqrt{m_l/m_s}, \tag{3.9}$$

where $m_\pi(m_l = 0) = 0$ because of the Goldstone phenomenon, for the pion screening mass m_π. This results from an analysis of pion pole masses around the phase transition at very low m_l [57]. At higher temperatures mesons with light masses like the m_π in the chiral limit should behave similar. Therefore we will assume for m_{a_0}, which would become degenerate to m_π if $U_A(1)$ symmetry gets effectively restored, a behavior in the vicinity of this square root behavior in m_l. In particular we will fit for the difference of m_π and m_{a_0} a square root function as in Eq. 3.9, a linear fitting function and a combination of those two ideas.

Our observable made out of susceptibilities $m_s^2 \frac{\chi_\pi - \chi_{a_0}}{f_K^4}$ on the other hand diverges in the chiral limit below the transition temperature because of χ_π's behaviour in the limit of vanishing m_l, not being degenerate to χ_{a_0} and $\langle\bar{\psi}\psi\rangle_l$ being non-zero below the transition temperature, cf. Eq. 3.5. From Ref. [58, 59] it can be derived that

$$\langle\bar{\psi}\psi\rangle_l \approx c + c'\sqrt{m_l}, \tag{3.10}$$

for $T < T_c$ assuming the $3d$ $O(4)$ spin model as universality class of the

critical point. That means that

$$\chi_\pi \approx \frac{c}{m_l} + \frac{c'}{\sqrt{m_l}}. \tag{3.11}$$

We want to assume that χ_π and χ_{a_0} will behave similar to Eq. 3.11 since they should become degenerate at some high enough temperature T since they are connected by $U_A(1)$, which should be effectively restored at large enough T. We want to assume that behaviour even around T_c in contrast to their universal behaviour at T_c (cf. [8]) and since the light quark masses are in the denominator we want to invert the function for a chiral limit extrapolation. Using Taylor expansion we get

$$(\chi_\pi - \chi_{a_0})^{-1} = \tilde{c} m_l + c'' \sqrt{m_l}^3, \tag{3.12}$$

where $\tilde{c}$ and c'' are free parameters. This function however would go trivially to zero in the chiral limit, which would imply that $(\chi_\pi - \chi_{a_0})$ is always diverging and that means that the $U_A(1)$ symmetry would be broken by definition. To account for a potential restoration, which would be for a diverging $(\chi_\pi - \chi_{a_0})^{-1}$, we introduce a parameter d

$$(\chi_\pi - \chi_{a_0})^{-1} = d + \tilde{c} m_l + c'' \sqrt{m_l}^3. \tag{3.13}$$

We want to compare that approach to a fitting function of

$$\chi_\pi - \chi_{a_0} = d + \tilde{c} m_l + c'' \sqrt{m_l}^3, \tag{3.14}$$

where the parameter d is a measure for the anomalous $U_A(1)$ symmetry breaking. Since we have no predictions here, we try these fitting functions and also compare them to the cases were we set $\tilde{c}$ or c'' to zero.

In the next chapter 4 we will show the results of this thesis.

Chapter 4

Results

In this chapter results for screening masses and their respective susceptibilities will be presented. Our main focus is the fate of the anomalous part of $U_A(1)$. For that we calculated mesonic screening correlators in dynamical QCD using the Highly Improved Staggered Quark (HISQ) action with (2+1)-flavors, fixing the strange quark mass m_s at its physical value and varying the two degenerate light quark masses m_l towards the chiral limit $m_l \to 0$ around their pseudo-critical temperature T_{pc}. We analyzed especially the correlators for the pseudoscalar and scalar particle π and a_0 for lower-than-physical light quark masses $m_l < m_{l,\mathrm{phys.}}$. For the analysis at physical quark masses see Ref. [12,53]. Since these two particles are connected via the $U_A(1)$ symmetry, which is explicitly broken for any non-zero light quark mass (and at finite lattice spacing for staggered fermions, see sections 2.8 and 2.10 for details), we need to remove the explicit breaking of the $U_A(1)$ symmetry with an extrapolation to vanishing light quark masses $m_l \to 0$. For more details on $U_A(1)$ see section 2.10. Before this two other extrapolations need to be done: The thermodynamic limit and the continuum limit. For more details about the procedure see chapter 3.

For dynamical QCD as we use here, the generation of Markov chains are far more expensive than for quenched QCD. Therefore to achieve enough configurations and consequently better statistics, lattice sizes for dynamical QCD are kept smaller than for quenched QCD. One problem that arises here is that the temporal lattice extent N_τ is undersized for our analytical methods. For this and other reasons we calculate mesonic correlators along the spatial lattice extent N_s to extract their so-called screening masses. For more details on the staggered correlators see section 2.7.

We expect two limits for our calculations: For zero temperature, temporal mesonic correlators and spatial mesonic correlators should have the same mass values. For temperatures $T \to \infty$, the screening masses of mesonic correlators should go towards $2\pi T$, which is the result in the free case [60,61].

In section 4.1 we will describe more of our lattice setup. In section 4.2 we take a look at the lattice results to assess the quality of our correlators. In section 4.3 the results from our calculations after setting the scale will be shown; for information about the scale setting see sections 2.9 and 4.1. In section 4.4 we will show our fitting results for the thermodynamic limit following the procedure of section 3.2: The goal is to estimate the systematic effect of the thermodynamic limit to our largest lattice volumes N_s^3. In section 4.5 continuum limit fitting results using the results from section 4.4 by using the methods of section 3.3 will be shown: Here we want to estimate, similar to section 4.4, the systematic effect of different continuum limit extrapolations to our finest lattice, i.e. largest N_τ. Finally in section 4.6 some chiral limit extrapolations will be shown and the final results will be discussed.

4.1 Lattice setup

All following calculations of meson screening mass correlators were performed with the $N_f = 2+1$ HISQ action while the strange quark mass is kept at the physical value $m_s = m_{s,\text{phys.}}$ and the degenerate light quark masses consisting of up and down quark mass, m_u and m_d, are varied to lower-than-physical quark masses $m_l < m_{l,\text{phys.}}$. The tuning of the strange quark mass was done by matching to the mass of the fictious pseudoscalar meson m_{η_s} [62,63]. The mass ratio for physical light quark masses corresponds to $m_l/m_s = 1/27$, i.e. lower-than-physical light quark mass values have a smaller mass ratio. Here we used $m_l/m_s = 1/40$, $1/80$ and $1/160$, which correspond to pion masses of $m_\pi = 110$ MeV, $m_\pi = 80$ MeV and $m_\pi = 55$ MeV, respectively. The temperature range that we covered for these mass ratios lies between $T = 135$ MeV and $T = 170$ MeV. All configurations are seperated by at least 5 full trajectories starting from 200, all in molecular dynamics time units. The lattice sizes vary from $24^3 \times 8$ to $60^3 \times 12$ for $m_l/m_s = 1/40$, from $24^3 \times 6$ to $72^3 \times 12$ for $m_l/m_s = 1/80$ and for $m_l/m_s = 1/160$ we only had one lattice of size $56^3 \times 8$. Therefore a proper continuum extrapolation including a thermodynamic limit extrapolation with at least three volumes and lattice spacings is currently only possible for mass ratio $m_l/m_s = 1/80$, since for $m_l/m_s = 1/40$ we did not have the $N_\tau = 6$ analysis and for $m_l/m_s = 1/160$ neither the thermodynamic limit nor the continuum limit is possible right now. The statistics are in Tables 4.2 to 4.7. All temperatures T mentioned in the tables are in f_K-scale from Ref. [12].

We have set the scale for our configurations using the f_K-scale following Ref. [64]. To set the scale the Kaon decay constant $f_{K,\text{exp}} = \frac{156.1}{\sqrt{2}}$ MeV has been compared to the lattice observable af_K computed from two point correlation functions. This thesis however uses an updated version of this scale setting [12], which results in slight deviations to the original scale during

the creation of configurations [64]. We calculated all eight channels but analyzed mainly the $M1$ scalar and $M2$ pseudoscalar channels since they are related via the $U_A(1)$ symmetry in which we are mostly interested in this thesis. The temperature is calculated via [12]

$$T(\beta, N_\tau) = \frac{f_{K,\text{exp}}}{a f_K(\beta) N_\tau}, \tag{4.1}$$

where it is

$$a f_K(\beta) = \frac{c_{0,f_K} f(\beta) + 10 f(\beta)^3 c_{2,f_K}/\beta}{1 + 10 f(\beta)^2 d_{2,f_K}/\beta}, \tag{4.2}$$

where it is

$$f(\beta) = (10 b_0/\beta)^{-b_1/2b_0^2} \exp(-\beta/20 b_0), \tag{4.3}$$

where β is the inverse coupling and the remaining coefficients are in Tab. 4.1. The number of flavors N_f is in our case three.

b_0	b_1	c_{0,f_K}	c_{2,f_K}	d_{2,f_K}
$\frac{11-2N_f/3}{(4\pi)^2}$	$\frac{102-38N_f/3}{(4\pi)^4}$	7.49415	46049	3671

Table 4.1: Used coefficients for setting the temperature with the f_K scale. N_f is the number of flavors.

For all calculations of correlators we used the Bielefeld GPU code on the cluster of Piz Daint, at the Swiss National Supercomputing Centre (CSCS), Switzerland and the GPU based supercomputing cluster of Bielefeld University, Germany. We used only point sources, which we put randomly on the lattice, for all calculated correlators. For the fitting of the pseudoscalar correlators we used up to three states in the non-oscillating part while the states in the oscillating part are kept at zero since they are not present in this channel. For the fitting of the remaining correlators we used up to three states in both the non-oscillating and the oscillating part of the correlators. For the exact method for extracting the masses from the correlators see section 3.1.

In the next section 4.2 we have a look into the quality of our correlators.

β	T[MeV]	statistics $24^3 \times 8$	statistics $32^3 \times 8$	statistics $40^3 \times 8$
6.260	136.716	15240	4197	8420
6.285	140.32	15263	4281	8706
6.300	142.53	15385	4287	9220
6.315	144.77	15271	4283	9220
6.330	147.04	17091	4477	10820
6.354	150.76	17164	4497	10820
6.365	152.49	17134	4533	11220
6.390	156.50	18797	4563	11220
6.423	161.93	18888	3261	11220
6.445	165.66	20661	3481	11220

Table 4.2: Statistics for lattices of size $N_s^3 = 24^3, 32^3, 40^3$ with $N_\tau = 8$ at mass ratio $m_s/m_l = 40$. Temperature T is in f_K-scale from Ref. [12].

β	T[MeV]	statistics $42^3 \times 12$	statistics $60^3 \times 12$
6.600	129.45	6108	4304
6.640	134.80	3819	5338
6.680	140.36	4380	6140
6.712	144.94	4380	6700
6.754	151.15	4900	6696
6.794	157.27	5400	7570
6.825	162.17	5412	7566
6.850	166.21	5570	7561

Table 4.3: Statistics for lattices of size $N_s^3 = 42^3, 60^3$ with $N_\tau = 12$ at mass ratio $m_s/m_l = 40$. Temperature T is in f_K-scale from Ref. [12].

β	T[MeV]	statistics $24^3 \times 6$	statistics $32^3 \times 6$	statistics $48^3 \times 6$
6.025	142.73	4813	-	3206
6.038	144.67	4157	-	3392
6.050	146.48	3688	-	3414
6.062	148.32	3888	4775	4157
6.075	150.33	3941	-	405
6.090	152.70	3985	7648	4106
6.105	155.10	4194	-	4182
6.120	157.54	-	-	3679
6.125	158.36	4496	-	-
6.135	160.02	4541	3525	-
6.150	162.54	6640	4702	-

Table 4.4: Statistics for lattices of size $N_s^3 = 24^3, 32^3, 48^3$ with $N_\tau = 6$ at mass ratio $m_s/m_l = 80$. Temperature T is in f_K-scale from Ref. [12].

β	T[MeV]	statistics $32^3 \times 8$	statistics $40^3 \times 8$	statistics $56^3 \times 8$
6.285	140.32	15209	5620	5118
6.300	142.53	14124	5620	5117
6.315	144.77	17468	5620	5115
6.330	147.05	18694	5740	5064
6.354	150.76	20403	6480	5115
6.372	153.60	15060	6425	3118
6.390	156.50	23021	8196	5235
6.423	161.93	9620	8385	2815
6.445	165.66	9620	8581	2831

Table 4.5: Statistics for lattices of size $N_s^3 = 32^3, 40^3, 56^3$ with $N_\tau = 8$ at mass ratio $m_s/m_l = 80$. Temperature T is in f_K-scale from Ref. [12].

β	T[MeV]	statistics $48^3 \times 12$	statistics $60^3 \times 12$	statistics $72^3 \times 12$
6.600	129.45	3734	2763	-
6.640	134.80	6940	4094	3106
6.680	140.36	7190	4365	4100
6.712	144.94	7908	4357	3884
6.733	148.02	1273	902	3433
6.754	151.15	8246	4716	3356
6.794	157.27	-	3718	-
6.825	162.17	-	3847	-
6.850	166.21	-	4347	-

Table 4.6: Statistics for lattices of size $N_s^3 = 48^3, 60^3, 72^3$ with $N_\tau = 12$ at mass ratio $m_s/m_l = 80$. Temperature T is in f_K-scale from Ref. [12].

β	T[MeV]	statistics
6.285	140.32	3391
6.300	142.53	3402
6.315	144.77	3378
6.330	147.05	3400
6.354	150.76	3378
6.372	153.60	1721
6.390	156.50	4131
6.423	161.93	4845
6.445	165.66	5182

Table 4.7: Statistics for lattice of size $56^3 \times 8$ at mass ratio $m_s/m_l = 160$. Temperature T is in f_K-scale from Ref. [12].

4.2 Correlators

In this section we will have a look at the correlators before analyzing further. First we want to look at the complete correlator and their respective uncertainties. Next we want to have a look at the distribution of the correlator values for a given distance.

In Fig. 4.1 and in Fig. 4.2 we show example plots for all calculated meson channels. The uncertainties are calculated via standard error. The correlators of Fig. 4.1 seem to be smooth and the uncertainties are small. Therefore a good mass extraction is expected from the $M1$ and $M2$ channels.

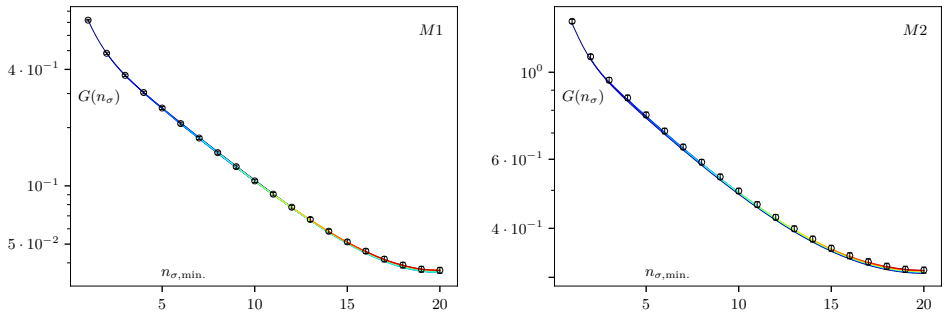

Figure 4.1: Example plots and best fits for the $M1$ scalar (left) and the $M2$ pseudoscalar channel (right). Both correlators G are calculated at lattice size $40^3 \times 8$, at $\beta = 6.354$, with quark content $\bar{u}d$ and for mass ratio $m_s/m_l = 80$. The corresponding temperature is $T = 150.76$ MeV [12]. The correlator for the $M1$ channel was multiplied by $(-1)^{n_\sigma}$ for better visibility.

The correlators of Fig. 4.2 on the other hand become very noisy towards the middle of the lattice with data points switching signs and having large uncertainties. Therefore we expected to get into some trouble if we extract masses from $M34$ and $M67$ channels, even though $M34$ and $M67$ have effectively increased statistics due to averaging of the $M3$, $M4$ and $M6$, $M7$ correlators, respectively.

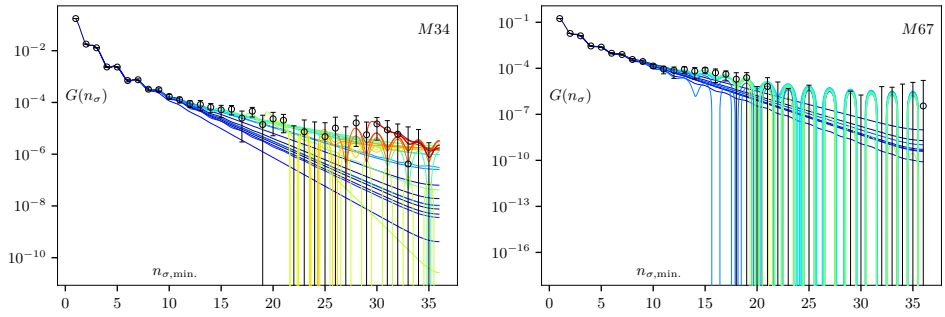

Figure 4.2: Example plots and best fits for the $M34$ axial vector (left) and the $M67$ vector channel (right). Both correlators G are calculated at lattice size $72^3 \times 12$, at $\beta = 6.712$, with quark content $\bar{u}d$ and for mass ratio $m_s/m_l = 80$. The corresponding temperature is $T = 144.94$ MeV [12]. The correlator for the $M34$ channel was multiplied by $(-1)^{n_\sigma}$ for better visibility.

In Fig. 4.3 and Fig. 4.4 we show some histograms of all channels at a distance equal to half the lattice extent. In Fig. 4.3 we see the $M3$ and $M6$ channel histograms. The distributions of the correlator values look like a normal distribution and seem to be centered around 0 in both cases.

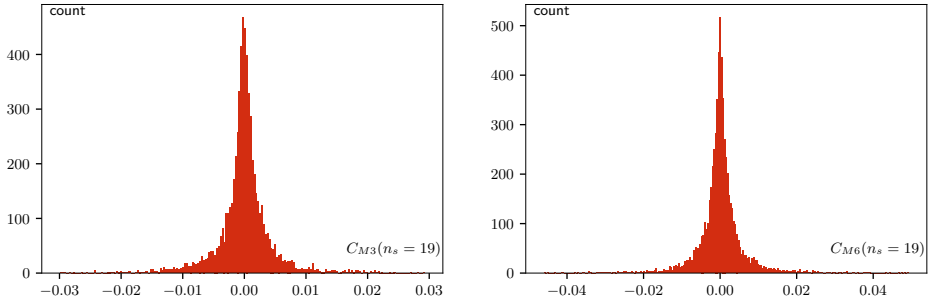

Figure 4.3: Histograms of $M3$ (left) and $M6$ (right) channel. Both correlators are calculated at lattice size $40^3 \times 8$, at $\beta = 6.354$, with quark content $\bar{u}d$ and for mass ratio $m_s/m_l = 80$. The corresponding temperature is $T = 150.76$ MeV [12].

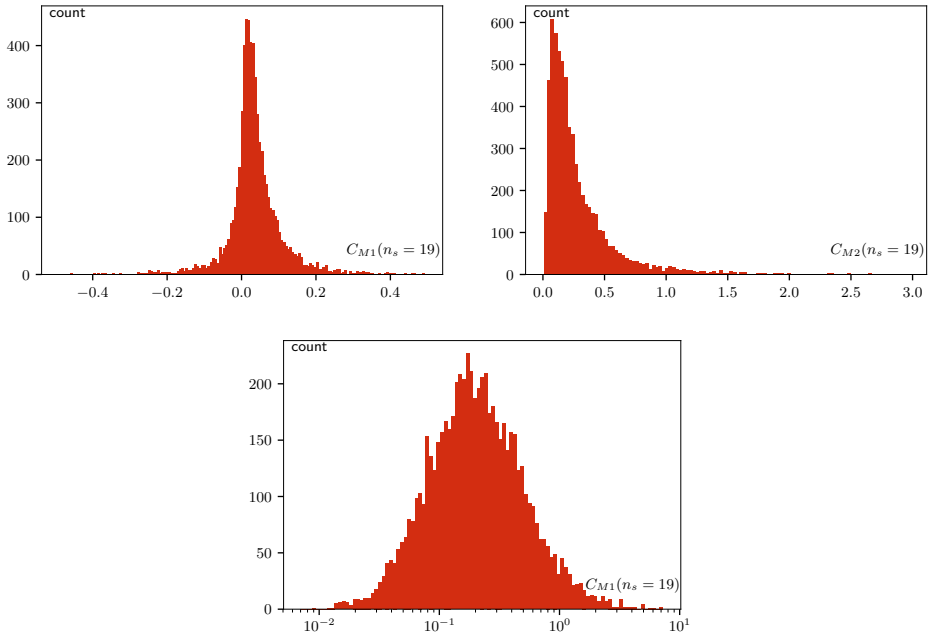

Figure 4.4: Histograms of $M1$ (left) and $M2$ (right, bottom) channel. Both correlators are calculated at lattice size $40^3 \times 8$, at $\beta = 6.354$, with quark content $\bar{u}d$ and for mass ratio $m_s/m_l = 80$. The corresponding temperature is $T = 150.76$ MeV [12]. The x-axis of the bottom $M2$ channel histogram is logarithmic.

In Fig. 4.4 we see the $M1$ and $M2$ channel histograms. The distribution of the correlator values for $M1$ seems to be shifted towards positive numbers

and looks like a skew normal distribution. It would be a right skewed normal distribution in that case. The $M2$ channel on the other side has a long tail distribution. In the bottom plot of Fig. 4.4 the $M2$ channel is plotted with a logarithmic x-axis. In this depiction the $M2$ channel looks like a normal distribution. Therefore the distribution of the $M2$ channel would be lognormal. Similar observations were already made and discussed in Ref. [65].

In the next section 4.3 we will show our results for the screening masses and susceptibilities before any extrapolation.

4.3 Calculations of screening masses and susceptibilities

4.3.1 Screening masses

In Fig. 4.5 we show the screening mass results from our calculations after setting the scale. The screening masses for mass ratio $m_s/m_l = 27$ were taken from a previous study of screening masses and their susceptibilities at physical quark masses [12]. It seems that the pseudoscalar mass m_π has lower volume dependence compared to the scalar mass m_{a_0}. In general, towards higher temperatures m_π rises on a convex curve while m_{a_0} first drops down as it gets closer to the phase transition temperature until it rises again. The gap between the scalar mass m_{a_0} and m_π decreases for increasing temperatures and m_{a_0} stays above m_π at all temperatures. Note that the calculated scalar mass for temperatures below the phase transition temperature T_{pc} is not the mass of a_0 but of an artificial and unphysical decay channel to particles of a combined mass of $2m_\pi$. This is a well-known staggered artifact [24–26]. This artifact results from the broken taste symmetry at finite lattice spacing [24], which gets restored in the continuum limit. This decay is forbidden in nature due to parity, isospin and G-parity conservation. For staggered fermions at finite lattice spacing different tastes contribute to the intermediate states of loop diagrams, which leads to this decay. If we could take the continuum limit on the correlator level, we could extract the correct m_{a_0} [24–26]. Since we first extract the screening mass and then take the continuum limit, we obtain this unphysical decay of the scalar to a combined mass of $2m_\pi$. Above T_{pc} this artifact is expected to not be present and it approaches the true screening mass m_{a_0} as the extracted ground state mass since m_{a_0} becomes more and more degenerate with m_π at higher temperatures, which implies that $U_A(1)$ symmetry may get effectively restored. Thus the reduced phase space forbids a decay from m_{a_0} into $2m_\pi$ due to energy conservation. This also leads to some large uncertainties for m_{a_0} below and around the phase transition temperature, which then leads to larger volume and cut-off effects. The continuum pseudo-critical temperatures we

used are $T_{\rm pc} = 156.5(15)$ MeV for $m_s/m_l = 27$ [66], $T_{\rm pc} = 151.5(6)$ MeV for $m_s/m_l = 40$ and $T_{\rm pc} = 146.5(10)$ MeV for $m_s/m_l = 80$ [40]. For $m_s/m_l = 160$ we did not have a continuum phase transition temperature yet. On the other hand we only had one lattice at $m_s/m_l = 160$ and therefore could not proceed there anyway. The $T_{\rm pc}$ in the chiral limit however is the continuum critical temperature $T_c = 132^{+3}_{-6}$ MeV corresponding to $m_s/m_l = \infty$ [8]. Note that for individual lattices with N_τ and N_s the $T_{\rm pc}$ varies since the mentioned transition temperatures are for values after the thermodynamic and continuum limit.

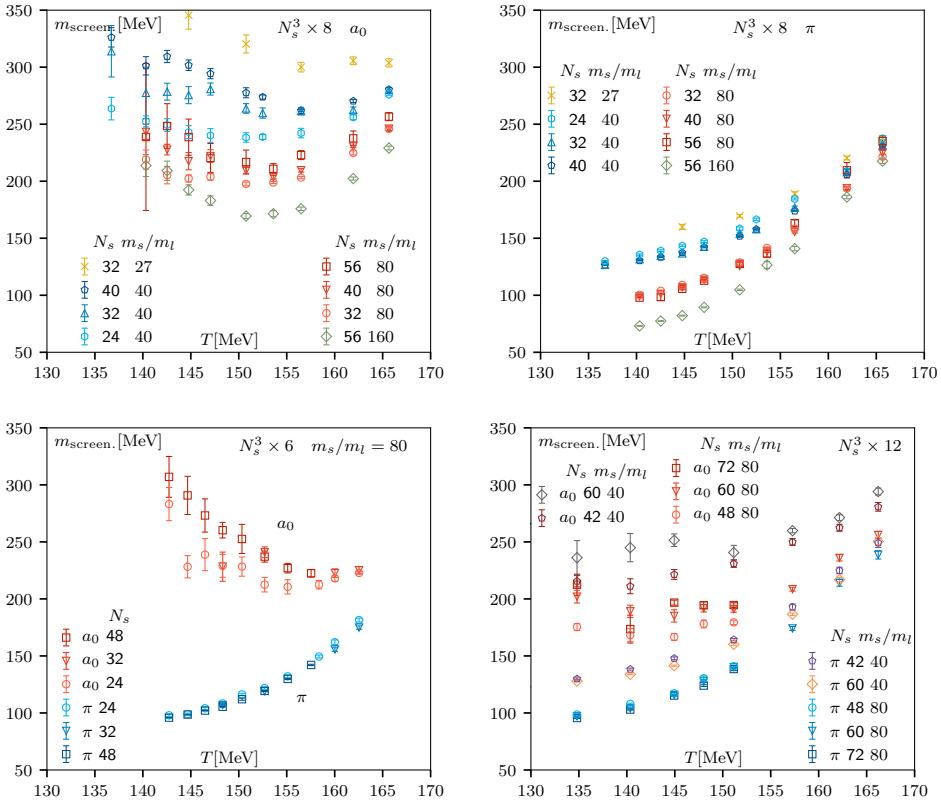

Figure 4.5: Extracted meson screening mass results for a_0 and π as function of temperature. Top left: $N_\tau = 8$, a_0. Top right: $N_\tau = 8$, π. Bottom left: $N_\tau = 6$ for mass ratio $m_s/m_l = 80$. Bottom right: $N_\tau = 12$ for mass ratio $m_s/m_l = 80$ and $m_s/m_l = 40$.

Before we can draw any meaningful conclusions regarding a possible effective $U_A(1)$ restoration we need to remove finite volume and cut-off effects. We will cover that in sections 4.4 and 4.5. But first we want to have a look at the susceptibilities in the next subsection 4.3.2.

4.3.2 Susceptibilities

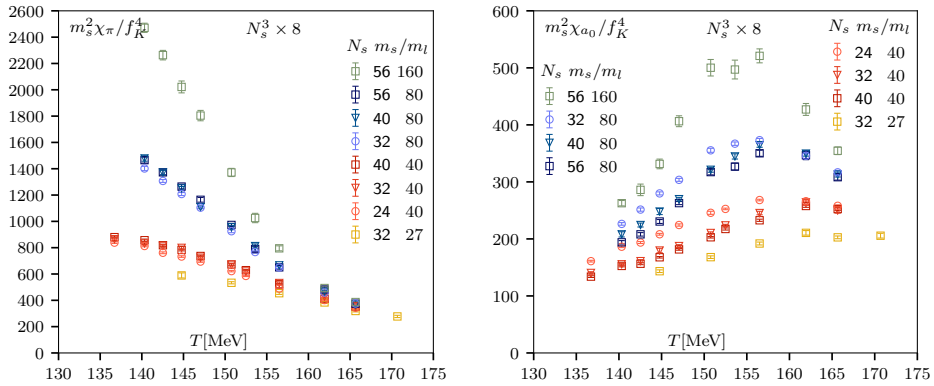

Figure 4.6: Individual susceptibility plots for χ_π (left) and χ_{a_0} (right) as function of temperature for $N_\tau = 8$ for different mass ratios m_s/m_l.

Circumventing and estimating the gravity of the issue in the scalar channel mass that we encountered in subsection 4.3.1 we want to have a look at the susceptibilities of π and a_0. This is a continuation of an earlier work from Ref. [67]. The susceptibilities χ_π and χ_{a_0} are calculated according to Eq. 3.1. The uncertainties are calculated via jackknife resampling. The values for mass ratio $m_s/m_l = 27$ were taken from a previous study of screening masses and their susceptibilities at physical quark masses [12]. In Fig. 4.6 we show the individual susceptibilities of π and a_0; the screening masses based on the same correlators were discussed in the last subsection 4.3.1. By multiplying the susceptibilities by m_s^2 and taking the difference of them, we get a additively and multiplicatively renormalized observable out of these susceptibilities, which is needed for the continuum extrapolation. We additionally divided the susceptibilities by f_K^4 to make it dimensionless. In the left plot of Fig. 4.6 we see that χ_π rises for increasing mass ratios m_s/m_l below and around their T_{pc}, that is due to Eq. 3.11, where χ_π diverges below T_{pc} in the chiral limit $m_l \to 0$. In the right plot of Fig. 4.6 we see that χ_{a_0} has low values below T_{pc} compared to χ_π and rise around T_{pc} while rising stronger for increasing mass ratios m_s/m_l. Above T_{pc} the values for the different mass ratios m_s/m_l apparently approach each other towards increasing temperatures, that seems to be true for each individual susceptibility as well as for the difference; see Fig. 4.7 for the difference. That approach means that χ_π and χ_{a_0} would both be independent of the mass ratio m_s/m_l at high temperatures. While the volume dependence for χ_π and χ_{a_0} seems to be comparable to the volume dependence of their respective screening masses m_π and m_{a_0}, the systematic uncertainties for χ_{a_0} seems to be rather small compared to

the ones for the scalar screening mass at temperatures below and around T_{pc}. This could be explained by the aforementioned unphysical decay channel of the scalar screening mass below and around T_{pc} at finite lattice spacing (see subsection 4.3.1), which leads to stronger systematic uncertainties due to the mass extraction process. For the corresponding susceptibility χ_{a_0} all information from the correlator is directly taken into account in contrast to extracting only the ground state mass. That would lead to less systematic uncertainties for χ_{a_0} in comparison to the extracted scalar screening masses.

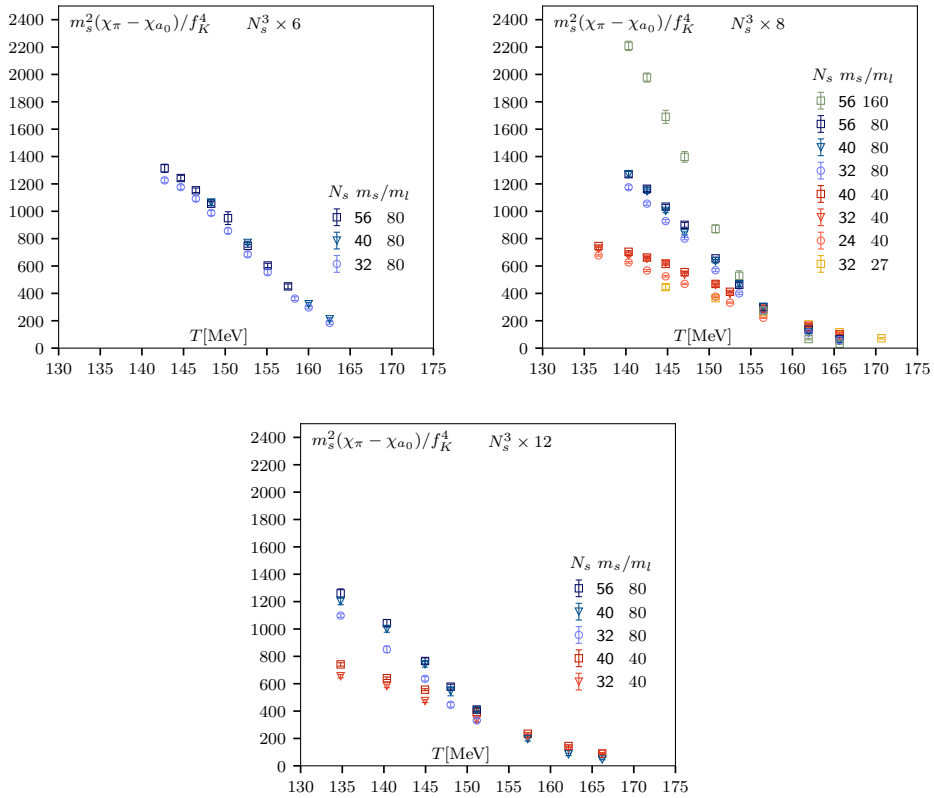

Figure 4.7: Susceptiblity difference of pseudoscalar χ_π and scalar χ_{a_0} as function of temperature for different mass ratios m_s/m_l. Top left: $N_\tau = 6$. Top right: $N_\tau = 8$. Bottom: $N_\tau = 12$.

We will now take a look into the difference of those susceptibilities, because their difference is a measure for the $U_A(1)$ symmetry breaking. We see in Fig. 4.7 that for increasing temperature $\chi_\pi - \chi_{a_0}$ approaches 0, which implies that the $U_A(1)$ symmetry may be effectively restored for higher temperatures. In the top right plot of Fig. 4.7 we see that for increasing mass ratios m_s/m_l the curve steepens, values increase below and around T_{pc} and

decrease above T_{pc} for increasing m_s/m_l. That is because χ_π is dominating (diverging in the chiral limit) below T_{pc}.

Since susceptibilities of screening correlators seem to have smaller uncertainties due to the lack of additional analysis, we will now have a quick look into the susceptibility difference for the vector and axial vector channels, which is shown in Fig. 4.8. The degeneracy of those correlators is related to the chiral symmetry restoration; to be precise the restoration of $SU_A(2)$. Compared to χ_π and χ_{a_0} this quantity has, as we already expected on the correlator level, sometimes large uncertainties and are not on a stable path as for χ_π and χ_{a_0}, thus we did not analyze them until further improvements. As mentioned in Ref. [12, 53], corner wall sources could help in the case of axial vector and vector correlators. Unfortunately corner wall sources are also more expensive compared to point sources. As also seen in these studies [12, 53] the uncertainties would still be larger compared to the scalar and pseudoscalar channels. For further verification an investigation of axial vector and vector channels with corner wall sources could be done beyond the scope of this thesis.

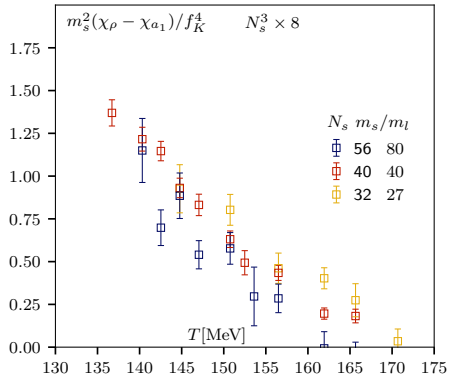

Figure 4.8: Susceptiblity difference of vector χ_ρ and axial vector χ_{a_1} as function of temperature for $N_\tau = 8$ for different mass ratios m_s/m_l.

Before we can draw any meaningful conclusions regarding a possible effective $U_A(1)$ restoration we need to remove finite volume and cut-off effects. We will cover that in sections 4.4 and 4.5. In the next subsection 4.3.3 we want to have a look at another project, which takes a look into the content of the screening correlators; whether they still consist of a meson state or if the individual quark states are visible.

4.3.3 Periodic temporal boundary condition

In nature, quarks are fermions and the meson screening masses should go towards $2\pi T$ in the free case at $T \to \infty$ [60, 61]. Bosonic quarks however would go towards the total mass of their constituents m_{tot} in the $T \to \infty$ limit, which results in a constant. But at low temperatures both mesons should give the same mass because the bound state is bosonic in both cases. The switch from fermionic to bosonic valence quarks is achieved by switching the boundary conditions in the temporal direction from anti-periodic to periodic. This allows us to observe at which temperature the bosonic meson state transitions into a superposition of its individual quark states and the meson state if we use the same configurations; in this case they contain fermionic sea quarks. As the last project of this thesis, next to the anomalous part of $U_A(1)$, we want to figure out the temperature where this transition happens.

In Fig. 4.9 we present comparison plots for $N_\tau = 6$ and $N_\tau = 8$ for a mass ratio of $m_s/m_l = 80$ between ground state meson screening masses with fermionic valence quarks and ground state meson screening masses with bosonic valence quarks. Filled points are the bosonic quark results and open points are the fermionic quark results. For both calculations the same configurations, i.e. fermionic sea quarks, are used.

In the case of a_0 (red) we can not make a clear distinction between both cases because of the lack of precision. One reason for the lack of precision could be the aforementioned problem in the scalar channel for temperatures around and below T_{pc}; see subsection 4.3.1 for details. For the π (blue) a clear separation can be seen. From these two plots the splitting temperature T_{split}, where the bosonic meson transitions into a superposition of meson and quark states, can not be determined since the splitting seems to happen below the calculated temperature range. Therefore we would expect a splitting temperature below 140 MeV for mass ratio $m_s/m_l = 80$. Together with former studies [68] we predict that this splitting temperature will decrease even more in the chiral limit because for lower quark masses they seemed to split earlier. However we can not make a clear statement before the thermodynamic limit and continuum limit extrapolations are done. Considering that it is very probable that the temperature range is too high to analyze the splitting behavior, we stopped this project here until we have masses at even lower temperatures.

In the next section 4.4 we will continue with the thermodynamic limit extrapolation for the screening masses and susceptibilities of the π and a_0 channel.

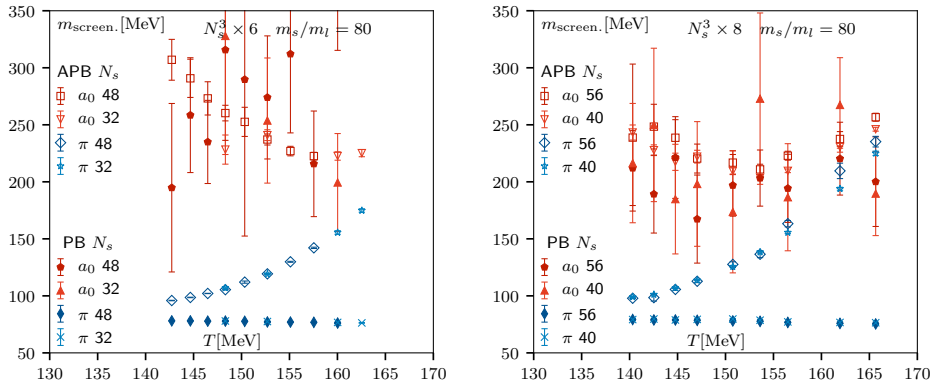

Figure 4.9: Comparison plot of physical screening masses with fermionic valence quarks using Anti-Periodic Boundary condition (APB, open points) and unphysical screening masses with bosonic valence quarks using Periodic Boundary condition (PB, filled points) in temporal direction as function of temperature at mass ratio $m_s/m_l = 80$ for π (blue) and a_0 (red). Left: $N_\tau = 6$. Right: $N_\tau = 8$.

4.4 Thermodynamic limit

Through the thermodynamic limit extrapolations we want to remove finite volume effects. To perform a proper thermodynamic limit for screening masses and their susceptibilities we need at least three values from different N_s for fixed N_τ at fixed mass ratio m_s/m_l and fixed temperature T. Getting bootstrap samples for screening masses is expensive because for every sample we would need to perform the whole analysis. For the procedure see section 3.2. Instead we randomly pick values x within the interval of the mean values μ and their standard error σ, i.e. $x \in [\mu - \sigma, \mu + \sigma]$. We use these random values x as new mean values $\mu_{\text{new}} = x$ with the same standard error σ to perform fits. After performing several fits, we calculated the mean values and standard error of all those fit functions. This procedure results in uncertainty bands, which we extrapolate to $N_s \to \infty$. The mean values and the standard errors of these uncertainty bands at $N_s \to \infty$ are then the infinite-volume-extrapolated values, which we could use for continuum and chiral limit extrapolations. In our case we used 10000 random values for the thermodynamic limit extrapolations to account for any randomness regarding the screening masses as well as the susceptibilities.

4.4.1 Screening masses

To remove the finite volume effects of the screening masses we used Eq. 3.3 for the thermodynamic limit extrapolation with c being the shared parameter

for π and a_0 at the same mass ratio m_s/m_l, temperature T and N_τ. See section 3.2 for details.

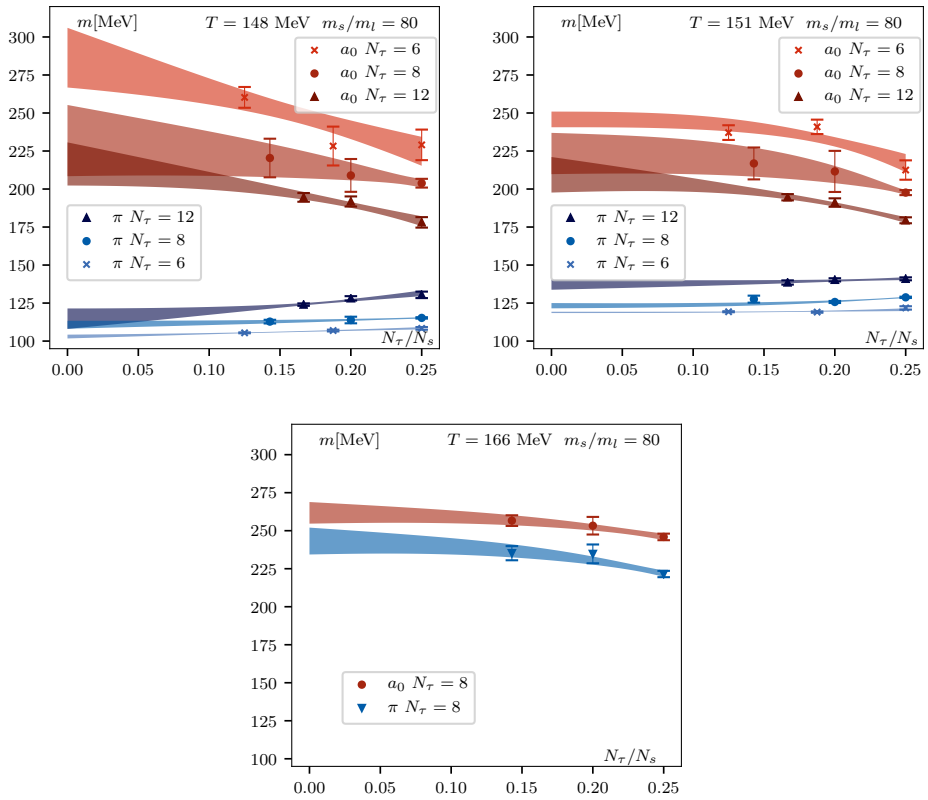

Figure 4.10: Thermodynamic limit extrapolations of scalar (S, red) and pseudoscalar (PS, blue) screening masses at $T \approx 148$ MeV (top left), $T \approx 151$ MeV (top right) and $T \approx 166$ MeV (bottom) for mass ratio $m_s/m_l = 80$.

Fig. 4.10 shows thermodynamic limit extrapolations at different temperatures for mass ratio $m_s/m_l = 80$. The uncertainties of m_π are very small in comparison to the uncertainties of m_{a_0} around the transition temperature T_{pc}, see Fig. 4.10 top plots. These larger volume effects of m_{a_0} also result from the large uncertainty from the extraction process; see section 4.3.1 for an explanation. Because of this, the fitting parameter c effectively gets determined by the m_π data around these temperatures. For higher temperatures even the uncertainty of m_{a_0} becomes small, see Fig. 4.10 bottom plot.

Note that the volume dependence seems to decrease with increasing temperature. Note also that most data points of the largest volumes agree within the 68% confidence interval, and all data points fall within the 95% confidence interval using the extrapolated value. The parameter c from our fits

are summarized in Tab. 4.8.

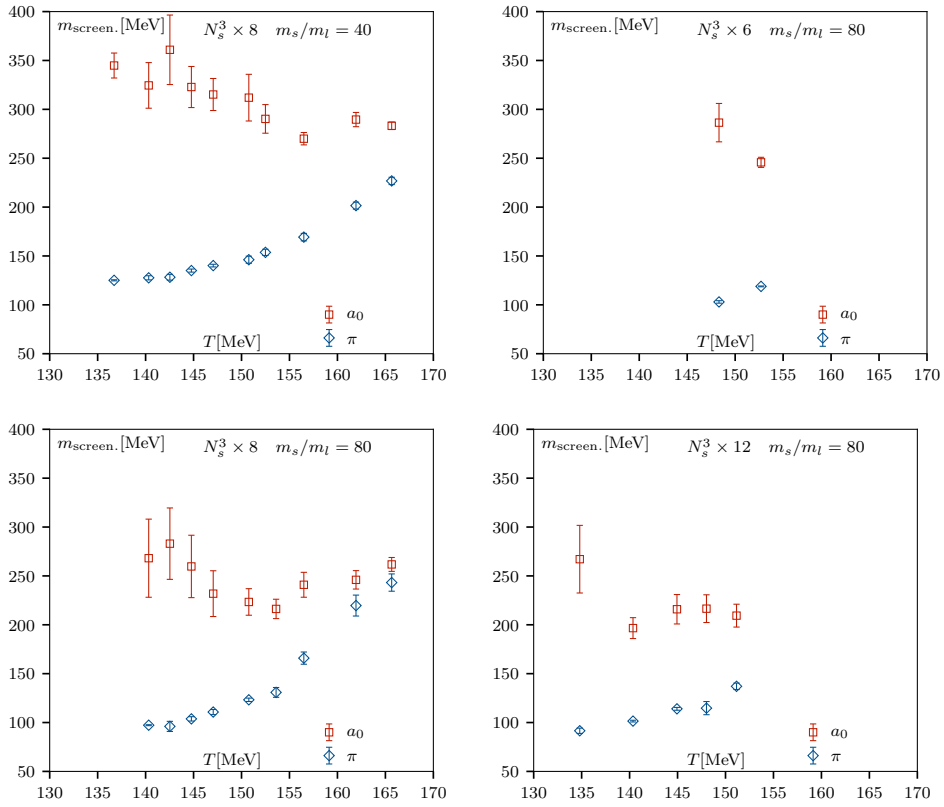

Figure 4.11: Infinite-volume-extrapolated masses of π (blue) and a_0 (red) as function of temperature. Top left: $N_\tau = 8$ for mass ratio $m_s/m_l = 40$. Top right: $N_\tau = 6$ for mass ratio $m_s/m_l = 80$. Bottom left: $N_\tau = 8$ for mass ratio $m_s/m_l = 80$. Bottom right: $N_\tau = 12$ for mass ratio $m_s/m_l = 80$.

Because different N_τ seem to experience slightly different volume effects, we want to investigate that even further. In the next step continuum extrapolations will take place, see section 4.5 for that. In this step we will check how much of an effect the thermodynamic limit has on the continuum limit. We will, among other things, compare continuum-extrapolated masses using infinite-volume-extrapolated masses to continuum-extrapolated masses using just our largest volumes. We want to quantify in that step any systematic uncertainties coming from the thermodynamic limit, which might lead to even larger uncertainties and due to their slightly different volume effects for different N_τ to a different extrapolation value for the continuum limit extrapolations. After we quantified also the systematic uncertainties from the continuum limit itself, we tackle the chiral limit extrapolation and try to

answer the main question of this thesis regarding a possible effective $U_A(1)$ restoration at the critical temperature T_c. We will cover the continuum limit in section 4.5.

In Fig. 4.11 we show the infinite-volume-extrapolated screening masses as a function of T. Note that for some N_τ and mass ratios m_s/m_l we did not have at least three different volumes for every temperature. Therefore we could not perform thermodynamic limit extrapolations for them. In fact we can only perform the pointwise continuum limit with infinite-volume-extrapolated masses for two different temperatures. Pointwise continuum extrapolation means that we take individual data points at different N_τ at similar temperature ($\approx$ 0-2 MeV) and treat them as if they had the exact same temperature and perform a continuum limit extrapolation. More on that in section 4.5.

In Tab. 4.9 and Tab. 4.10 we show the masses after the extrapolation and the masses from the largest N_s and their respective uncertainties. Assuming that the masses after the thermodynamic limit are the correct one, we calculated additionally the systematic uncertainty for the mean value that would result from skipping this step. From the change in the mean value it is apparent that for the lower temperature $T \approx 148$ MeV the change is stronger for a_0 as can already be seen in Fig. 4.10. Overall the change in mean value is stronger for a_0 compared to π. A summary of these results is that the finite volume effects become smaller for higher temperatures above T_{pc} and the corrections are rather small since they all agree with the largest volumes within the 95% confidence interval while both sets, extrapolated and largest volume masses, have uncertainties of less than 10%. We will proceed with the continuum limit in section 4.5.

In the next subsection 4.4.2 we will cover the thermodynamic limit extrapolations for the susceptibilities.

T[MeV]	$c_{N_\tau=6}$	$\Delta c_{N_\tau=6}$	$c_{N_\tau=8}$	$\Delta c_{N_\tau=8}$	$c_{N_\tau=12}$	$\Delta c_{N_\tau=12}$
148	1.34	0.67	1.91	0.97	1.83	0.92
151	2.99	0.15	2.90	0.40	2.30	0.90
166	-	-	2.59	0.76	-	-

Table 4.8: Fit parameter c from thermodynamic limit extrapolation of screening masses. The parameter c is identical to the c in Eq. 3.3.

T[MeV]	N_τ	$m_{a_0,\text{th.}}$[MeV]	$m_{a_0,\text{no th.}}$[MeV]	systematic uncertainty mean %
148	6	286.39(1963)	260.27 (684)	9.12
148	8	231.85(2342)	220.41(1269)	4.94
148	12	216.49(1419)	194.50 (287)	10.16
151	6	245.78 (516)	237.11 (483)	3.53
151	8	223.36(1358)	216.83(1049)	2.92
151	12	209.36(1169)	194.59 (207)	7.05

Table 4.9: Comparison of m_{a_0} after thermodynamic limit extrapolations $m_{a_0,\text{th.}}$ and the masses from the largest volume $m_{\text{a}_0,\text{no th.}}$. The systematic uncertainty of the mean value is calculated via $\frac{|m_{a_0,\text{th.}} - m_{a_0,\text{no th.}}|}{m_{a_0,\text{th.}}}$ using only the mean values.

T[MeV]	N_τ	$m_{\pi,\text{th.}}$[MeV]	$m_{\pi,\text{no th.}}$[MeV]	systematic uncertainty mean %
148	6	102.97(126)	105.42 (30)	2.38
148	8	110.73(261)	112.80(121)	1.87
148	12	114.73(673)	123.98 (81)	8.06
151	6	118.86 (43)	119.30 (34)	0.37
151	8	123.26(174)	127.57(230)	3.50
151	12	137.06(330)	138.53(140)	1.07

Table 4.10: Same as Tab. 4.9 but for m_π.

4.4.2 Susceptibilities

Coming back to the susceptibilities before we proceed to the continuum limit, we also want to remove the finite volume effects of our susceptibilities and compare them to the screening masses. For the fitting procedure we used the same strategy as for the screening masses in section 4.4.1. Toward the thermodynamic limit we made an ansatz for the susceptibilities according to Eq. 3.4. In Fig. 4.12 we show the thermodynamic limit for the susceptibility difference of χ_π and χ_{a_0} at mass ratio $m_s/m_l = 80$.

The ansatz seems to describe the data quite well. In contrast to the screening masses all the largest volume values agree with the extrapolated values already within the 68% confidence interval. In Fig. 4.13 we show a comparison of $(\chi_\pi - \chi_{a_0})$ available for different volumes to the infinite-volume-extrapolated results for various mass ratios m_s/m_l and N_τ.

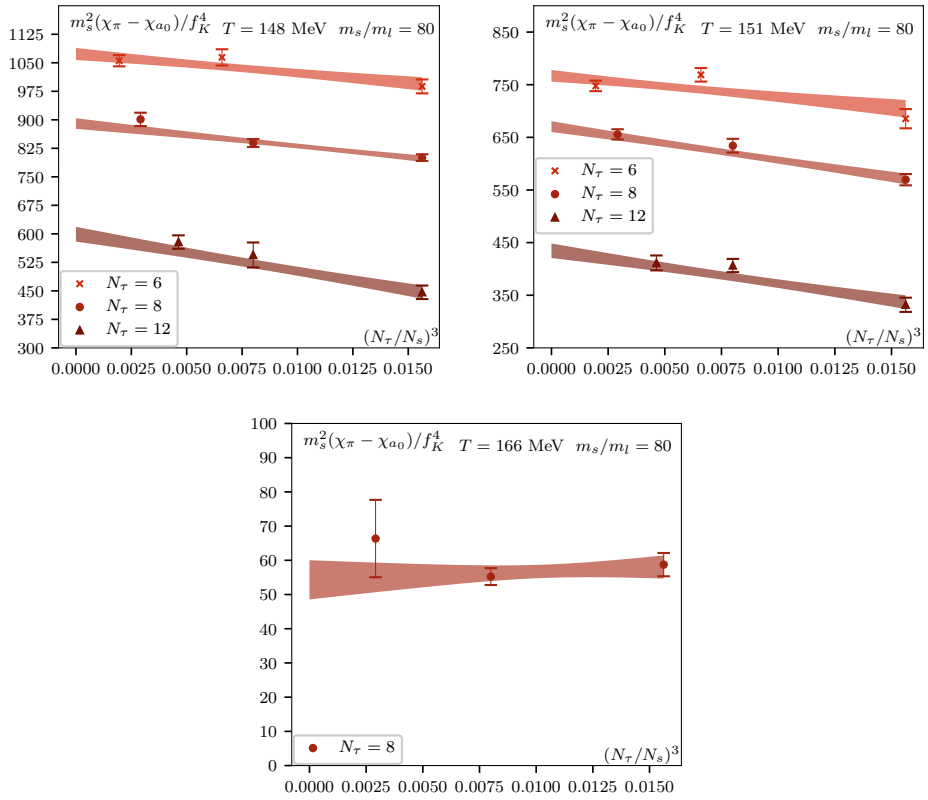

Figure 4.12: Thermodynamic limit extrapolations of susceptibility observable at $T \approx 148$ MeV (top left), $T \approx 151$ MeV (top right) and $T \approx 166$ MeV (bottom) for mass ratio $m_s/m_l = 80$.

T[MeV]	N_τ	$X_{\text{thermo.}}$	$X_{\text{no thermo.}}$	systematic uncertainty mean %
148	6	1073.16(1594)	1055.42(1475)	1.65
148	8	890.05(1400)	901.07(1760)	1.24
148	12	599.02(1945)	578.37(1770)	3.45
151	6	766.90(1107)	747.72 (998)	2.50
151	8	670.35(1030)	655.67 (967)	2.19
151	12	434.48(1384)	411.39(1418)	5.31

Table 4.11: Comparison of our observable $X = m_s^2(\chi_\pi - \chi_{a_0})/f_K^4$ after thermodynamic limit extrapolations $X_{\text{thermo.}}$ and values of the largest volumes $X_{\text{no thermo.}}$. The systematic uncertainty of the mean value is calculated via $\frac{|X_{\text{thermo.}} - X_{\text{no thermo.}}|}{X_{\text{thermo.}}}$ using only the mean values.

From Fig. 4.13 it seems that the volume dependence is stronger for temperatures below T_{pc} compared to higher temperatures and also for increasing N_τ. In Tab. 4.11 we show the values after the extrapolation and the values from the largest lattice extent N_s with their respective uncertainties. Assuming that the susceptibilities in the thermodynamic limit are the correct one, we calculated additionally the systematic uncertainty for the mean value, which would result from skipping this step. The change in the mean value seems to be the largest for $N_\tau = 12$ and overall rather small.

We will now proceed with the continuum limit in the next section 4.5.

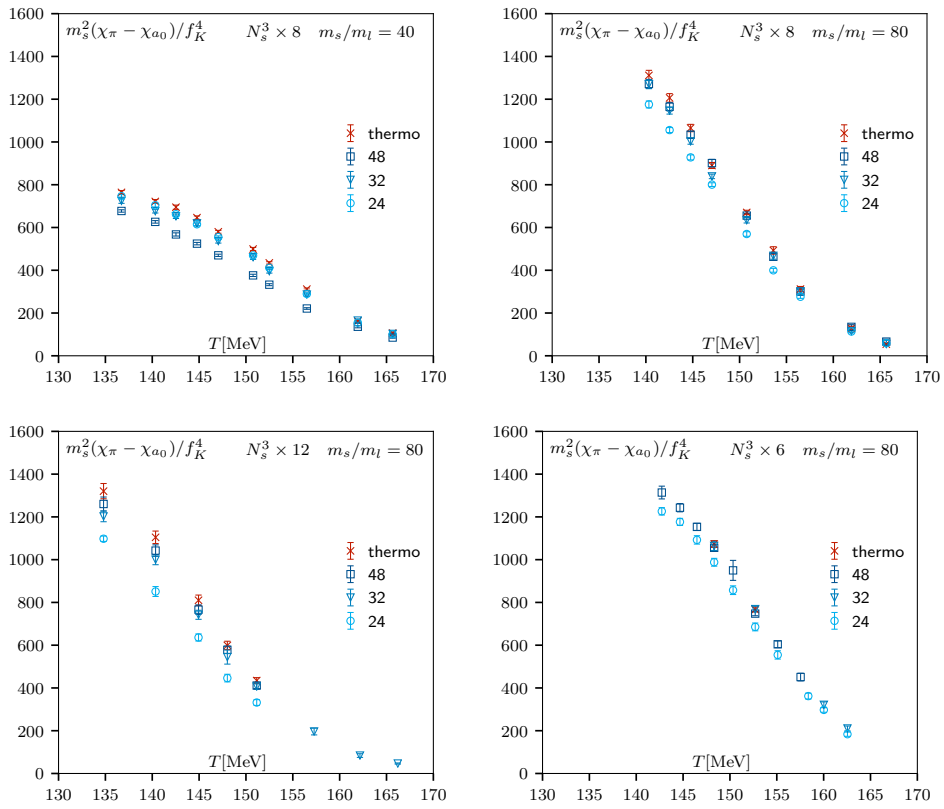

Figure 4.13: Comparison plot of original data (light to dark blue) to their infinite volume values (red) for the susceptibility difference of χ_π and χ_{a_0} as function of temperature. The ansatz used here is Eq. 3.4. Top left: $N_\tau = 8$, $m_s/m_l = 40$. Top right: $N_\tau = 8$, $m_s/m_l = 80$. Bottom left: $N_\tau = 12$, $m_s/m_l = 80$. Bottom right: $N_\tau = 6$, $m_s/m_l = 80$.

4.5 Continuum limit

In a second step after the thermodynamic limit extrapolations, which removed finite volume effects, we proceed with continuum limit extrapolations, which remove cut-off effects by extrapolating the lattice spacing to $a \to 0$, i.e. going back to continuum physics. In this section we also want to estimate the importance of thermodynamic limit extrapolations propagating to continuum-extrapolated values. For this we will compare extrapolated values after the thermodynamic and continuum limit with extrapolated values after the continuum limit using only largest volumes. We also want to quantify the corrections of the continuum extrapolations and compare them to the original data points without any extrapolations. We are especially interested in the area around T_{pc} where we can perform pointwise continuum extrapolations. We want to know the relative effect on masses and susceptiblities from continuum limit extrapolations around the transition temperature to make more accurate statements for values after chiral limit extrapolations. Pointwise continuum extrapolation means that we take individual data points at different N_τ at similar temperature ($\approx$ 0-2 MeV) and treat them as if they had the exact same temperature and perform a continuum extrapolation.

Because the temperatures for the pointwise continuum extrapolations do not align perfectly we want to address that. Therefore we want to use temperature ranges afterwards, which we get by interpolating between the temperatures using cubic splines with node positions determined by the density of data points. These temperature interpolations for $N_\tau = 6, 8$ and 12 are used in a joint continuum extrapolation with spline coefficients as a function of $1/N_\tau^2$. More details about that procedure can be found in Ref. [12, 53]. We use the same strategy as for the thermodynamic limit (section 4.4) to perform the pointwise $N_\tau \to \infty$ extrapolations. We took 1000 random values for the pointwise continuum limit extrapolations and a sample size of 1000 for the continuum limit extrapolations with temperature interpolation. Since we first assume that our fitting function is linear in $1/N_\tau^2$ as in Eq. 3.7 and Eq. 3.8, we need values for at least two different N_τ but better three. For details see section 3.3.

In the next subsection 4.5.1 we apply all these strategies to our screening masses.

4.5.1 Screening masses

In this subsection we want to extrapolate the screening masses back to continuum physics via continuum limit extrapolations to remove cut-off effects from our specific choice of discretization. To perform a proper continuum extrapolation for screening masses we need masses of different N_τ at fixed mass ratio m_s/m_l and fixed temperature T. We start with the masses after the

thermodynamic limit from subsection 4.4.1. In Fig. 4.14 we show the thermodynamic limit results plotted against $1/N_\tau^2$ for the screening masses for the two possible temperatures for pointwise continuum extrapolations. For details of what pointwise continuum extrapolation means, see the beginning of section 4.5.

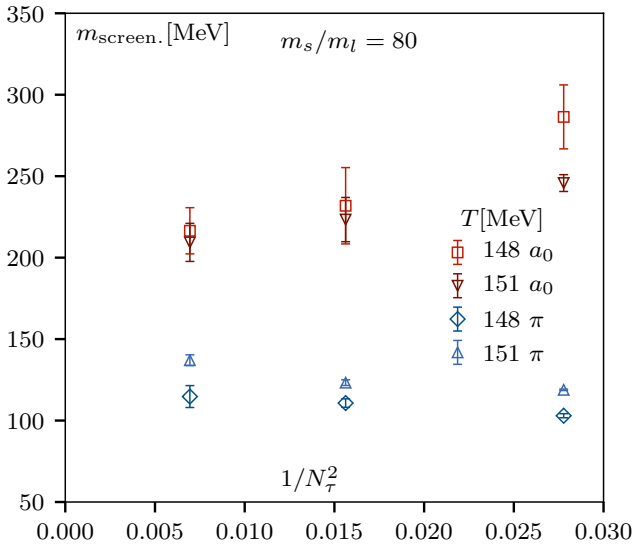

Figure 4.14: Infinite-volume-extrapolated masses for mass ratio $m_s/m_l = 80$ plotted against $1/N_\tau^2$. A linear dependence is expected.

From Fig. 4.14 it seems that the infinite-volume-extrapolated masses behave as expected. We therefore will proceed with a fitting function linear in $1/N_\tau^2$.

As a benchmark we compare masses after the thermodynamic limit with masses from the largest volumes and perform continuum limit extrapolations from there, because the correction seemed small (see subsection 4.4.1). In Fig. 4.15 we show both extrapolations.

From Fig. 4.15 we see that the cut-off effect compared to the volume effect is of the same magnitude. It seems that a thermodynamic limit extrapolation beforehand widens the mass gap between a_0 and π in the continuum limit and leads to larger uncertainties. Skipping the thermodynamic limit extrapolation might therefore conclude an earlier effective $U_A(1)$ restoration temperature, however the current accuracy is not statistically significant to be certain about that conclusion. The results of our calculations are given in Tab. 4.12. Since the two continuum extrapolation types give results, which agree within the 95% confidence interval, we use the screening masses from the largest available volumes for further analysis.

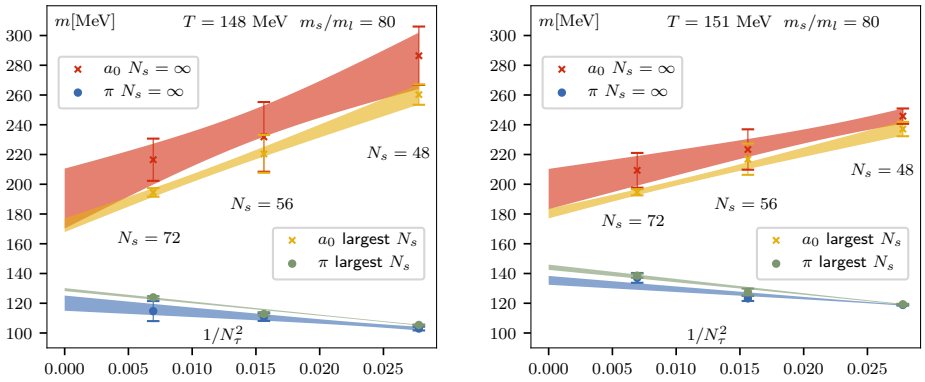

Figure 4.15: Comparison of pointwise continuum limit extrapolations for screening masses m_π (blue, light grey) and m_{a_0} (red, yellow) at $m_s/m_l = 80$. Left: Extrapolations using masses after the thermodynamic limit ($N_s = \infty$, red and blue) and from largest volumes ($N_s = 48, 56, 72$, yellow and light grey) at $T \approx 148$ MeV. Right: Same as left but at $T \approx 151$ MeV.

T[MeV]	$m_{a_0,\text{cont.}}$[MeV]	$m_{a_0,\text{cont.,no th.}}$[MeV]	systematic uncertainty mean %
148	190.37(2015)	172.43 (464)	9.42
151	196.77(1355)	180.29 (322)	8.38
T[MeV]	$m_{\pi,\text{cont.}}$[MeV]	$m_{\pi,\text{cont.,no th.}}$[MeV]	systematic uncertainty mean %
148	120.06 (512)	129.17 (100)	7.58
151	135.39 (298)	144.21 (178)	6.51

Table 4.12: Comparison of screening meson mass continuum limit extrapolations with ($m_{\text{cont.}}$) and without ($m_{\text{cont.,no th.}}$) thermodynamic limit beforehand for mass ratio $m_s/m_l = 80$. The systematic uncertainty of the mean value is calculated via $\frac{|m_{\text{cont.}} - m_{\text{cont.,no th.}}|}{m_{\text{cont.}}}$ using only the mean values.

We want to also compare the systematic uncertainties we would get by skipping the continuum limit extrapolations to the systematic uncertainties we got from skipping the thermodynamic limit extrapolations. For that we compare now the masses in Tab. 4.12 to the masses from $N_\tau = 12$ lattices in Tab. 4.9 and Tab. 4.10. We see, if we compare the continuum masses without thermodynamic limit extrapolation to the $N_\tau = 12$ masses without thermodynamic limit extrapolation, that they do not even agree within 95% confidence interval. If we compare the continuum masses with thermody-

namic limit extrapolation to the $N_\tau = 12$ masses with thermodynamic limit extrapolations, we see that they agree within at least 95% confidence interval. Comparing however the continuum masses without thermodynamic limit extrapolation to the $N_\tau = 12$ masses with thermodynamic limit extrapolation they do not all agree within 95% confidence interval. Both continuum extrapolations, with or without thermodynamic limit extrapolation, however agree within at least the 95% confidence interval.

From this detailed study of the thermodynamic and continuum limit at the two temperatures we conclude that for large enough lattices the thermodynamic limit might not be necessary for our screening masses because the uncertainties agree with each other in the 95% confidence interval. Therefore we will use here also our largest volumes for further analysis. The continuum limit on the other hand is necessary because the systematic uncertainties would be otherwise too large and therefore we need to perform continuum limit extrapolations before a chiral limit extrapolation.

As for the other temperatures simple pointwise extrapolations are not possible due to the lack of available data, in the following we will interpolate between the data points for more continuum extrapolations. For this we first need to do an interpolation of temperature. To interpolate our masses in temperature we will use our largest lattices as well as masses from smaller volumes at high temperatures beyond the temperature range of our largest volumes. We include masses from smaller volumes at high temperatures because their volume effects at those temperatures are small as we saw in subsection 4.4.1. We use temperature interpolation with cubic splines, those splines also have a function built-in for the continuum extrapolation, which we constrain. At low temperatures, $T = 25$ MeV and $T = 50$ MeV, we constrain the first derivative after temperature of the fit to be equal to zero. For high temperature, well above the available temperature region of our study, we constrain the first derivative after temperature to be equal to 2π at $T = 1.5$ GeV. To make sure that the continuum extrapolations for our temperature interpolation agrees with the pointwise continuum extrapolation and to check for possible discrepancies resulting from higher order cut-off effects, we compare in Fig. 4.16 different possibilities to extrapolate to continuum masses. Here we use the masses from largest available lattice volume as a starting point. We see that all these variations agree within uncertainties with each other. From Fig. 4.16 it is vivid that the temperature interpolation works very well and that the masses of all the different cut-offs N_τ have mainly cut-off effects linear in $1/N_\tau^2$. In Tab. 4.13 we summarized the continuum-extrapolated masses from Fig. 4.16.

In Fig. 4.17 we show the continuum limit extrapolations using temperature interpolation for mass ratio $m_s/m_l = 80$ using a linear fitting function in $1/N_\tau^2$ and all $N_\tau = 6, 8, 12$ (yellow and light grey from Fig. 4.16). We use them because all fits agreed within uncertainties and they have the most

degrees of freedom. This counters possible overfitting and stabilizes the fit.

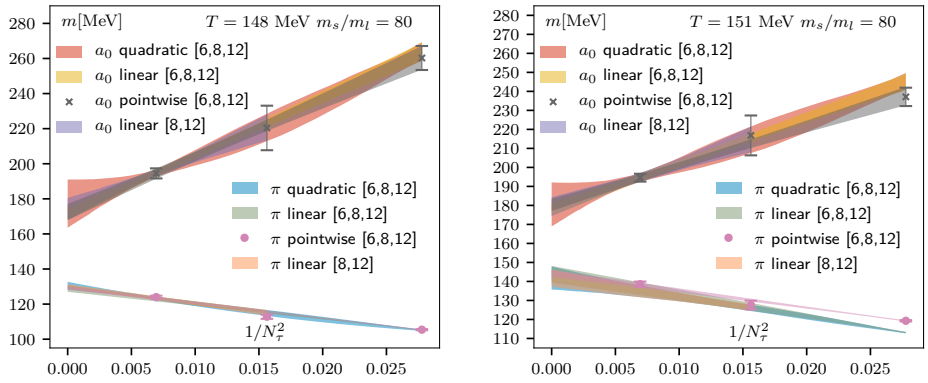

Figure 4.16: Comparison of the pointwise continuum extrapolation from Fig. 4.15 (dark grey, purple) to different continuum extrapolations using temperature interpolated data points for screening masses at mass ratio $m_s/m_l = 80$. Linear and quadratic means that the fitting function for the continuum extrapolation is linear (yellow, violet, light grey, light orange) or linear and quadratic (red, blue) in $1/N_\tau^2$. In square brackets are the N_τ of the used lattices. Largest volume lattices where used without thermodynamic limit. Left: At temperature $T = 148$ MeV. Right: At temperature $T = 151$ MeV.

T	$m_{a_0,\text{quadratic}}[6,8,12]$	$m_{a_0,\text{linear}}[6,8,12]$	$m_{a_0,\text{linear}}[8,12]$	$m_{a_0,\text{pointwise}}[6,8,12]$
148	177.25(1375)	171.57 (312)	174.30 (622)	172.43 (464)
151	180.52(1156)	178.03 (330)	179.30 (491)	180.29 (322)
T	$m_{\pi,\text{quadratic}}[6,8,12]$	$m_{\pi,\text{linear}}[6,8,12]$	$m_{\pi,\text{linear}}[8,12]$	$m_{\pi,\text{pointwise}}[6,8,12]$
148	130.51 (221)	128.77 (179)	130.03 (132)	129.17 (100)
151	141.79 (606)	143.80 (438)	141.73 (453)	144.21 (178)

Table 4.13: The different continuum-extrapolated masses from Fig. 4.16 in comparison. For details on the different continuum extrapolations see caption of Fig. 4.16. Temperatures T and masses m are in MeV. In square brackets are the N_τ of the used lattices.

As can be seen in Fig. 4.17, the continuum for m_{a_0} is approached from above while for the m_π it is appoached from below. This behaviour is similar to a previous study at physical mass ratio $m_s/m_l = 27$ [12]. In that study a slightly different behavior of m_{a_0} was seen. At temperatures below and around T_pc the extrapolation resulted in lower continuum masses, while at temperatures above T_pc the extrapolation resulted in higher continuum masses. For m_{a_0} we only see the behavior of below and around T_pc of the

study [12], which might be due to the smaller temperature range compared to the previous study. Nonetheless it would be plausible that it would also happen here. In the bottom plot of Fig. 4.17 we see a possible degeneration towards the upper bound of our temperature range, which would mean that $U_A(1)$ is effectively restored there. The temperature interpolations and continuum extrapolations however might need additional $N_\tau = 6$ points at higher temperatures since we lack these data points and improvement on the two highest temperature $N_\tau = 8$ points to give a definitive answer regarding the temperature at which results for m_π and m_{a_0} start to agree.

Using the results from Ref. [12] we can compare our results for mass ratios $m_s/m_l = 80$ and $m_s/m_l = 40$ to mass ratio $m_s/m_l = 27$. For $m_s/m_l = 40$ we have also used a continuum extrapolation linear in $1/N_\tau^2$ while we only had $N_\tau = 8, 12$ lattices. In Fig. 4.18 we show such a comparison.

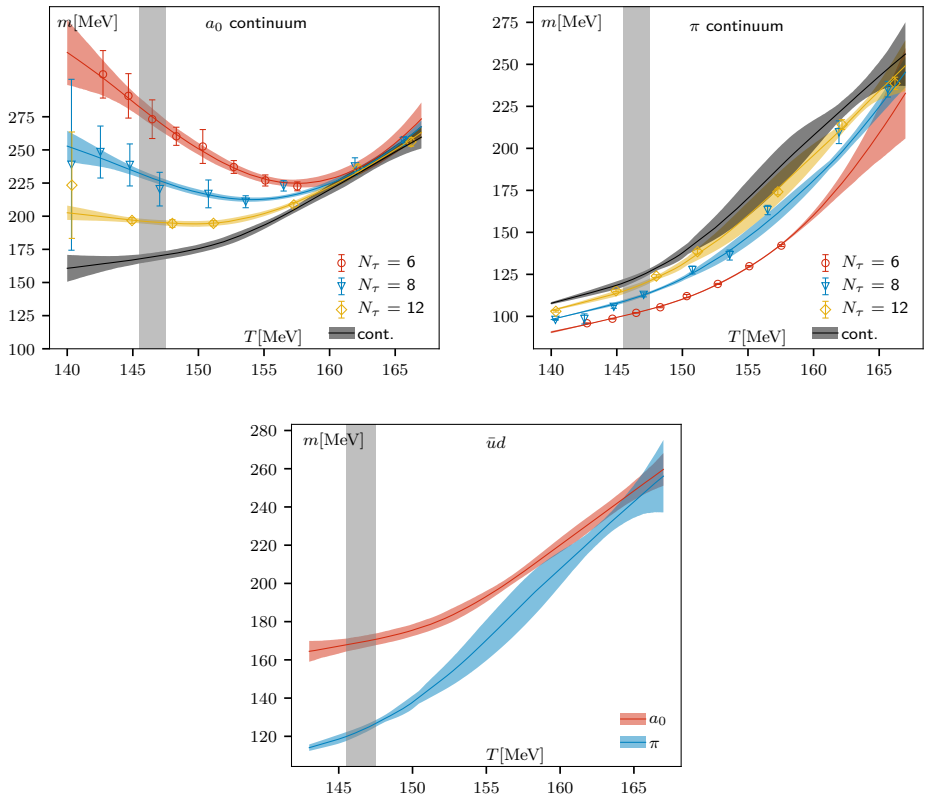

Figure 4.17: Continuum extrapolation linear in $1/N_\tau^2$ with uncertainty bands for mass ratio $m_s/m_l = 80$ using cubic spline interpolations in temperature. Left: m_{a_0}. Right: m_π. Bottom: Continuum bands of m_{a_0} and m_π combined. The vertical grey band corresponds to the continuum pseudo-critical temperature $T_{\mathrm{pc,cont.}}$ for mass ratio $m_s/m_l = 80$.

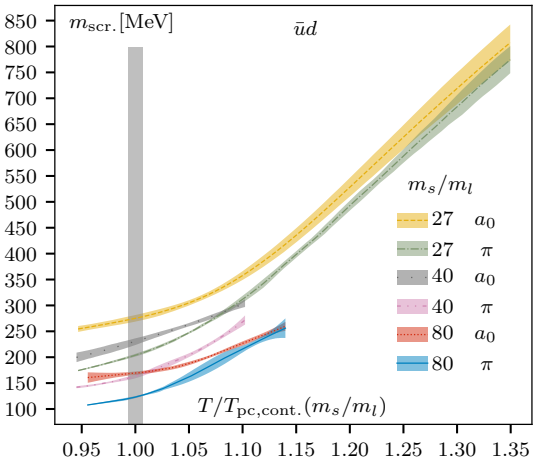

Figure 4.18: Comparison of the continuum-extrapolated screening masses m_π and m_{a_0} for $m_s/m_l = 27$, $m_s/m_l = 40$ and $m_s/m_l = 80$ as a function of temperature scaled by their respective pseudo-critical temperature in the continuum limit $T_{\mathrm{pc,cont.}}$. The grey vertical band illustrates the transition temperature; the width is just to guide the eye.

We see in Fig. 4.18 that for smaller light quark masses m_l, i.e. larger m_s/m_l, the temperature at which results for m_π and m_{a_0} start to agree (degeneration temperature) seems to approach their pseudo-critical transition temperature T_{pc}. That would mean that the breaking of $U_A(1)$ becomes smaller for smaller light quark masses, i.e. towards the chiral limit and that could mean that the explicit breaking of $U_A(1)$ through the light quark masses m_l is the dominant breaking cause at those mass ratios. Keep in mind that the degeneration temperature for mass ratio $m_s/m_l = 80$ might be beyond our temperature range, because m_π and m_{a_0} agree within uncertainty bands only at the upper boundary of our temperature range and that might change if we improve our temperature interpolation, e.g. if we extend the temperature range by calculating correlators for even higher temperatures. Finding the degeneration temperature was however not a subject of this thesis. Note that the maximum temperature for mass ratio $m_s/m_l = 40$ is too low (maximum $T/T_{\mathrm{pc,cont.}}(m_s/m_l)$ is even smaller than for $m_s/m_l = 80$) to see the degeneration of m_π and m_{a_0}. From this we would expect that the degeneration temperature for mass ratio $m_s/m_l = 40$ falls between the degeneration temperatures for $m_s/m_l = 80$ and $m_s/m_l = 27$.

Whether or not it becomes degenerate in the transition region can only be stated if a chiral limit extrapolation is done. We will discuss that in section 4.6. Before that we will have a look into the continuum extrapolation for susceptibilities in subsection 4.5.2.

4.5.2 Susceptibilities

Coming back to the susceptibilities before we proceed to the chiral limit, we also want to remove the cut-off effects of our susceptibilities and compare them to the screening masses. In this subsection we want to extrapolate the susceptibilities back to continuum physics via continuum limit extrapolations to remove the cut-off effects from our specific choice of discretization. Similar to subsection 4.5.1 we need susceptibilities at different N_τ at fixed mass ratio m_s/m_l and fixed temperature T. In Fig. 4.19 we show the results after the thermodynamic limit that we obtained in subsection 4.4.2 for the two temperatures $T \approx 148$ MeV and $T \approx 151$ MeV plotted against $1/N_\tau^2$. We expected a linear dependence for the continuum limit due to our ansatz from Eq. 3.8.

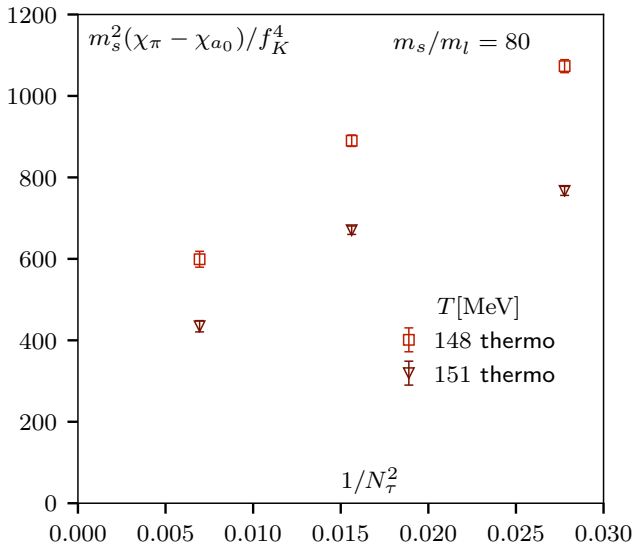

Figure 4.19: Infinite-volume-extrapolated susceptibilities for mass ratio $m_s/m_l = 80$ plotted against $1/N_\tau^2$. A linear dependence was expected.

Unlike the corresponding screening masses these points are not on a linear line. We therefore assume that our $N_\tau = 6$ values still have higher order contributions beyond the leading order correction of $\mathcal{O}(a^2)$. Similar differences for $N_\tau = 6$ were already observed in [40].

We begin again with the comparison of pointwise continuum limit extrapolations starting once from infinite-volume-extrapolated values and once from values at the largest volumes. For details of what pointwise extrapolation means, see the beginning of section 4.5. In Fig. 4.20 we show the comparison of these different pointwise continuum extrapolations using our

two largest N_τ, $N_\tau = 8, 12$, at $T \approx 148$ MeV and $T \approx 151$ MeV.

From Fig. 4.20 we can conclude that for the pointwise extrapolation, the continuum extrapolation using infinite-volume-extrapolated susceptibilities agrees within uncertainty bands with the continuum extrapolation using susceptibilities from largest volumes only. The $N_\tau = 6$ data would be clearly missed on these lines, which implies that the $N_\tau = 6$ data has higher order cut-off effects. Skipping the thermodynamic limit extrapolation lowers the value after the continuum limit extrapolation compared to its proper limits, but both ways still agree within uncertainties. Therefore this skip could (falsely) conclude an earlier effective $U_A(1)$ restoration similar to the screening masses, because at a value of zero $U_A(1)$ would effectively be restored. The results of our calculations are given in Tab. 4.14.

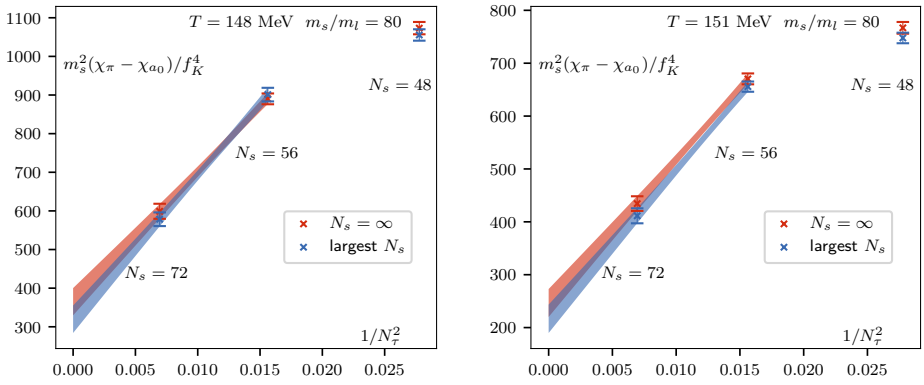

Figure 4.20: Comparison of pointwise linear continuum limit extrapolations for our susceptibility observable at mass ratio $m_s/m_l = 80$. Left: Extrapolations using values after the thermodynamic limit ($N_s = \infty$, red) and from largest volumes ($N_s = 48, 56, 72$, blue) at $T \approx 148$ MeV. Right: Same as left but at $T \approx 151$ MeV.

T[MeV]	$X_{\text{cont.}}$	$X_{\text{cont.,no th.}}$	systematic uncertainty mean %
148	364.88(3531)	319.52(3557)	12.43
151	246.51(2641)	216.64(2687)	12.12

Table 4.14: Comparison of continuum limit extrapolations of our susceptibility observable $X = m_s^2(\chi_\pi - \chi_{a_0})/f_K^4$ with ($X_{\text{cont.}}$) and without ($X_{\text{cont.,no th.}}$) thermodynamic limit beforehand for mass ratio $m_s/m_l = 80$. The systematic uncertainty is calculated via $\frac{|X_{\text{cont.,no th.}} - X_{\text{cont.}}|}{X_{\text{cont.}}}$ using only the mean values.

We want to also compare the systematic uncertainties we would get by skipping the continuum limit extrapolations to the systematic uncertainties we got from skipping the thermodynamic limit extrapolations. For that we compare now the susceptibility in Tab. 4.14 to the susceptibility from $N_\tau = 12$ lattices in Tab. 4.11. We see, if we compare the continuum susceptibilities without thermodynamic limit extrapolation to the $N_\tau = 12$ susceptibility without thermodynamic limit extrapolation, that they do not even agree within 95% confidence interval. If we compare the continuum susceptibilities with thermodynamic limit extrapolation to the $N_\tau = 12$ susceptibilities with thermodynamic limit extrapolations, we see that they also do not even agree within 95% confidence interval. Comparing the continuum susceptibilities without thermodynamic limit extrapolation to the $N_\tau = 12$ susceptibilities with thermodynamic limit extrapolation they also do not even agree within 95% confidence interval.

From this detailed study of the thermodynamic and continuum limit at the two temperatures we conclude that for large enough lattices the thermodynamic limit might not be necessary for our susceptibility observable because the uncertainties agree with each other in the 68% confidence interval. Therefore we will use here also our largest volumes for further analysis. The continuum limit on the other hand is necessary because the systematic uncertainties would be otherwise too large and therefore we need to perform continuum limit extrapolations before a chiral limit extrapolation.

As for the other temperatures simple pointwise extrapolations are not possible due to the lack of available data, in the following we will interpolate between the data points for more continuum extrapolations. For this we first need to do an interpolation of temperature. To interpolate our susceptibilities in temperature we will again use our largest lattices as well as susceptibilities from smaller volumes at high temperatures beyond the temperature range of our largest volumes. We include the susceptibilities from smaller volumes at high temperatures because their volume effects at those temperatures are small as we saw in subsection 4.4.2. We use temperature interpolation with cubic splines, those splines also have a function built-in for the continuum extrapolation, which we constrain. We only constrain our interpolation at high temperature, well above the available temperature region of our study. We constrain the first derivative to be equal to 0 at $T = 0.5$ GeV. For more details on how the temperature interpolation works, see the beginning of section 4.5. To make sure that the continuum extrapolations for our temperature interpolation agree with the pointwise continuum extrapolations and to check for possible discrepancies resulting from higher order cut-off effects we compare different possibilities of continuum extrapolations for susceptibilities. Studies with other chiral observables [40] have shown that including or excluding $N_\tau = 6$ lattices to the analysis give slightly different results with an ansatz linear in $1/N_\tau^2$, which means that the $N_\tau = 6$ lattices have signif-

icant cut-off effects beyond the linear cut-off effect in $1/N_\tau^2$ for these chiral observables. Since the next higher order is quadratic in $1/N_\tau^2$, we compared linear fits including the additional quadratic term with linear fits dropping the $N_\tau = 6$ points completely. All methods use values from largest lattice volumes as a starting point. In Fig. 4.21 we show the results.

We see in Fig. 4.21 that the linear extrapolation in $1/N_\tau^2$ with all three N_τ (yellow) including $N_\tau = 6$ differ at $T = 148$ MeV from all the other extrapolations including the extrapolation with an additional quadratic term (red). Therefore we conclude that susceptiblity values at $N_\tau = 6$ are not just linear in $1/N_\tau^2$ but have also a quadratic term. Again we want to interpolate between all the available temperatures and perform continuum extrapolations on those interpolated bands. We therefore use a linear and quadratic fitting function in $1/N_\tau^2$ for the extrapolation (red in Fig. 4.21) for $m_s/m_l = 80$ as it uses all N_τ and is as accurate as the linear fitting function for the extrapolation with $N_\tau = 8, 12$ (grey in Fig. 4.21). In Tab. 4.15 we summarized the results of the continuum-extrapolated susceptibility difference from Fig. 4.21.

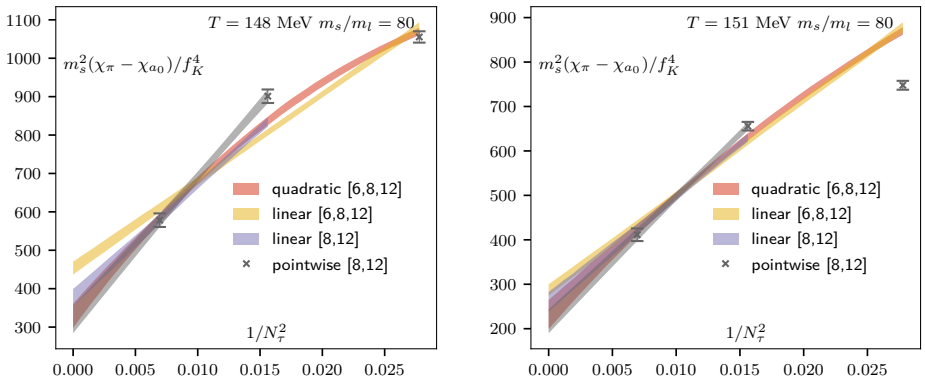

Figure 4.21: Comparison of the pointwise continuum extrapolation from Fig. 4.20 (dark grey) to different continuum extrapolation variations using temperature interpolated data points for susceptibilities at mass ratio $m_s/m_l = 80$. Linear and quadratic means that the fitting function for the continuum extrapolation is linear (yellow, violet) or linear and quadratic in $1/N_\tau^2$ (red). In square brackets are the used N_τ for the fit. Largest volume lattices where used without thermodynamic limit. Left: At temperature $T \approx 148$ MeV. Right: At temperature $T \approx 151$ MeV.

In Fig. 4.22 we show the result of our continuum extrapolation as bands for our temperature range. As a reminder we used values from smaller volumes at high temperatures where we do not have the largest volumes available. As an ansatz for the continuum limit extrapolation we used the one

with linear and quadratic terms using all three N_τ, $N_\tau = 6, 8, 12$ (red, blue, yellow, respectively), for mass ratio $m_s/m_l = 80$.

T	$X_{\text{quadratic}}[6,8,12]$	$X_{\text{linear}}[6,8,12]$	$X_{\text{linear}}[8,12]$	$X_{\text{pointwise}}[6,8,12]$
148	329.45(3141)	453.48(1690)	376.61(2259)	319.52(3557)
151	231.97(3285)	287.12(1300)	260.72(2207)	216.64(2687)

Table 4.15: The different continuum-extrapolated values of our observable $X = m_s^2(\chi_\pi - \chi_{a_0})/f_K^4$ from Fig. 4.21 in comparison. For details on the different continuum extrapolations see caption of Fig. 4.21. Temperatures T are in MeV. In square brackets are the N_τ of the used lattices.

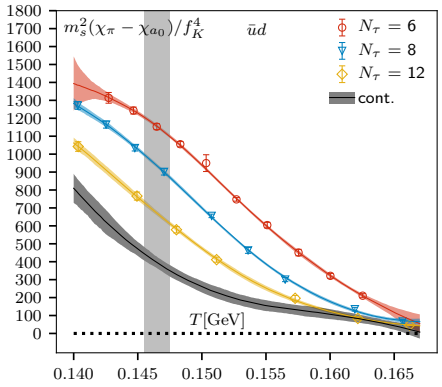

Figure 4.22: Continuum extrapolation linear and quadratic in $1/N_\tau^2$ with uncertainty bands of the susceptibility difference of χ_π and χ_{a_0} for mass ratio $m_s/m_l = 80$ using cubic spline interpolations in temperature. The vertical grey band corresponds to the continuum pseudo-critical temperature $T_{\text{pc,cont.}}$ for mass ratio $m_s/m_l = 80$.

Now we can compare our results for the continuum-extrapolated susceptibility difference of χ_π and χ_{a_0} for mass ratios $m_s/m_l = 80$ and $m_s/m_l = 40$ to the results at mass ratio $m_s/m_l = 27$ from Ref. [12]. In Fig. 4.23 we show such a comparison.

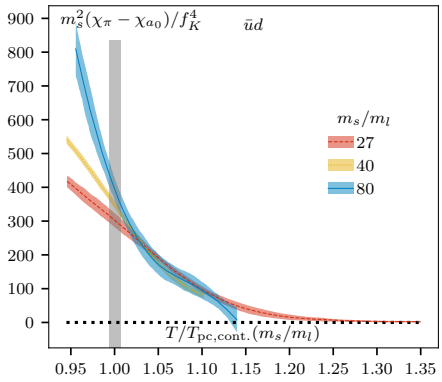

Figure 4.23: Comparison of the continuum-extrapolated susceptibility difference of χ_π and χ_{a_0} for $m_s/m_l = 27$, $m_s/m_l = 40$ and $m_s/m_l = 80$ normalized by the physical strange quark mass m_s and the Kaon decay constant f_K as function of temperature scaled by their respective pseudo-critical temperature in the continuum limit $T_{\mathrm{pc,cont.}}(m_s/m_l)$. The interpolation and extrapolation for $m_s/m_l = 80$ are from Fig. 4.22, for $m_s/m_l = 27$ are from Ref. [12] and for $m_s/m_l = 40$ are the same as for $m_s/m_l = 80$ but with only a linear fitting function in $1/N_\tau^2$ using both $N_\tau = 8, 12$. The grey vertical band illustrates the transition temperature; the width is just to guide the eye.

Analogously to the screening masses (section 4.5.1) we see that for smaller light quark masses m_l, i.e. larger m_s/m_l, the temperature at which results for the susceptibility difference start to agree with 0 (degeneration temperature) seems to approach their pseudo-critical transition temperature T_{pc}. It makes sense that we see a similar behavior because the screening masses and their susceptibilities contain the same information regarding the $U_A(1)$ symmetry. That would mean that the breaking of $U_A(1)$ becomes smaller for smaller light quark masses, i.e. towards the chiral limit and that could mean that the explicit breaking of $U_A(1)$ through the light quark masses m_l could be the dominant breaking cause at those mass ratios. Keep in mind that the degeneration temperature for mass ratio $m_s/m_l = 80$ might be beyond our temperature range, because the susceptibilities are degenerate only at the upper boundary of our temperature range and that might change if we e.g. extend the temperature range by calculating correlators for even higher temperatures. Finding the degeneration temperature was again not a subject of this thesis. Note again that the maximum temperature for mass ratio $m_s/m_l = 40$ is too low (maximum $T/T_{\mathrm{pc,cont.}}(m_s/m_l)$ is even smaller than for $m_s/m_l = 80$) to see its degeneration. Note also that we had to change the fitting function for mass ratio $m_s/m_l = 40$ to a linear extrapolation since we only have $N_\tau = 8, 12$. From the observation that for smaller light

quark masses m_l the degeneration temperature approaches their phase transition temperature T_{pc} we would expect that the degeneration temperature for mass ratio $m_s/m_l = 40$ falls between the degeneration temperatures for $m_s/m_l = 80$ and $m_s/m_l = 27$. Together with the results from subsection 4.5.1 we would therefore expect that the $U_A(1)$ symmetry is either broken or has very small breaking, i.e. is effectively restored, at the chiral phase transition. That would support the scenario in the left plot of Fig. 2.2, which would mean that the chiral phase transition is second order. For details about the potential scenarios see section 2.10.

Assuming that the degeneration temperature for $m_s/m_l = 80$ is correct and that for decreasing m_l the degeneration temperature relative to their pseudo-critical temperature $T_{\text{pc,cont.}}(m_s/m_l)$ always decreases, we can construct an upper bound for the degeneration temperature in the chiral limit. The degeneration point for mass ratio $m_s/m_l = 80$ is then $T/T_{\text{pc,cont.}} \approx 1.15$. The critical temperature is $T_c = 132^{+3}_{-6}$ MeV [8] and that would mean that the degeneration temperature in the chiral limit would be $T_{\text{degen.},c} < 1.15 T_c \approx 151.8$ MeV.

From the discussion of our results in this section we can conclude from our observations that the $U_A(1)$ symmetry gets effectively restored at lower temperatures relative to their pseudo-critical temperature $T_{\text{pc,cont.}}(m_s/m_l)$ for lower light quark masses m_l. Whether or not it becomes degenerate in the transition area can again only be stated if a chiral limit extrapolation is done. We will discuss that in the following section 4.6.

4.6 Chiral limit

To finally answer the main question of this thesis, whether the $U_A(1)$ symmetry is effectively restored at the chiral phase transition or not, we need to perform the chiral limit extrapolation. For the chiral limit we need continuum-extrapolated values of at least three different mass ratios. At this point we have continuum-extrapolated values for screening masses and our susceptibility observable for mass ratios $m_s/m_l = 27$, $m_s/m_l = 40$ and $m_s/m_l = 80$.

If we want to answer the main question of this thesis, the possible restoration of $U_A(1)$ in the chiral limit at the transition temperature, we first need to extract suitable values for such a chiral limit extrapolation. Since the pseudo-critical temperature $T_{\text{pc,cont.}}$ depends also on the mass ratio m_s/m_l and becomes smaller for higher values of m_s/m_l, i.e. towards the chiral limit, we now want to extract these values at the corresponding transition temperature for each m_s/m_l. Due to the fact that around physical quark masses the transition is a cross-over rather than a true phase transition of first or

second order, we consider values of the whole range of this transition temperature $I = [T_{\text{pc,cont.}} - \Delta T_{\text{pc,cont.}}, T_{\text{pc,cont.}} + \Delta T_{\text{pc,cont.}}]$. Therefore we extracted the largest $\max\{X(T) \pm \Delta X(T)\}\ \forall T \in I$ and the smallest values $\min\{X(T) \pm \Delta X(T)\}\ \forall T \in I$ of all observables X within this temperature range and consider these values as the upper X_{max} and lower bound X_{min} in the sense of a value range similar to uncertainties. We consider their arithmetic mean $X_{\text{transition}} = \frac{X_{\text{max}}+X_{\text{min}}}{2}$ as the mean value and the difference of this mean value to the largest or smallest value as the uncertainty $\Delta X_{\text{transition}} = X_{\text{max}} - X_{\text{transition}}$ at the transition temperature. As T_{pc} we used the values mentioned in subsection 4.3.1.

For the extrapolation we used the same strategy as for the thermodynamic limit (see section 4.4 for details on the procedure) to perform $m_l/m_s \to 0$ extrapolations. We took 1000 random values for the chiral limit extrapolations. If we assume at least a linear fitting function we need values for at least two different m_l/m_s, but better three, to verify a linear behaviour. For details on our ansatz see section 3.4.

We start with the chiral limit extrapolation of the screening masses in the next subsection 4.6.1.

4.6.1 Screening masses

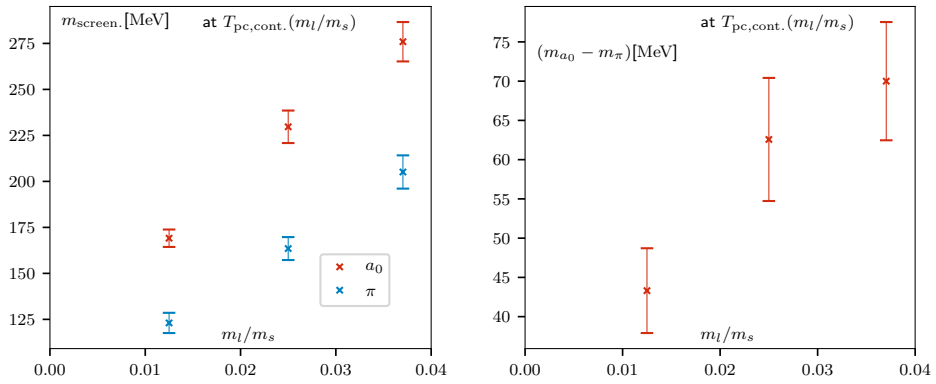

Figure 4.24: Screening masses of a_0 and π at their pseudo-critial temperature $T_{\text{pc,cont.}}$ as a function of the explicit symmetry breaking parameter m_l/m_s. Left: The individual screening masses. Right: The difference between those two screening masses as a measure of $U_A(1)$ symmetry breaking.

In this subsection we want to remove the explicit breaking of the $U_A(1)$ symmetry through the light quark mass m_l for the screening masses by performing chiral limit extrapolations. In Fig. 4.24 we show the screening masses as a function of the explicit breaking of $U_A(1)$ symmetry, m_l/m_s, at their

corresponding $T_{\mathrm{pc,cont.}}(m_l/m_s)$. We show the individual screening masses (left) and also the difference of the two masses (right), which gives a measure of $U_A(1)$ symmetry breaking analogous to our susceptibility observable. The difference is taken before the continuum limit extrapolation using mostly largest volume lattices; for details see sections 4.4 and 4.5.

Since from this stage it was not clear for us how to proceed, we tried different ansätze on the mass difference. The straightforward approach is just a linear function in m_l/m_s. Another idea is a square root fitting function since the pion is a Goldstone boson below T_c and therefore its mass should behave like a square root of m_l/m_s going towards 0. Another simple idea is combining those two functions to a linear and square root fitting funtion, cf. section 3.4. In Fig. 4.25 we show those three fits.

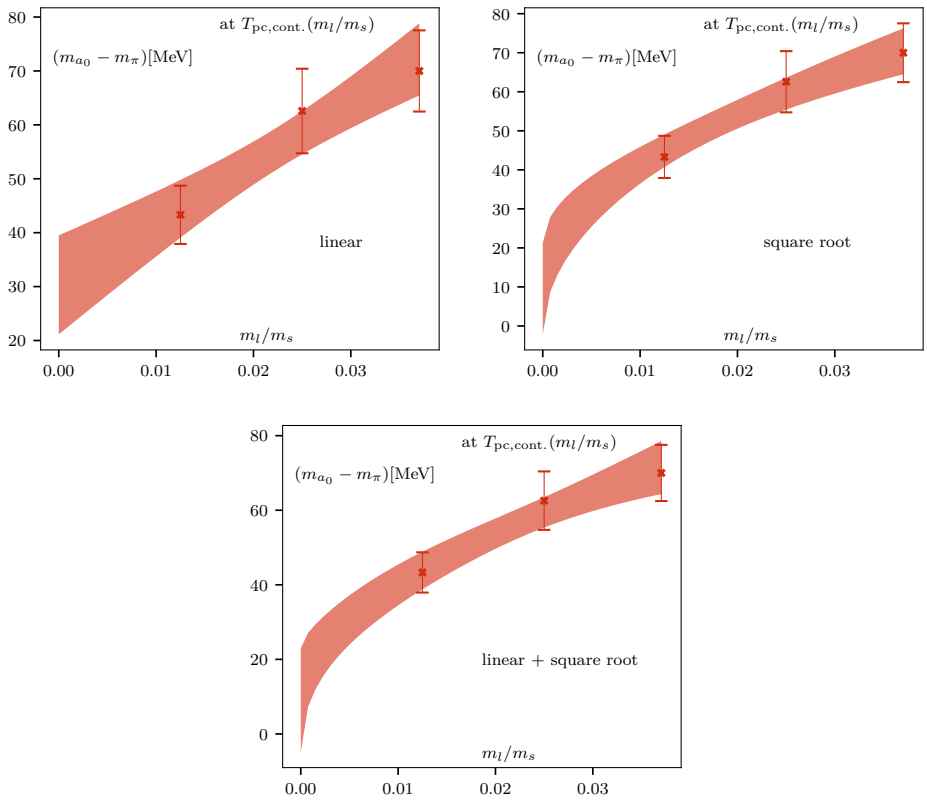

Figure 4.25: Different fits for the chiral limit extrapolation of the mass difference of m_{a_0} and m_π. Top left: Linear function. Top right: Square root function. Bottom: Fitting function containing both terms.

We see from Fig. 4.25 that depending on the fitting function the chiral limit extrapolation would lead to either no degeneracy of $U_A(1)$ in the linear

case or to a potential degeneracy in the case of square root functions with and without an additional linear term. That is an inconclusive result. With the current data points however we can neither be sure of what is the right function nor if it becomes degenerate or not. To answer those questions more data points at smaller mass ratios m_l/m_s are needed. Also the extracted m_{a_0} is inconclusive due to the unphysical decay channel as mentioned in subsection 4.3.1. In Tab. 4.16 we have summarized the chiral limit fitting results and χ^2 fitting results for comparison. As can be seen the linear fitting function as well as the square root fitting function have very low χ^2 values and the chiral limit mass difference values agree within uncertainties.

Fitting function	m_{diff}[MeV]	m_{diff}[MeV] from χ^2	χ^2/d.o.f.
linear	30.322 (9183)	30.183 (5576)	0.3857163
square root	9.573(11727)	5.597 (7025)	0.1812405
linear + square root	9.041(13906)	-	-

Table 4.16: Chiral-limit-extrapolated results of the screening mass difference $m_{\text{diff}} = m_{a_0} - m_\pi$. Results differ depending on the fitting function. Comparison of chiral-limit-extrapolated mass difference from our fit method (m_{diff}) and a χ^2 fit (m_{diff} from χ^2) with its corresponding χ^2/d.o.f.. For our fit method see section 4.6.

Since the chiral limit extrapolations for the screening masses are inconclusive at that point we have to take a closer look at the chiral limit extrapolations of the susceptibilities. We finish the result chapter therefore with the chiral limit extrapolations of the susceptibilities in the last subsection of this chapter 4.6.2.

4.6.2 Susceptibilities

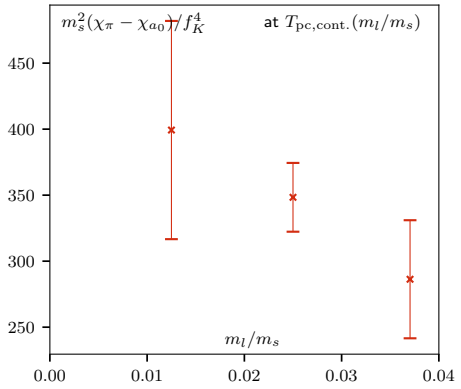

Figure 4.26: Susceptibility difference at their pseudo-critical temperature $T_{\mathrm{pc,cont.}}$ as a function of the explicit symmetry breaking parameter m_l/m_s. The difference is a measure for $U_A(1)$ symmetry breaking.

In this subsection we want to remove the explicit breaking of the $U_A(1)$ symmetry through the light quark mass m_l for the susceptibilities by performing chiral limit extrapolations. Similar to subsection 4.6.1 we show in Fig. 4.26 our susceptibility observable as a function of the explicit breaking of $U_A(1)$ symmetry m_l/m_s.

Looking at Fig. 4.26 we see a rather unlikely degeneration of χ_π and χ_{a_0} towards the chiral limit, unless the function is very different from the ones we proposed in section 3.4. This could mean that the largest quark mass ratio $m_l/m_s = 1/27$ is potentially outside of that simple scaling regime similar to the $N_\tau = 6$ values for the linear continuum limit extrapolation in $1/N_\tau^2$; for details on that see subsection 4.5.2. Nonetheless we show in Fig. 4.27 the fits using the fitting ideas from section 3.4, i.e. a linear, a square root to the power of 3 and a linear combined with a square root to the power of 3 fitting function.

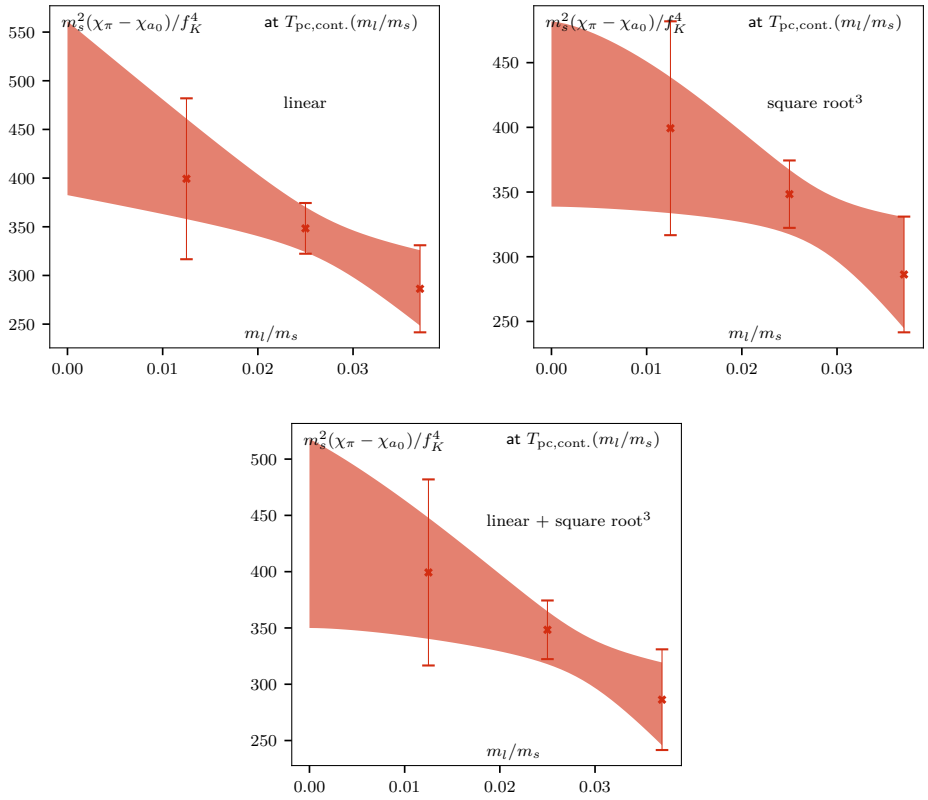

Figure 4.27: Different fitting function ideas for the chiral limit extrapolation of the susceptibility difference of χ_π and χ_{a_0}. Top left: Linear function. Top right: Square root to the power of 3 function. Bottom: Fitting function containing both terms.

We see in Fig. 4.27 that the chiral limit extrapolations differ a lot between the different fitting functions. Nonetheless the susceptibilites all rise towards $m_l/m_s = 0$ and agree of being clearly above 0, which would mean that there is no $U_A(1)$ symmetry restoration at T_c in the chiral limit. For Fig. 4.28 we used the same fitting functions as in Fig. 4.27 but with the inverse of that observable as we motivated in section 3.4. We see that towards $m_l/m_s = 0$ the values decrease and become very small but still non-zero as well, which would mean that the breaking is large but not divergently large and therefore hints again to a non-degeneracy of χ_π and χ_{a_0} at the phase transition temperature in the chiral limit. These findings are not in accordance to the screening mass chiral limit extrapolations, which had a possible $U_A(1)$ symmetry restoration at T_c for some fitting functions. One possible reason for that is that the screening mass extrapolation might be imprecise due to the problem in the scalar mass. Another possible reason might be that the $m_s/m_l = 27$ value for

the susceptibilities is not in the scaling regime for a chiral limit extrapolation similar to the $N_\tau = 6$ value for its linear continuum limit extrapolation in $1/N_\tau^2$. A very probable other reason is that the used fitting functions are just incorrect. However in Tab. 4.17 we have summarized the chiral limit fitting results. Like in the case of screening masses (subsection 4.6.1) the χ^2 values are very small and the chiral-limit-extrapolated values agree within uncertainties with our method. Interestingly inverting the values of χ_{diff} from Tab. 4.17 is in the order of 10^{-3}, which is the same order as the values of χ_{diff}^{-1}.

Besides that we saw a similar predicition already in one of our ealier studies [67]. That study did a spline interpolation between the susceptibility differences of different m_l/m_s with physical strange quark mass m_s at fixed temperatures and predicted their behavior in the chiral limit. The susceptibility difference was not in the thermodynamic or continuum limit, which means that we should be a bit careful with the interpretation of that study. The study predicted that for higher temperatures, i.e. $T \approx 166$ MeV and $T \approx 162$ MeV, the suceptibility difference would be vanishing in the chiral limit $m_l \to 0$. That would be in good accordance with our prediction that for decreasing mass ratios m_l/m_s the susceptibility difference vanishes at lower temperatures relative to their pseudo-critical temperature $T_{\text{pc,cont.}}(m_l/m_s)$, where the critical temperature, the phase transition temperature in the chiral limit, is $T_c = 132^{+3}_{-6}$ MeV [8]. We predicted in subsection 4.5.2 under the assumption that the temperature at which the results of m_π and m_{a_0} as well as the susceptibility difference and 0 start to agree (degeneration temperature) for $m_s/m_l = 80$ is correct and that for decreasing m_l the degeneration temperature relative to their pseudo-critical temperature $T_{\text{pc,cont.}}(m_l/m_s)$ always decreases that the degeneration temperature in the chiral limit is $T_{\text{degen.},c} < 1.15 T_c \approx 151.8$ MeV. For decreasing temperatures the prediction of the study [67] seems to be not so clear anymore. Especially at temperatures $T \approx 151$ MeV and $T \approx 145$ MeV it seems that the susceptibility difference is diverging in the chiral limit. Since the continuum critical temperature corresponding to $m_l/m_s = 0$ is $T_c = 132^{+3}_{-6}$ MeV [8], we would assume from that study [67] that the susceptibility difference will not vanish and therefore the $U_A(1)$ symmetry will not be effectively restored at the chiral phase transition. Of course it is important to note that the calculated χ_π is diverging below the pseudo-critical temperature T_{pc} corresponding to their mass ratios m_l/m_s; cf. Eq. 3.11. Those T_{pc} are higher for higher m_l/m_s. That is another reason why we extracted the susceptibility difference for our chiral limit extrapolation at the corresponding transition temperature $T_{\text{pc}}(m_l/m_s)$. Nonetheless we saw with Fig. 4.26 a starting position similar to that study and came here to the conclusion that $U_A(1)$ symmetry would not be effectively restored in the chiral limit at the transition temperature.

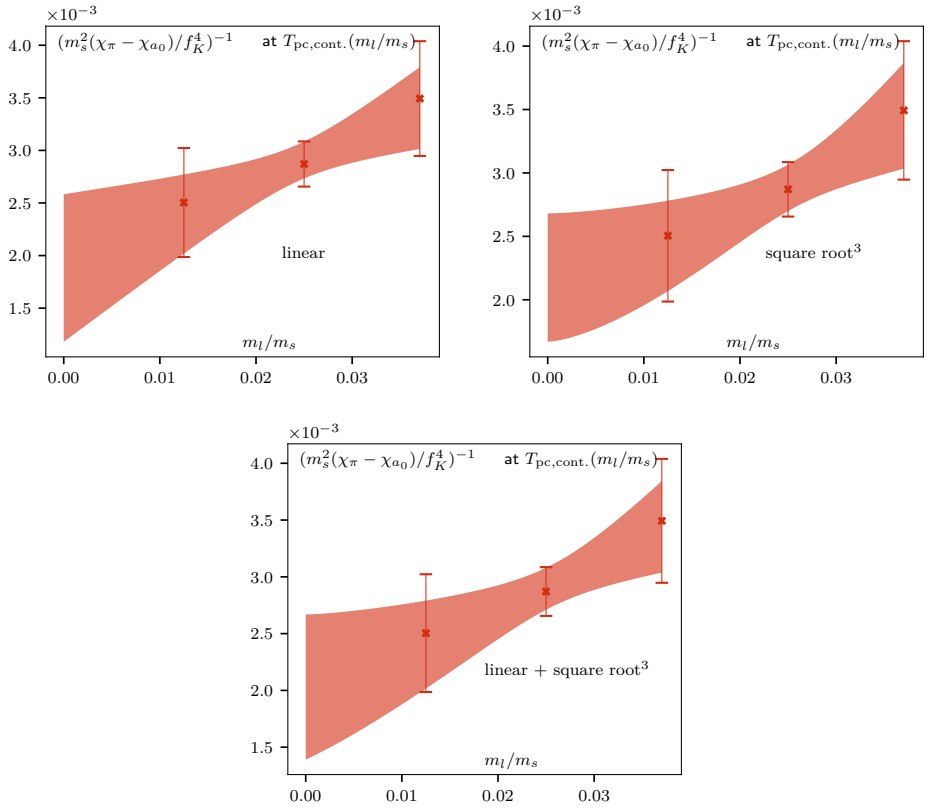

Figure 4.28: Same fitting functions as Fig. 4.27 but using the inverse values of our susceptibility observable.

Finally we want to compare our findings with the findings of other current research (see end of section 2.10 for a summary of the current status). All studies [15, 49, 50, 52] from section 2.10, which have found an effectively restored $U_A(1)$ symmetry, have used two-flavor QCD, which is not directly comparable with our $(2+1)$-flavor QCD. Nonetheless we want to try to unify those findings with our seemingly contrary findings. We can take a look at the temperature, where $U_A(1)$ symmetry gets effectively restored, relative to the transition temperature in both theories. This relative restoration should be comparable with two-flavor QCD. Some studies [50,52], which came to the conclusion that the $U_A(1)$ symmetry is effectively restored, were investigating a temperature range of 190-330 MeV, which is a range of around 1.11-1.95 T_c ($T_c \approx 170$ MeV for two-flavor QCD [51]), where T_c is the chiral phase transition temperature of the $N_f = 2$ QCD, which these papers studied. At those temperature ratios $U_A(1)$ could already be effectively restored because for mass ratio $m_s/m_l = 80$ we have seen in Fig. 4.23 that $U_A(1)$ might be already restored at a ratio of $T/T_{\text{pc,cont.}}(m_s/m_l) = 1.15$ and it is likely as we

have shown in subsection 4.4.2 that this temperature ratio might be smaller than 1.11 towards the chiral limit, which is below the temperature range of these studies.

Fitting function	χ_{diff}	χ_{diff} from χ^2	χ^2/d.o.f.
linear	468.09 (9225)	467.47 (1168)	0.015446
square root^3	331.43 (3839)	426.09 (65)	$9.6 \cdot 10^{-5}$
linear + square root^3	258.72(21765)	-	-
Fitting function	$\chi_{\text{diff}}^{-1}/10^{-3}$	$\chi_{\text{diff}}^{-1}/10^{-3}$ from χ^2	χ^2/d.o.f.
linear	1.882(702)	1.912(248)	0.100362
square root^3	2.175(506)	2.203 (96)	0.029625
linear + square root^3	2.030(639)	-	-

Table 4.17: Chiral-limit-extrapolated results of the susceptibility difference $\chi_{\text{diff}} = m_s^2(\chi_\pi - \chi_{a_0})/f_K^4$. Results differ depending on the fitting function. Comparison of chiral-limit-extrapolated susceptibility difference from our method (χ_{diff} and χ_{diff}^{-1}) and a least χ^2 fit ('χ_{diff} from χ^2' and 'χ_{diff}^{-1} from χ^2') with its corresponding χ^2/d.o.f.. For our fit method see section 4.6.

On the other side we compare our findings to the studies that have found a still broken $U_A(1)$ symmetry around or after the chiral phase transition [44–48]. Even though our findings agree on a broken $U_A(1)$ symmetry at the chiral phase transition, there are still some differences. The latest study [48] in that respect with $(2+1)$-flavor QCD using HISQ predicted a broken $U_A(1)$ symmetry even at $T \approx 205$ MeV $\approx 1.6T_c$. That seems to contradict our prediction that the restoration temperature in the chiral limit could be $T_{\text{degen.},c} < 1.15T_c$. The findings of that study [48] would also mean that the effective restoration of $U_A(1)$ at physical quark masses [12] would happen at lower temperatures ($T \approx 200$ MeV) than it would in the chiral limit. In both studies (this thesis and [12]) the focus was however not the potential effective $U_A(1)$ symmetry restoration at some high temperature. The focus of this thesis was the potential $U_A(1)$ symmetry restoration at the chiral phase transition. Therefore we leave the question of a potential $U_A(1)$ symmetry restoration at some temperature far higher than the chiral phase transition temperature open at this point. We close with our finding that $U_A(1)$ symmetry seem to stay broken at the chiral phase transition. Nonetheless more research should be done in that regard since this was just a first study on that specific question.

In the next chapter 5 we conclude our thesis.

Chapter 5

Conclusion

In this chapter we want to conclude and summarize the insights and the results of this thesis.

We calculated mesonic screening mass correlators for lower than physical light quark masses and analyzed them in order to answer the question if the anomaly of $U_A(1)$ exists at the phase transition temperature for vanishing light quark masses, the so-called chiral limit. We also looked into the content of those mesonic screening mass correlators by switching the boundary conditions of the valence quarks to periodic temporal boundary conditions instead of the usual anti-periodic temporal boundary conditions.

From the latter analysis we could not see a pure mesonic state for our mesonic screening mass correlators for our temperature range down to a temperature of 140 MeV. Keep in mind that we did not perform any extrapolations for these screening masses. Therefore we put further analysis on hold in this direction until we calculate correlators for lower temperatures.

Regarding the anomaly of $U_A(1)$ we investigated the thermodynamic and continuum limit for our mass ratios of $m_s/m_l = 80$ and $m_s/m_l = 40$ before we turned to the chiral limit extrapolation using results from a former study [12] at the physical mass ratio of $m_s/m_l = 27$. In all calculations we set the strange quark mass m_s to the physical quark mass values. We analyzed the screening masses as well as the corresponding susceptibilities related to the $U_A(1)$ anomaly.

From the analysis of the infinite volume extrapolations we can conclude that our largest lattices with $N_s \geq 4N_\tau$ were already large enough because of two reasons. First the largest volumes agreed mostly with the infinite-volume-extrapolated values and second the systematic uncertainties resulting from cut-off effects due to our finite lattice spacing are overall larger than the finite volume effects. The infinite volume extrapolations seem to, if at all, push the degeneracy temperature of the pion mass m_π and the iso-vector scalar mass m_{a_0} as well as their susceptibilities χ_π and χ_{a_0} to a higher temperature,

which could be investigated further.

From the analysis of the continuum limit extrapolations we conclude that this limit is necessary to draw proper conclusions for continuum physics. We also saw that we can use values interpolated between our calculated values along different temperatures for the continuum limit extrapolations. This is especially important since we needed values at the transition temperature intervals. We also saw that for lighter light quark masses m_l the degeneracy temperature relative to their transition temperature seemed to get smaller. That would show that the effect of the explicit breaking of $U_A(1)$ by the mass term gets weaker. With the assumptions that the temperatures at which the results of masses m_π and m_{a_0} as well as the susceptibilities χ_π and χ_{a_0} become degenerate (degeneration temperature) are correct and that for decreasing light quark masses m_l the degeneracy temperature relative to their transition temperature gets smaller, we also made an upper bound of the restoration temperature in the chiral limit. This temperature would therefore be $T_{\text{degen.},c} < 1.15 T_c \approx 151.8$ MeV.

In the last result section we tried to approach the chiral limit extrapolations for the screening masses of π and a_0 as well as for the susceptibilities. To reduce the uncertainties we took the difference, which is a measure for the anomalous $U_A(1)$ symmetry breaking before we extrapolated to the continuum and chiral limit $m_l \to 0$. Since we had no true expectation for the fitting function of the chiral limit extrapolations, we tried a few possible fitting functions, which we motivated in section 3.4. For the screening masses we used a linear as well as a square root and a combined fitting function consisting of both terms. Only the linear fitting function in light quark mass showed a clearly broken $U_A(1)$ symmetry at the phase transition temperature in the chiral limit. The other two fitting functions agree within uncertainty bands with an effective $U_A(1)$ symmetry restoration. The chiral limit extrapolations for their susceptibilities on the other hand showed only a broken $U_A(1)$ symmetry. We used as fitting functions a linear as well as a square root to the power of 3 and a combined fitting function for the difference of χ_π and χ_{a_0} as well as the inverse of this difference.

These findings for the susceptibilities differ to the screening mass chiral limit extrapolations which had a possible $U_A(1)$ symmetry restoration at T_c for some fitting functions even though they should show the same result. One possible reason for that is that the screening mass extrapolation for the scalar might be imprecise.

Nonetheless we only had three data points ($m_s/m_l = 80$, $m_s/m_l = 40$ and $m_s/m_l = 27$) to play with and had no expectation for the fitting function towards chiral limit. Therefore other possible reasons might be that the $m_s/m_l = 27$ value for the susceptibilities is not in the scaling regime for a simple chiral limit extrapolation or that the used fitting functions are just incorrect. To improve on that values at an even lighter light quark mass m_l

are needed because at this point we can neither exclude possible higher order corrections for the physical quark mass ratio nor can we exclude or conclude to a fitting function. Since for some of our fitting functions an effective $U_A(1)$ symmetry restoration might be possible, proper thermodynamic limit extrapolations might adjust the chiral limit extrapolated values to a broken $U_A(1)$ symmetry as mentioned before.

More research should be done on the topic of $U_A(1)$. Especially increasing the number of points for the chiral limit extrapolation as well as trying to verify our finding that for decreasing m_l the degeneracy temperature relative to their transition temperature gets smaller, which would create an upper bound to the degeneration temperature in the chiral limit.

Acknowledgement

This work was supported by the Deutsche Forschungsgemeinschaft (DFG, German Research Foundation) - Project number 315477589-TRR 211 and the grant number 05P18PBCA1 of the German Bundesministerium für Bildung und Forschung.

We acknowledge PRACE for awarding us access to Piz Daint, at the Swiss National Supercomputing Centre (CSCS), Switzerland.

This research also used computing resources made available through the GPU supercomputing cluster of Bielefeld University, Germany.

Thanks to those for making this work possible. I also want to thank BGTS and HGS-HIRe for the opportunities they gave me.

There are a lot of individual people who helped me during the creation of this thesis. Some helped me with the general framework, some with advice and some with their personal support.

First I want to thank my family for the great support in all these years. They encouraged me throughout and helped me when I doubted myself.

Next I want to thank my bosses.

In the beginning Edwin Laermann was officially my supervisor but unfortunately I did not have the pleasure to meet him personally since he was terminally ill when I came to Bielefeld. He created an interesting research topic that led to this thesis work. Although he was not at the university anymore he still kept friendly contact with our group until he lost the battle against his illness.

In his place Olaf Kaczmarek managed all main supervising of Edwin's students, including me. Olaf was therefore soon loaded by more work than usual, but somehow he still managed to find time for me and helped me integrate quickly into our lattice group. He also helped me with most of the organizational work and made even time for spontaneous visits to also answer my physics questions.

After Edwin's unfortunate death Frithjof Karsch took over as my co-supervisor until the end of my thesis. During the beginning of my thesis Frithjof was already helping me tackle some challenges in physics I was struggling with. Even though my work was not exactly the main focus of his research, he filled the gap with all his knowledge about the whole field of

lattice QCD and gave important input for my work.

So thank you all for your support.

I also want to thank Hauke for his excellent work on the great AnalysisToolBox, which I heavily used for the mass extration in this thesis. I want to thank him also for showing me how the university works and how to set up my working tools.

Next I want to thank our secretaries Gudrun, Susi and Irene for their great work of removing all the bureaucratic obstacles so that we can bring our main focus to the scientific work. I want to thank in particular Gudrun since I was bothering her the most during those years, especially because our boisterous office was right next to hers.

I also want to thank all my people which I met in Bielefeld. You made working here really fun. Taking lunches together, spending our free time together in restaurants, making some trips, exercising in the university gym together, learning German, ... The list of people I need to thank for that would be too long and I would probably miss someone accidentally, but you know who you are. Feel my gratitude.

I want to say special thanks to my two office buddies, Anirban and Jishnu, for all the fun hours we spent in our oftentimes crowded office. You helped me with alot of coding and fundamental physics problems.

Finally I want to thank my proofreaders, David, my office buddies, Frithjof and Olaf, for squeezing out all my horrible spelling errors and weird formulations in this thesis for a buttery smooth read.

Appendix

β	T[MeV]	π mass $24^3 \times 8$	π mass $32^3 \times 8$	π mass $40^3 \times 8$
6.260	136.716	0.118796 (488)	0.115750 (271)	0.115661(318)
6.285	140.323	0.120863 (494)	0.117292 (372)	0.116115(223)
6.300	142.531	0.122013 (668)	0.118066 (534)	0.116931(250)
6.315	144.773	0.123834 (675)	0.118038 (760)	0.118609(211)
6.330	147.048	0.124981 (689)	0.121113 (610)	0.120782(346)
6.354	150.761	0.131425(1144)	0.127628 (681)	0.125888(309)
6.365	152.492	0.136485 (871)	0.129408(1068)	0.129366(320)
6.390	156.497	0.147304 (698)	0.141245(1033)	0.138864(291)
6.423	161.934	0.161339(1642)	0.160554(1673)	0.158942(578)
6.445	165.656	0.179250 (751)	0.174296(1910)	0.174051(953)

Table 1: Statistics for lattices of size $N_s^3 = 24^3, 32^3, 40^3$ with $N_\tau = 8$ at mass ratio $m_s/m_l = 40$. Temperature T is in f_K-scale from [12]. Masses are in lattice units.

β	T[MeV]	a_0 mass $24^3 \times 8$	a_0 mass $32^3 \times 8$	a_0 mass $40^3 \times 8$
6.260	136.716	0.241089(9051)	0.287040(20607)	0.298214(7771)
6.285	140.323	0.224911(4250)	0.247153(20029)	0.268297(7153)
6.300	142.531	0.218528(4929)	0.244262 (6527)	0.271320(4691)
6.315	144.773	0.209859(4907)	0.237856 (6460)	0.260511(3978)
6.330	147.048	0.204117(5089)	0.238723 (4501)	0.250178(3784)
6.354	150.761	0.197638(3432)	0.218733 (3504)	0.230150(3630)
6.365	152.492	0.195781(1875)	0.212960 (3688)	0.224438(1576)
6.390	156.497	0.193474(3314)	0.208860 (2624)	0.209257 (849)
6.423	161.934	0.197641(1726)	0.202590 (2004)	0.208635 (984)
6.445	165.656	0.208194 (736)	0.211196 (1847)	0.211553(1351)

Table 2: Statistics for lattices of size $N_s^3 = 24^3, 32^3, 40^3$ with $N_\tau = 8$ at mass ratio $m_s/m_l = 40$. Temperature T is in f_K-scale from [12]. Masses are in lattice units.

β	T[MeV]	π mass $42^3 \times 12$	π mass $60^3 \times 12$
6.600	129.447	0.080095 (330)	0.079236 (164)
6.640	134.804	0.080290 (521)	0.079103 (181)
6.680	140.355	0.082140 (561)	0.079466 (232)
6.712	144.938	0.085047 (732)	0.081332 (299)
6.754	151.149	0.090573 (548)	0.088322 (495)
6.794	157.275	0.102211(1382)	0.098867 (555)
6.825	162.167	0.115576(1473)	0.111477 (997)
6.850	166.206	0.124944(2030)	0.125594(1471)

Table 3: Statistics for lattices of size $N_s^3 = 42^3, 60^3$ with $N_\tau = 12$ at mass ratio $m_s/m_l = 40$. Temperature T is in f_K-scale from [12]. Masses are in lattice units.

β	T[MeV]	a_0 mass $42^3 \times 12$	a_0 mass $60^3 \times 12$
6.600	129.447	0.155120(3904)	0.171214(7338)
6.640	134.804	0.133220(3024)	0.145981(9280)
6.680	140.355	0.125351(3890)	0.145434(7338)
6.712	144.938	0.127313(2467)	0.144591(3179)
6.754	151.149	0.127282(1754)	0.132688(3491)
6.794	157.275	0.132420(1593)	0.137678 (983)
6.825	162.167	0.134857(1558)	0.139400(1327)
6.850	166.206	0.140745(1905)	0.147470(1517)

Table 4: Statistics for lattices of size $N_s^3 = 42^3, 60^3$ with $N_\tau = 12$ at mass ratio $m_s/m_l = 40$. Temperature T is in f_K-scale from [12]. Masses are in lattice units.

β	T[MeV]	π mass $24^3 \times 6$	π mass $32^3 \times 6$	π mass $48^3 \times 6$
6.025	142.727	0.114345 (995)	-	0.111989 (255)
6.038	144.665	0.113997(1079)	-	0.113597 (266)
6.050	146.479	0.118425(1281)	-	0.116167 (166)
6.062	148.316	0.121767 (989)	0.120158 (666)	0.118460 (340)
6.075	150.334	0.128881(1148)	-	0.124225(1058)
6.090	152.697	0.132943(1202)	0.129963 (483)	0.130210 (369)
6.105	155.100	0.141922(1387)	-	0.139545 (462)
6.120	157.541	-	-	0.150344 (606)
6.125	158.363	0.157340(1338)	-	-
6.135	160.021	0.168713(2139)	0.162028(1645)	-
6.150	162.542	0.186057(1706)	0.179298(1539)	-

Table 5: Statistics for lattices of size $N_s^3 = 24^3, 32^3, 48^3$ with $N_\tau = 6$ at mass ratio $m_s/m_l = 80$. Temperature T is in f_K-scale from [12]. Masses are in lattice units.

β	T[MeV]	a_0 mass $24^3 \times 6$	a_0 mass $32^3 \times 6$	a_0 mass $48^3 \times 6$
6.025	142.727	0.330629(16969)	-	0.358502(20910)
6.038	144.665	0.262934(11220)	-	0.334980(19311)
6.050	146.479	0.271755(15971)	-	0.310816(16587)
6.062	148.316	0.257380(11293)	0.256512(14360)	0.292475 (7685)
6.075	150.334	0.253146 (9348)	-	0.280016(14164)
6.090	152.697	0.231926 (6957)	0.262930 (5173)	0.258801 (5271)
6.105	155.100	0.226325 (6748)	-	0.243879 (4495)
6.120	157.541	-	-	0.235395 (3541)
6.125	158.363	0.223597 (3942)	-	-
6.135	160.021	0.227051 (2635)	0.231895 (3849)	-
6.150	162.542	0.228467 (982)	0.230878 (3245)	-

Table 6: Statistics for lattices of size $N_s^3 = 24^3, 32^3, 48^3$ with $N_\tau = 6$ at mass ratio $m_s/m_l = 80$. Temperature T is in f_K-scale from [12]. Masses are in lattice units.

β	T[MeV]	π mass $32^3 \times 8$	π mass $40^3 \times 8$	π mass $56^3 \times 8$
6.285	140.323	0.089402 (212)	0.088207 (339)	0.087212 (201)
6.300	142.531	0.091082 (283)	0.088786 (503)	0.086335(2646)
6.315	144.773	0.094100 (257)	0.092333 (436)	0.091228 (730)
6.330	147.048	0.097964 (403)	0.096650 (382)	0.095889(1029)
6.354	150.761	0.106768 (364)	0.104236 (557)	0.105774(1912)
6.372	153.604	0.115157 (757)	0.112577 (683)	0.111068(2415)
6.390	156.497	0.126478(1048)	0.124245 (753)	0.130429(2226)
6.423	161.934	0.149494(1264)	0.149704(1000)	0.161789(5224)
6.445	165.656	0.167146(1568)	0.169778(1454)	0.177485(3516)

Table 7: Statistics for lattices of size $N_s^3 = 32^3, 40^3, 56^3$ with $N_\tau = 8$ at mass ratio $m_s/m_l = 80$. Temperature T is in f_K-scale from [12]. Masses are in lattice units.

β	T[MeV]	a_0 mass $32^3 \times 8$	a_0 mass $40^3 \times 8$	a_0 mass $56^3 \times 8$
6.285	140.323	0.195141(7463)	0.216672(5892)	0.212718(57416)
6.300	142.531	0.180078(6677)	0.199696(4113)	0.217846(17191)
6.315	144.773	0.174780(2696)	0.187863(6518)	0.206061(13681)
6.330	147.048	0.173269(2447)	0.188774(4761)	0.187358(10786)
6.354	150.761	0.163877(1363)	0.173702(2201)	0.179778 (8698)
6.372	153.604	0.161836 (771)	0.165668(1141)	0.171626 (3680)
6.390	156.497	0.162301 (817)	0.167449(1268)	0.178032 (3126)
6.423	161.934	0.173557(1377)	0.177919 (791)	0.183375 (5009)
6.445	165.656	0.185555(1627)	0.185701(1267)	0.193647 (2644)

Table 8: Statistics for lattices of size $N_s^3 = 32^3, 40^3, 56^3$ with $N_\tau = 8$ at mass ratio $m_s/m_l = 80$. Temperature T is in f_K-scale from [12]. Masses are in lattice units.

β	T[MeV]	π mass $48^3 \times 12$	π mass $60^3 \times 12$	π mass $72^3 \times 12$
6.600	129.447	0.059599 (495)	0.059282 (269)	-
6.640	134.804	0.060959 (373)	0.059999 (313)	0.059070(263)
6.680	140.355	0.064104 (365)	0.061719 (382)	0.061140(264)
6.712	144.938	0.067386 (507)	0.066618 (394)	0.066267(329)
6.733	148.015	0.073419(1197)	0.072120 (811)	0.069801(457)
6.754	151.149	0.077704 (535)	0.077335 (582)	0.076375(769)
6.794	157.275	-	0.092257 (921)	-
6.825	162.167	-	0.110037(1493)	-
6.850	166.206	-	0.119664(1834)	-

Table 9: Statistics for lattices of size $N_s^3 = 48^3, 60^3, 72^3$ with $N_\tau = 12$ at mass ratio $m_s/m_l = 80$. Temperature T is in f_K-scale from [12]. Masses are in lattice units.

β	T[MeV]	a_0 mass $48^3 \times 12$	a_0 mass $60^3 \times 12$	a_0 mass $72^3 \times 12$
6.600	129.447	0.112909(3474)	0.138199(5884)	-
6.640	134.804	0.108412(1914)	0.124861(3452)	0.131327(5733)
6.680	140.355	0.099911(3443)	0.112288(3186)	0.103033(7260)
6.712	144.938	0.095823(1727)	0.106410(3120)	0.113125(1251)
6.733	148.015	0.100253(1940)	0.107989(1871)	0.109506(1614)
6.754	151.149	0.098932(1080)	0.105365(1530)	0.107286(1140)
6.794	157.275	-	0.110500 (908)	-
6.825	162.167	-	0.121274(1406)	-
6.850	166.206	-	0.128370(1625)	-

Table 10: Statistics for lattices of size $N_s^3 = 48^3, 60^3, 72^3$ with $N_\tau = 12$ at mass ratio $m_s/m_l = 80$. Temperature T is in f_K-scale from [12].

β	T[MeV]	π mass	a_0 mass
6.285	140.323	0.065109 (292)	0.190385(8548)
6.300	142.531	0.067891 (289)	0.183462(7413)
6.315	144.773	0.070927 (335)	0.166108(3871)
6.330	147.048	0.075995 (341)	0.155590(3515)
6.354	150.761	0.086872 (509)	0.140507(1878)
6.372	153.604	0.102967(2433)	0.139551(2245)
6.390	156.497	0.112529(1502)	0.140440(1215)
6.423	161.934	0.143661(1162)	0.156180(1022)
6.445	165.656	0.164207(1504)	0.172853(1274)

Table 11: Statistics for lattice of size $56^3 \times 8$ at mass ratio $m_s/m_l = 160$. Temperature T is in f_K-scale from [12]. Masses are in lattice units.

β	T[MeV]	π mass $24^3 \times 6$	π mass $32^3 \times 6$	π mass $48^3 \times 6$
6.025	142.727	0.091287(663)	-	0.091165(121)
6.038	144.665	0.090756(673)	-	0.089932(131)
6.050	146.479	0.090082(434)	-	0.088526 (94)
6.062	148.316	0.086925(796)	0.087612(217)	0.087497(136)
6.075	150.334	0.086965(775)	-	0.086109(299)
6.090	152.697	0.085292(473)	0.084569(311)	0.084180 (97)
6.105	155.100	0.084056(523)	-	0.082732(121)
6.120	157.541	-	-	0.081242(164)
6.125	158.363	0.082735(607)	-	-
6.135	160.021	0.081281(715)	0.079911(366)	0.079296(321)
6.150	162.542	0.079019(800)	0.078223(344)	-

Table 12: Statistics for lattices of size $N_s^3 = 24^3, 32^3, 48^3$ with $N_\tau = 6$ at mass ratio $m_s/m_l = 80$ using periodic boundary conditions. Temperature T is in f_K-scale from [12]. Masses are in lattice units.

β	T[MeV]	a_0 mass $24^3 \times 6$	a_0 mass $32^3 \times 6$	a_0 mass $48^3 \times 6$
6.025	142.727	0.289839(101869)	-	0.227505 (86259)
6.038	144.665	0.273578 (92960)	-	0.297771 (58015)
6.050	146.479	0.274221 (68226)	-	0.267349 (41479)
6.062	148.316	-	0.368507(116849)	0.354760 (89159)
6.075	150.334	0.324173 (87517)	-	0.321200(152206)
6.090	152.697	0.356392(135807)	0.276944 (59882)	0.299071 (58905)
6.105	155.100	0.270028 (60107)	-	0.335412 (74395)
6.120	157.541	-	-	0.228277 (48982)
6.125	158.363	0.277873(105586)	-	-
6.135	160.021	0.129514 (50935)	0.207690 (44694)	0.405724 (77356)
6.150	162.542	0.169164 (63333)	0.442681 (59208)	-

Table 13: Statistics for lattices of size $N_s^3 = 24^3, 32^3, 48^3$ with $N_\tau = 6$ at mass ratio $m_s/m_l = 80$ using periodic boundary conditions. Temperature T is in f_K-scale from [12]. Masses are in lattice units.

β	T[MeV]	π mass $32^3 \times 8$	π mass $40^3 \times 8$	π mass $56^3 \times 8$
6.260	136.716	0.072949(484)	-	-
6.285	140.323	0.072351(402)	0.070574(633)	0.070605(100)
6.300	142.531	0.070534(326)	0.069899(322)	0.069174(102)
6.315	144.773	0.068914(353)	0.068090(367)	0.068083(124)
6.330	147.048	0.068537(501)	0.067477(360)	0.066757(116)
6.354	150.761	0.065925(362)	0.066085(359)	0.064688(159)
6.372	153.604	0.064390(452)	0.063993(384)	0.063185(101)
6.390	156.497	0.062633(466)	0.061632(274)	0.061269(152)
6.423	161.934	0.060716(698)	0.059186(472)	0.058560(165)
6.445	165.656	0.058903(748)	0.057680(394)	0.056888(155)

Table 14: Statistics for lattices of size $N_s^3 = 32^3, 40^3, 56^3$ with $N_\tau = 8$ at mass ratio $m_s/m_l = 80$ using periodic boundary conditions. Temperature T is in f_K-scale from [12]. Masses are in lattice units.

β	T[MeV]	a_0 mass $32^3 \times 8$	a_0 mass $40^3 \times 8$	a_0 mass $56^3 \times 8$
6.260	136.716	0.273765(182115)	-	-
6.285	140.323	0.192117 (52510)	0.192784(46606)	0.188896(29251)
6.300	142.531	0.133930 (38712)	0.219150(58992)	0.165975(29976)
6.315	144.773	0.154434 (26166)	0.159596(41509)	0.191072(30953)
6.330	147.048	0.170879 (35777)	0.168413(46470)	0.142240(32820)
6.354	150.761	0.171651 (37991)	0.143961(44338)	0.163282(22415)
6.372	153.604	0.178226 (59342)	0.222105(61148)	0.165434(20029)
6.390	156.497	0.156928 (36594)	0.148948(37507)	0.155172(23857)
6.423	161.934	0.131674 (29113)	0.206426(31988)	0.170064(24656)
6.445	165.656	0.124345 (37601)	0.143126(27804)	0.151012(29643)

Table 15: Statistics for lattices of size $N_s^3 = 32^3, 40^3, 56^3$ with $N_\tau = 8$ at mass ratio $m_s/m_l = 80$ using periodic boundary conditions. Temperature T is in f_K-scale from [12]. Masses are in lattice units.

β	T[MeV]	X $24^3 \times 8$	X $32^3 \times 8$	X $40^3 \times 8$
6.260	136.716	575.519(4722)	615.771(9958)	634.155(6215)
6.285	140.323	479.607(4558)	517.902(6599)	539.182(6319)
6.300	142.531	408.247(5354)	469.492(7476)	476.244(6295)
6.315	144.773	354.468(3884)	418.441(8243)	415.639(4436)
6.330	147.048	298.316(3385)	340.768(6074)	352.579(3537)
6.354	150.761	216.113(3054)	265.044(5959)	269.647(3574)
6.365	152.492	182.565(2519)	217.211(4882)	226.021(2458)
6.390	156.497	109.438(1840)	141.653(3819)	143.218(2155)
6.423	161.934	58.610(2132)	71.109(3077)	66.990(1251)
6.445	165.656	33.576(1118)	40.361(3379)	39.792(1589)

Table 16: Statistics for lattices of size $N_s^3 = 24^3, 32^3, 40^3$ with $N_\tau = 8$ at mass ratio $m_s/m_l = 40$. Temperature T is in f_K-scale from [12]. $X = m_s^2(\chi_\pi - \chi_{a_0})/T^4$.

β	T[MeV]	X $42^3 \times 12$	X $60^3 \times 12$
6.600	129.447	767.527(12606)	863.143(15946)
6.640	134.804	588.976(11088)	666.214(10971)
6.680	140.355	446.653 (9753)	489.944 (7039)
6.712	144.938	318.665 (7425)	374.354 (4714)
6.754	151.149	191.538 (9369)	224.358 (4506)
6.794	157.275	105.659 (4810)	113.859 (3015)
6.825	162.167	53.912 (3426)	62.177 (3283)
6.850	166.206	35.261 (2291)	34.170 (1841)

Table 17: Statistics for lattices of size $N_s^3 = 42^3, 60^3$ with $N_\tau = 12$ at mass ratio $m_s/m_l = 40$. Temperature T is in f_K-scale from [12]. $X = m_s^2(\chi_\pi - \chi_{a_0})/T^4$.

β	T[MeV]	X $24^3 \times 6$	X $32^3 \times 6$	X $48^3 \times 6$
6.025	142.727	877.159(12332)	-	939.978(21370)
6.038	144.665	797.494(11281)	-	842.578(13114)
6.050	146.479	704.504(12672)	-	743.773(10691)
6.062	148.316	606.069(11214)	652.943(13085)	647.522 (9052)
6.075	150.334	498.238(11793)	-	552.109(27184)
6.090	152.697	374.299 (9966)	419.836 (7037)	408.313 (5450)
6.105	155.100	284.511(10036)	-	309.956 (7897)
6.120	157.541	-	-	217.360 (8691)
6.125	158.363	170.825 (6432)	-	-
6.135	160.021	134.630 (5022)	145.456 (6080)	-
6.150	162.542	78.123 (4178)	89.518 (4835)	-

Table 18: Statistics for lattices of size $N_s^3 = 24^3, 32^3, 48^3$ with $N_\tau = 6$ at mass ratio $m_s/m_l = 80$. Temperature T is in f_K-scale from [12]. $X = m_s^2(\chi_\pi - \chi_{a_0})/T^4$.

β	T[MeV]	X $32^3 \times 8$	X $40^3 \times 8$	X $56^3 \times 8$
6.285	140.323	900.062(12385)	972.545(15949)	973.530(16337)
6.300	142.531	759.384 (8370)	824.576(11469)	837.767(14017)
6.315	144.773	627.090 (7921)	677.744 (9074)	698.729(10985)
6.330	147.048	508.291 (5534)	532.682 (6670)	572.132(11175)
6.354	150.761	327.300 (6148)	364.418 (7496)	376.802 (5558)
6.372	153.604	213.198 (4826)	249.366 (8483)	246.891 (8649)
6.390	156.497	136.639 (3711)	149.076 (4938)	148.648 (5661)
6.423	161.934	48.959 (2725)	49.825 (2305)	58.400 (4403)
6.445	165.656	23.155 (1342)	21.777 (970)	26.161 (4457)

Table 19: Statistics for lattices of size $N_s^3 = 32^3, 40^3, 56^3$ with $N_\tau = 8$ at mass ratio $m_s/m_l = 80$. Temperature T is in f_K-scale from [12]. $X = m_s^2(\chi_\pi - \chi_{a_0})/T^4$.

β	T[MeV]	X $48^3 \times 12$	X $60^3 \times 12$	X $72^3 \times 12$
6.600	129.447	1347.827(25996)	1463.346(29597)	-
6.640	134.804	986.969(11230)	1080.807(22309)	1133.099(29263)
6.680	140.355	651.064(17743)	765.120(18166)	797.453(20446)
6.712	144.938	427.904(11172)	499.274(14247)	515.409(15017)
6.733	148.015	275.967(11008)	336.714(20338)	357.736(10946)
6.754	151.149	188.761 (7675)	231.198 (7152)	234.003 (8067)
6.794	157.275	-	95.206 (7651)	-
6.825	162.167	-	35.964 (3728)	-
6.850	166.206	-	18.109 (1037)	-

Table 20: Statistics for lattices of size $N_s^3 = 48^3, 60^3, 72^3$ with $N_\tau = 12$ at mass ratio $m_s/m_l = 80$. Temperature T is in f_K-scale from [12]. $X = m_s^2(\chi_\pi - \chi_{a_0})/T^4$.

β	T[MeV]	X $56^3 \times 8$
6.285	140.323	1691.066(26353)
6.300	142.531	1422.378(23775)
6.315	144.773	1142.259(32181)
6.330	147.048	887.361(24602)
6.354	150.761	500.827(17020)
6.372	153.604	281.892(19594)
6.390	156.497	135.617 (7470)
6.423	161.934	28.632 (2514)
6.445	165.656	12.735 (1939)

Table 21: Statistics for lattice of size $56^3 \times 8$ at mass ratio $m_s/m_l = 160$. Temperature T is in f_K-scale from [12]. $X = m_s^2(\chi_\pi - \chi_{a_0})/T^4$.

β	T[MeV]	Y $40^3 \times 8$ $m_s/m_l = 40$	Y $56^3 \times 8$ $m_s/m_l = 80$
6.260	136.716	1.163770(65128)	-
6.285	140.323	0.930950(53349)	0.880425(143292)
6.300	142.531	0.824579(40818)	0.502308 (74920)
6.315	144.773	0.629069(38505)	0.598199 (89900)
6.330	147.048	0.528017(39753)	0.343010 (52331)
6.354	150.761	0.362567(27728)	0.331776 (53144)
6.365	152.492	0.270926(38834)	-
6.372	153.604	-	0.158112 (91472)
6.390	156.497	0.214889(21828)	0.141127 (41325)
6.423	161.934	0.084740(14175)	-0.003069 (42144)
6.445	165.656	0.071745(15737)	-0.047473 (58972)

Table 22: Statistics for lattices of size $N_s^3 = 40^3$ and $N_s^3 = 56^3$ with $N_\tau = 8$ at mass ratio $m_s/m_l = 40$ and $m_s/m_l = 80$ respectively. Temperature T is in f_K-scale from [12]. $Y = m_s^2(\chi_\rho - \chi_{a_1})/T^4$.

Bibliography

[1] J. C. Collins and M. J. Perry, *Superdense Matter: Neutrons or Asymptotically Free Quarks?*, Phys. Rev. Lett. **34** (1975) 1353.

[2] H.-T. Ding, F. Karsch, and S. Mukherjee, *Thermodynamics of Strong-Interaction Matter from Lattice QCD*, Quark–Gluon Plasma 5 (2016) 1.

[3] Y. Aoki, G. Endrődi, Z. Fodor, S. D. Katz, and K. K. Szabó, *The Order of the Quantum Chromodynamics transition predicted by the Standard Model of particle physics*, Nature **443** (2006) 675.

[4] I. Arsene et al., *Quark gluon plasma and color glass condensate at RHIC? The Perspective from the BRAHMS experiment*, Nucl. Phys. A **757** (2005) 1.

[5] J. Adams et al. [STAR Collaboration], *Experimental and theoretical challenges in the search for the quark gluon plasma: The STAR Collaboration's critical assessment of the evidence from RHIC collisions*, Nucl. Phys. A **757** (2005) 102.

[6] B. B. Back et al. [PHOBOS Collaboration], *The PHOBOS perspective on discoveries at RHIC*, Nucl. Phys. A **757** (2005) 28.

[7] K. Adcox et al. [PHENIX Collaboration], *Formation of dense partonic matter in relativistic nucleus-nucleus collisions at RHIC: Experimental evaluation by the PHENIX collaboration*, Nucl. Phys. A **757** (2005) 184.

[8] H.-T. Ding et al. [HotQCD Collaboration], *Chiral Phase Transition Temperature in* (2+1)*-Flavor QCD*, Phys. Rev. Lett. **123** (2019) 062002.

[9] F. Gao and J. M. Pawlowski, *QCD phase structure from functional methods*, Phys. Rev. D **102** (2020) 034027.

[10] J. Schaffner-Bielich, *Signals of the QCD Phase Transition in the Heavens*, PoS **CPOD07** (2008) 062.

[11] K. G. Wilson, *Confinement of Quarks*, Phys. Rev. D **10** (1974) 2445.

[12] A. Bazavov et al. [HotQCD Collaboration], *Meson screening masses in* $(2+1)$*-flavor QCD*, Phys. Rev. D **100** (2019) 094510.

[13] E. Witten, *Current algebra theorems for the U(1) "Goldstone Boson"*, Nucl. Phys. B **156** (1979) 269.

[14] G. Veneziano, *U(1) without instantons*, Nucl. Phys. B **159** (1979) 213.

[15] B. B. Brandt et al., *On the strength of the* $U_A(1)$ *anomaly at the chiral phase transition in* $N_f = 2$ *QCD*, JHEP **12** (2016) 158.

[16] R. D. Pisarski and F. Wilczek, *Remarks on the Chiral Phase Transition in Chromodynamics*, Phys. Rev. D **29** (1984) 338.

[17] A. Pelissetto and E. Vicari, *Relevance of the axial anomaly at the finite-temperature chiral transition in QCD*, Phys. Rev. D **88** (2013) 105018.

[18] N. Brouzakis and N. Tetradis, *The universal equation of state near the critical point of QCD*, Nuclear Physics A **742** (2004) 144.

[19] A. Bazavov et al. [HotQCD Collaboration], *Chiral and deconfinement aspects of the QCD transition*, Phys. Rev. D **85** (2012) 054503.

[20] C. Gattringer and C. B. Lang, *Quantum Chromodynamics on the Lattice: An Introductory Presentation*, Lect. Notes in Phys. **788** (2010) Springer.

[21] T. DeGrand and C. DeTar, *Lattice methods for quantum chromodynamics* (2006) World Scientific.

[22] H. B. Nielsen and M. Ninomiya, *A no-go theorem for regularizing chiral fermions*, Phys. Lett. B **105** (1981) 219.

[23] A. S. Kronfeld, *Lattice gauge theory with staggered fermions: how, where, and why (not)*, PoS **LATTICE2007** (2008) 016.

[24] S. Prelovsek, *Effects of staggered fermions and mixed actions on the scalar correlator*, Phys. Rev. D **73** (2006) 014506.

[25] S. Prelovsek, C. Dawson, T. Izubuchi, K. Orginos, and A. Soni, *Scalar meson in dynamical and partially quenched two-flavor QCD: Lattice results and chiral loops*, Phys. Rev. D **70** (2004) 094503.

[26] Z.-W. Fu and C. DeTar, *Scalar meson spectroscopy with a fine lattice*, Chin. Phys. C **35** (2011) 896.

[27] E. Follana et al. [HPQCD collaboration], *Further Improvements to staggered quarks*, Nucl. Phys. B Proc. Suppl. **129** (2004) 447.

[28] P. Steinbrecher, *The QCD crossover up to $\mathcal{O}(\mu_B^6)$ from Lattice QCD* PhD thesis, U. Bielefeld (main), 2018.

[29] S. R. Sharpe and A. Patel, *Perturbative corrections for staggered four-fermion operators*, Nucl. Phys. B **417** (1994) 307.

[30] T. Hashimoto, A. Nakamura, and I. O. Stamatescu, *Temperature-dependent structure in the mesonic channels of QCD*, Nucl. Phys. B **400** (1993) 267.

[31] M. Cheng et al., *Meson screening masses from lattice QCD with two light and one strange quark*, Eur. Phys. J. C **71** (2011) 1564.

[32] F. Karsch and E. Laermann, *Thermodynamics and in-medium hadron properties from lattice QCD*, Quark-gluon plasma 4 (2003) 1.

[33] C. DeTar and J. Kogut, *The Hadronic Spectrum of the Quark Plasma*, Phys. Rev. Lett. **59** (1987) 399.

[34] N. Kawamoto and J. Smit, *Effective lagrangian and dynamical symmetry breaking in strongly coupled lattice QCD*, Nucl. Phys. B **192** (1981) 100.

[35] A. Bazavov et al., *Nonperturbative QCD simulations with $2+1$ flavors of improved staggered quarks*, Rev. Mod. Phys. **82** (2010) 1349.

[36] E. Laermann and F. Pucci, *Taste symmetry breaking at finite temperature*, Eur. Phys. J. C **72** (2012) 2200.

[37] R. Sommer, *Scale setting in lattice QCD*, PoS **LATTICE2013** (2014) 015.

[38] M. E. Peskin and D. V. Schroeder, *An Introduction to quantum field theory* (1995) CRC Press.

[39] D. T. Son and M. A. Stephanov, *Pion Propagation near the QCD Chiral Phase Transition*, Phys. Rev. Lett. **88** (2002) 202302.

[40] O. Kaczmarek, F. Karsch, A. Lahiri, and C. Schmidt, *Universal scaling properties of QCD close to the chiral limit*, Acta Phys. Pol. B Proc. Suppl. **14** (2021) 291.

[41] O. Philipsen and C. Pinke, *The $N_f = 2$ QCD chiral phase transition with Wilson fermions at zero and imaginary chemical potential*, Phys. Rev. D **93** (2016) 114507.

[42] F. Karsch, *Critical behavior and net-charge fluctuations from lattice QCD*, PoS **CORFU2018** (2019) 163.

[43] S. H. Lee and T. Hatsuda, *$U_A(1)$ symmetry restoration in QCD with N_f flavors*, Phys. Rev. D **54** (1996) R1871.

[44] A. Bazavov et al. [HotQCD Collaboration], *Chiral transition and $U(1)_A$ symmetry restoration from lattice QCD using domain wall fermions*, Phys. Rev. D **86** (2012) 094503.

[45] M. I. Buchoff et al. [LLNL/RBC Collaboration], *QCD chiral transition, $U(1)_A$ symmetry and the dirac spectrum using domain wall fermions*, Phys. Rev. D **89** (2014) 054514.

[46] V. Dick, F. Karsch, E. Laermann, S. Mukherjee, and S. Sharma, *Microscopic origin of $U_A(1)$ symmetry violation in the high temperature phase of QCD*, Phys. Rev. D **91** (2015) 094504.

[47] O. Kaczmarek, L. Mazur, and S. Sharma, *Eigenvalue spectra of QCD and the fate of $U_A(1)$ breaking towards the chiral limit* arXiv:2102.06136.

[48] H.-T. Ding, S.-T. Li, S. Mukherjee, A. Tomiya, X.-D. Wang, and Y. Zhang, *Correlated Dirac Eigenvalues and Axial Anomaly in Chiral Symmetric QCD*, Phys. Rev. Lett. **126** (2021) 082001.

[49] G. Cossu, S. Aoki, H. Fukaya, S. Hashimoto, T. Kaneko, H. Matsufuru, and J.-I. Noaki, *Finite temperature study of the axial U(1) symmetry on the lattice with overlap fermion formulation*, Phys. Rev. D **87** (2013) 114514. [Erratum: Phys. Rev. D **88** (2013) 019901].

[50] A. Tomiya, G. Cossu, S. Aoki, H. Fukaya, S. Hashimoto, T. Kaneko, and J. Noaki [JLQCD Collaboration], *Evidence of effective axial $U(1)$ symmetry restoration at high temperature QCD*, Phys. Rev. D **96** (2017) 034509. [Addendum: Phys. Rev. D **96** (2017) 079902].

[51] S. Ejiri, Y. Maezawa, N. Ukita, S. Aoki, T. Hatsuda, N. Ishii, K. Kanaya, and T. Umeda [WHOT-QCD Collaboration], *Equation of state and heavy-quark free energy at finite temperature and density in two flavor lattice QCD with Wilson quark action*, Phys. Rev. D **82** (2010) 014508.

[52] S. Aoki, Y. Aoki, H. Fukaya, S. Hashimoto, C. Rohrhofer, and K. Suzuki [JLQCD collaboration], *Role of axial $U(1)$ anomaly in chiral susceptibility of QCD at high temperature*, arXiv:2103.05954.

[53] H. S. Sandmeyer, *Hadronic correlators from heavy to very light quarks: Spectral and transport properties from lattice QCD*. PhD thesis, U. Bielefeld (main), 2019.

[54] H. Akaike, *A new look at the statistical model identification*, IEEE Transactions on Automatic Control **19** (1974) 716.

[55] S. Aoki, T. Umemura, M. Fukugita, N. Ishizuka, H. Mino, M. Okawa, and A. Ukawa, *Finite-size effects of hadron masses in lattice QCD: A comparative study for quenched and full QCD simulations*, Phys. Rev. D **50** (1994) 486.

[56] E. Laermann, M. Mueller, and O. Kaczmarek, *The thermodynamic and continuum limit of meson screening masses*, PoS **LATTICE 2013** (2014) 150.

[57] K. Rajagopal and F. Wilczek, *Static and dynamic critical phenomena at a second order QCD phase transition*, Nucl. Phys. B **399** (1993) 395.

[58] J. Engels and F. Karsch, *The scaling functions of the free energy density and its derivatives for the* $3d$ $O(4)$ *model*, Phys. Rev. D **85** (2012) 094506.

[59] S. Ejiri, F. Karsch, E. Laermann, C. Miao, S. Mukherjee, P. Petreczky, C. Schmidt, W. Soeldner, and W. Unger, *Magnetic equation of state in* $(2+1)$*-flavor QCD*, Phys. Rev. D **80** (2009) 094505.

[60] W. Florkowski and B. L. Friman, *Spatial dependence of the finite temperature meson correlation function*, Z. Phys. A **347** (1994) 271.

[61] C. Rohrhofer, Y. Aoki, G. Cossu, H. Fukaya, C. Gattringer, L. Y. Glozman, S. Hashimoto, C. B. Lang, and S. Prelovsek, *Symmetries of spatial meson correlators in high temperature QCD*, Phys. Rev. D **100** (2019) 014502.

[62] A. Bazavov et al. [HotQCD Collaboration], *Chiral and deconfinement aspects of the QCD transition*, Phys. Rev. D **85** (2012) 054503.

[63] C. Bernard et al., *QCD spectrum with three quark flavors*, Phys. Rev. D **64** (2001) 054506.

[64] A. Bazavov et al. [HotQCD Collaboration], *Equation of state in* $(2+1)$*-flavor QCD*, Phys. Rev. D **90** (2014) 094503.

[65] T. DeGrand, *Log-normal distribution for correlators in lattice QCD?*, Phys. Rev. D **86** (2012) 014512.

[66] A. Bazavov et al. [HotQCD Collaboration], *Chiral crossover in QCD at zero and non-zero chemical potentials*, Phys. Lett. B **795** (2019) 15.

[67] S. Dentinger, O. Kaczmarek, and A. Lahiri, *Screening masses towards chiral limit*, Acta Phys. Pol. B Proc. Suppl. **14** (2021) 321.

[68] F. Karsch, E. Laermann, S. Mukherjee, and P. Petreczky, *Signatures of charmonium modification in spatial correlation functions*, Phys. Rev. D **85** (2012) 114501.

[69] T. Bhattacharya et al. [HotQCD Collaboration], *QCD Phase Transition with Chiral Quarks and Physical Quark Masses*, Phys. Rev. Lett. **113** (2014) 082001.

Disclaimer

I hereby declare that the work done in this thesis is that of the author alone with the help of no more than the mentioned literature and auxiliary means.

Bielefeld, November 5, 2021

Simon Fabian Dentinger

Gedruckt auf alterungsbeständigem Papier gemäß DIN ISO 9706.